Model Predictive Control of Diesel Fuel Consumption and On-road Emission Constraints

by

Saravanan Duraiarasan

A dissertation submitted in partial fulfillment
of the requirements for the degree of
Doctor of Philosophy
(Mechanical Engineering)
in the University of Michigan
2021

Doctoral Committee:

Professor Anna Stefanopoulou, Chair
Professor Andre Boehman
Professor Ilya Kolmanovsky
Assistant Research Scientist Robert Middleton

Saravanan Duraiarasan

saravan@umich.edu

ORCID iD: 0000-0002-7682-6584

Dedication

To my maternal uncle Mr. Rajendran for his love, sacrifices, and never-ending support.

Acknowledgments

I want to thank my Ph.D. advisor Professor Anna Stefanopoulou for providing me the opportunity to work in her esteemed research group. Her continued support, trust, encouragement, and motivation helped me to grow both professionally and personally. I would also like to thank her for providing the unique opportunity to use the state-of-the-art heavy-duty powertrain test facility. Due to that, I was able to craft my Ph.D. research with a good mix of experimentation and simulation.

I want to thank Professor Andre Boehman for his technical guidance on the fundamentals of emission formation and aftertreatment systems. I will always be grateful for his exceptional support with the emission measurement systems. I want to thank Professor Ilya Kolmanovsky for his valuable remarks and fruitful discussions. His timely feedbacks helped me evaluate the model fidelity and successfully design the model predictive controller. I also want to thank Dr. Robert Middleton for his exceptional support in reviewing and providing critical feedback on our technical publications. I was also privileged to work alongside Dr. Middleton in the powertrain control laboratory, and I appreciate his willingness to help whenever needed. I would also like to thank Mr. John Hoard for sharing his technical expertise in emissions and aftertreatment systems.

I want to thank Dr. Rasoul Salehi at General Motors for his technical guidance and mentorship. This work was not possible without his endless patience with my questions and his help while code debugging. I would also like to thank Daimler Trucks North America (DTNA) for their continued financial support through the Super Truck II project. I want to thank Mr. Marc Allain and Mr. Siddharth Mahesh from DTNA for their technical support during these four long years.

I want to thank Mr. Charles Solbrig for his exceptional technical assistance with the dynamometer and data acquisition software. I also want to thank Mr. William Kirkpatrick for his help during engine and other hardware installations. I want to thank everyone in the PCL lab for their outstanding support and the much-needed fun times I spent with them, including Mr. Mitchell Bieniek, Mr. Joe Drallmeier, Ms. Miriam Figueroa, Ms. Chunan Huang, Ms. Di Chen, Ms. Eunjeong Hyeon, Mr. Venkateswaran Vaidhyanathan, Mr. Peyman Mohtat, Dr. Suhak Lee, Mr. Sravan Pannala, Mr. Omar Ahmed, Mr. Fucong Wang, Mr. Ting Cai, Dr. Niket Prakash, Dr. Rani Kiwan, Dr. Shima Nazari, and Dr. Bryan Maldonado and Dr. Gokul Siva Sankar.

I also want to thank W.E. Lay Automotive laboratory fellows Dr. Vassilis Triantopoulos, Mr. Rinav Pillai, Ms. Courtney Videchak, and Mr. Subramaniam Balakrishna for providing technical support and guidance during engine test cell operations.

I am also thankful for the ORISE aspire program, which allowed me to gain internship experience at Oak Ridge National Laboratory. It certainly had a significant impact on my research methodology later during my Ph.D.

Finally, I would like to thank my parents for allowing me to pursue my dream and for their constant words of encouragement over the years.

Table of Contents

List of Tables

List of Figures

List of Appendices

Abstract

Diesel engines continue to be an important powerplant in heavy-duty trucks due to their inherent advantages such as range, robustness to operating conditions, and wide range of torque deliverability. With the introduction of on-road-focused emission regulations, one would explore an adaptive calibration scheme, where the fuel efficiency is maximized subject to tailpipe NO_X emission constraint. Nowadays, the engine calibration setpoints are a function of speed and load calibrated offline, considering various driving profiles and certified on a specific drive cycle. This thesis explores adjusting engine setpoints online to enable future integration with the trip ahead and a preview of the load affecting the thermal and, thus, the aftertreatment conditions. Recognizing that the engine-out NO_X increases by more than 50 % for a corresponding decrease of 1 % in brake-specific fuel consumption (BSFC). It is essential to control the engine at the low BSFC conditions only when the selective catalytic reduction (SCR) is predicted to operate efficiently. Similarly, the engine operation should support the warm-up of the SCR and avoid the generation of NO_X when the SCR cannot convert it.

In this thesis, a hierarchical predictive engine and aftertreatment control architecture is designed to alter the engine setpoints to achieve the best fuel economy while the SCR effectively reduces the corresponding increase in engine-out NO_X. The advantage of the model predictive controller in handling time-delayed systems addresses the slow thermo-chemical dynamics of SCR. To implement this controller in real-time, physics-based engine airpath, engine-out NO_X emission, and aftertreatment thermodynamic models are developed.

The hierarchical controller architecture consists of a supervisory thermal management controller with a long prediction horizon and an air path controller with short prediction horizon. The supervisory controller aims to improve and maintain the aftertreatment temperature above a set catalyst light-off temperature with intake manifold pressure and the start of injection (SOI) as control variables. After the aftertreatment warm-up, the supervisory controller balances and initiates transitions to “fuel save” mode and provides fuel-optimal references. The air path

controller tracks the references dictated by the supervisory controller while it also controls the transient engine-out NO_X by compensating the reference SOI. The sub-components of this hierarchical controller are experimentally validated for real-time feasibility and prediction capability. The overall architecture is validated in a software-in-the-loop (SIL) simulation environment, and results show improved fuel economy with reduced tailpipe NO_X emission and real-time implementation feasibility.

Chapter 1 Introduction

1.1 Background

In the US, during the year 2020, the trucking industry moved 80 % of the freight generating $791.7 billion in revenue [1]. Diesel engines are the predominant and preferred choice of power source in trucks due to their high fuel economy, reliability, and wide range of torque deliverability. However, diesel engines suffer from the severe disadvantage of particulate matter (PM) emissions and nitrogen oxides (NO and NO_2, collectively called NO_X) emission and are commonly referred to as "Achille's heel of diesel engines." The modern-day heavy-duty diesel engine is equipped with a series of aftertreatment devices like diesel oxidation catalyst (DOC), diesel particulate filter (DPF), selective catalytic reduction (SCR), and ammonia slip catalyst (ASC) [2]. The PM emissions in tailpipe is controlled by DPF, and the filtration efficiency is more than 95 % for a wide operating range [3].

The NO_X emissions are reduced by the SCR using the reductant hydrolyzed urea, commercially called diesel exhaust fluid (DEF). The hydrolyzed urea is injected into the exhaust gas at a location between the turbocharger and the SCR catalyst. The hot exhaust gas converts the liquid hydrolyzed-urea into gaseous Ammonia (NH_3). The gaseous NH_3 reaches the SCR catalyst site and adsorbs on the surface of the catalyst. Under a range of SCR catalyst temperature, the NO_X in the exhaust gas reacts with NH_3 at the catalyst site to produce nitrogen and water. However, the NO_X conversion efficiency of the SCR depends significantly on the catalyst surface temperature and the availability of ammonia at the catalyst [4]. As shown in [5], a Cu/Zeolite-based SCR catalyst is more than 95 % efficient in the range of 220 to 320 ℃ catalyst temperature, whereas the efficiency drops to 60 % at 150 ℃ and further drops to 20 % at 130 ℃. During low-load engine operation, engine idle, and cold-start conditions, the engine-out exhaust gas temperature is cold, which reduces the temperature of the SCR below the efficient operating temperature (220 to 320 ℃). SCR efficiency also depends on the availability

of NH_3 in the SCR catalyst, an equimolar concentration of NH_3 and NO_X is required to achieve 100 % conversion efficiency provided the catalyst temperature is above light-off temperature. Engine-out NO_X during engine transient operations called transient NO_X, escapes from the SCR even when the overall SCR conversion efficiency is high due to the diffusion and depletion limitations in NH_3, resulting in high tailpipe NO_X. In contrast overdosing of urea causes ammonia slip [2]. Hence, in-cylinder NO_X formation control is indispensable to compensate for the limitations of SCR conversion efficiency at suboptimal temperatures and to control transient NO_X.

The formation of NO_X depends on the combustion gas temperature and the concentration of nitrogen (N_2) and oxygen (O_2) around the flame front. The NO_X formation increases exponentially with an increase in combustion gas temperature. Typically, exhaust gas recirculation (EGR) technology is used to reduce the in-cylinder NO_X formation [4]. With EGR, part of the exhaust gas is used to dilute the fresh charge, thereby reducing oxygen availability for NO_X formation and reduces the combustion gas temperature. EGR also increases the specific heat of the charge, which reduces the combustion gas temperature and thereby NO_X. In-cylinder NO_X formation can also be reduced by retarding the start of the fuel injection crank angle (SOI) and/or by reducing the fuel injection pressure [73] , which reduces the combustion pressure and temperature and thereby reduces in-cylinder NO_X formation.

Among other options such as combustion phasing, reducing friction, and pumping losses, the Diesel engine's brake thermal efficiency depends on the cylinder pressure and the corresponding increase in combustion gas temperature. As shown in Figure 1-1 in the left side plot, for a constant engine speed, torque, and SOI, closing the EGR valve position from 55 % marked as point A (which corresponds to the stock engine value at this operating condition) to 45 % marked as point B reduced the BSFC by 1.4 %. The increase in fuel economy is due to the rise in the peak cylinder pressure caused by the EGR valve's closure. However, as shown in Figure 1-1 in the right-side plot, closing the EGR valve from point A to B increased $BSNO_X$ by 67 %. Also, retarding SOI from the MBT injection timing, which is 12 CA bTDC at this operating point, reduces NO_X with an increase in BSFC. Hence there exists a fundamental trade-off between NO_X and the fuel economy.

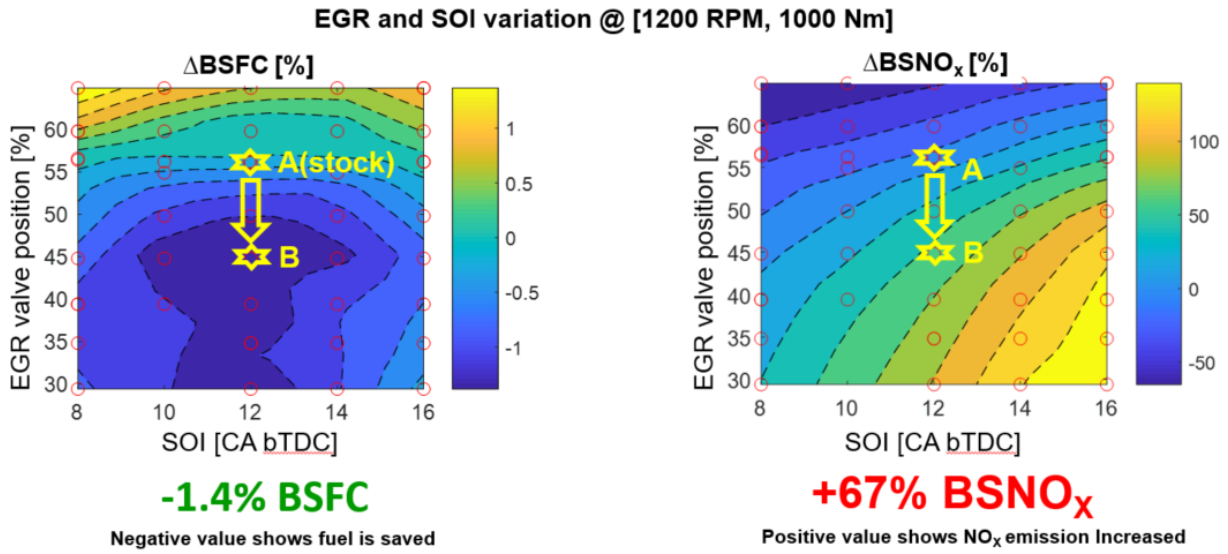

Figure 1-1: Comparison of brake specific fuel consumption and brake specific engine-out oxides of nitrogen with a change in the exhaust gas recirculation valve position and start of injection.

The upcoming emission standards like "CARB low NO_X Omnibus Rule", "EPA cleaner truck initiative," and "CARB advanced clean trucks rule" proposes a considerable challenge for automotive manufactures to reduce carbon dioxide (CO_2), which is a significant greenhouse gas (GHG), and reduce NO_X emission by more than 90% from the existing norm which is from 0.2 to 0.02 g/bhp-hr by 2027 time frame [6][9].

Conventional calibration schemes are developed based on steady-state operating conditions, and they are extrapolated or corrected for transient operating conditions. However, with the evolution of the above-said emission standards and more focus on control and monitoring of on-road emissions, advanced onboard adaptive calibration schemes are indispensable for negotiating the tradeoff between NO_X and BSFC on a rolling window basis. Model-based control can predict and take control actions to operate the engine at the most efficient regime. This thesis explores the opportunity to utilize route preview information with a model predictive controller (MPC), which manages to shift the engine set-points to achieve the best BSFC and correspondingly maintain the required SCR catalyst temperature to accommodate the increase in NO_X. MPC utilizes the route preview information to address the fundamental difficulty in controlling the slow SCR thermal dynamics. The various building blocks needed for the model and controller development are shown in Figure 1-2, and it is detailed in the below subsections.

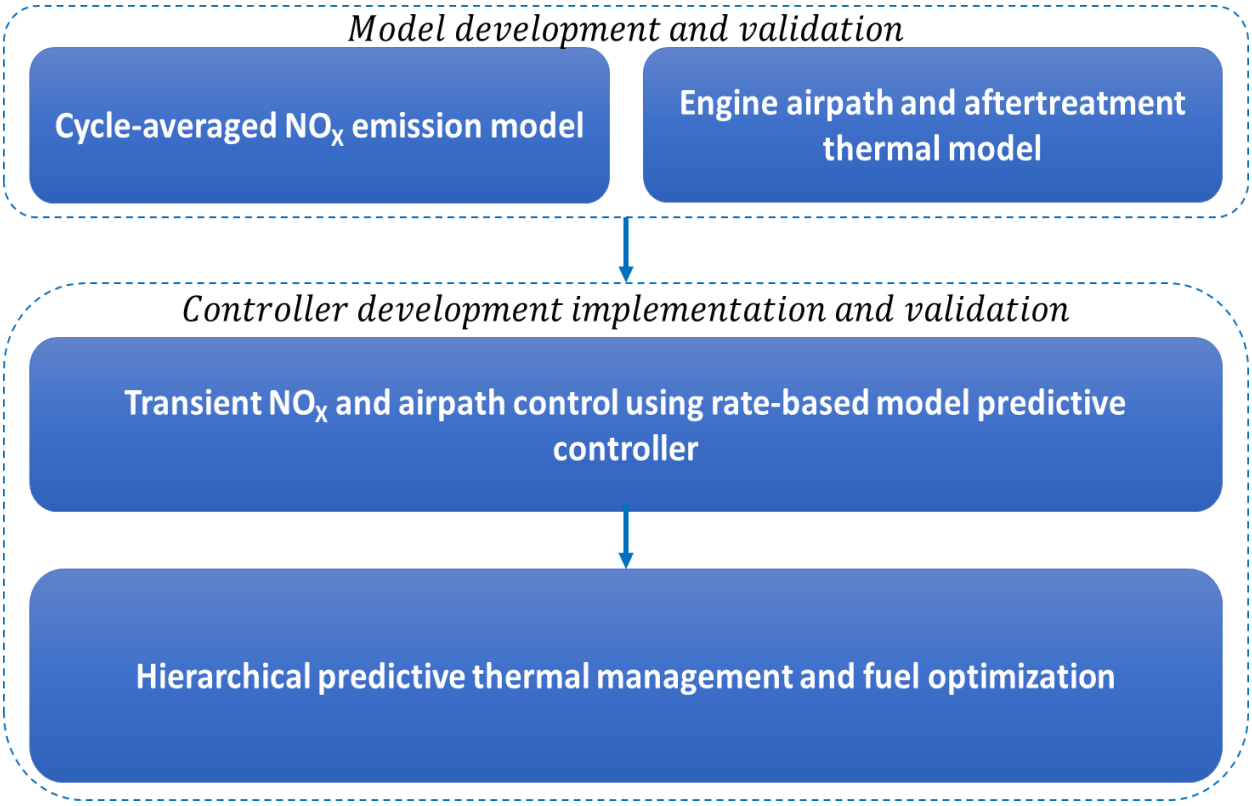

Figure 1-2: Major components of model and controller development

1.2 Cycle-averaged engine-out NO_X emission model

The literature on NO_X emission models show different model fidelity levels ranging from detailed crank angle resolved kinetic model as demonstrated by [10], which predict instantaneous in-cylinder NO_X concentration, to cycle-averaged models [11] where a cycle averaged NO_X concentration is predicted. As explained in [12], the detailed NO_X formation mechanism depends on the instantaneous concentration of reactants and the flame temperature. However, estimating these variables on a real-time basis in an automotive engine control unit is not feasible. In-cylinder pressure signals have proven to be a valuable parameter to estimate the flame temperature [13]. However, along with the additional cost to the engine, the use of in-cylinder pressure sensor-based NO_X models would reduce the control scope based on the measured in-cylinder pressure signal and limits its use to predict NO_X given the engine speed and torque preview.

Cycle-averaged NO_X models could be simplified to a lookup table, where the NO_X measured is mapped with corresponding engine speed and torque at different operating conditions. These empirical models are fast and accurate in the identified operating range but lack extrapolation capability from the nominal operating conditions. Also, extensive data collection is needed to cover the entire operating range. On the other hand, a semi-physical model combines the advantages of both physics-based models and empirical models [14]. In a semi-physical model, the underlying physical parameters are connected using first principles, and regression equations are used to express parameters that cannot be defined through first principles. A semi-physical model is explained in [15], where the in-cylinder pressure sensor signal is used to model a pseudo-multi-zone NO_X model. The heat release rate is estimated from the measured cylinder pressure data, and the NO_X thermochemical kinetics based on [12] is used to predict the NO_X formation. The semi-empirical model explained in [16] is derived from a zero-dimensional model, where the maximum burnt gas temperature is estimated based on the in-cylinder pressure signal, and it is correlated with NO_X. The resonance frequencies are tracked using cylinder pressure trace, and the trapped cylinder charge and the adiabatic flame temperature are estimated to predict NO_X formed [17]. A semi-empirical model is presented in [18] and [19], which are based on a set point-related formulation, where certain physically motivated empirical elements are introduced and identified using experimental data.

In this thesis, a semi-empirical NO_X model structure as presented in [19] is considered with inputs SOI, intake manifold pressure, engine speed, and torque. The NO_X model presented in [19] is also extended to include the effect of fuel injection rate shaping on NO_X, and an adiabatic flame temperature model, which would capture the impact of exhaust gas recirculation (EGR) is presented. A step-by-step procedure to identify the model parameters is also shown. The engine used in this research has a EGR valve arrangement, which controls both the EGR mass flow rate and flow to the turbine; thereby, the EGR mass and intake pressure variations are coupled. The model is formulated to work with the typical signals available on a production engine ECU. Specifically, the model can be used in an engine without an in-cylinder pressure sensor. Chapter two in this thesis covers the detailed architecture and experimental validation of this NO_X model.

1.3 Engine Airpath and Aftertreatment Thermal model

The development of physics-based models for the nonlinear air path system has been addressed well and used successfully by many authors [22] to [25] for different applications such as model-based control or calibration [26]. A reduced-order three-state airpath model for embedded application with Lyapunov control design and the associated model uncertainty due to the unaccounted states was presented in [27]. Further, a real-time cycle-averaged eight-state mean-value airpath model with the tuning procedure for the model parameters with least square optimization was explained in [28]. Feed gas emissions models have also been developed using semi-physical or grey box modeling approaches [29]. There is a strong need in the heavy-duty diesel engine research community to develop physics-based models with high prediction capability during transient and steady-state behavior prediction with low complexity and computational demand from a modeling perspective. To date, no literature exists in showing model-order reduction procedures for a complete diesel engine airpath and emission model.

Chapter three in this thesis shows the development of a physics-based full-order air path model for a modern air path system [64] in which the EGR valve controls both the EGR flow rate and intake manifold pressure. A step-by-step model order reduction procedure is presented to realize a low-order air path model and enable real-time implementation with the feasibility of using a higher discrete sampling time (10ms).

The reduced air path model is then used to calculate the input variables required for the cycle-averaged NO_X model explained in the previous section and provide engine out boundary conditions for the aftertreatment thermal model. With the three sub-models, the engine fuel efficiency and emissions are predicted on a rapid prototyping system. A gain scheduled PID controller for closed-loop control of engine torque is developed to manipulate the engine pedal and ensure tracking of the desired torque even when the control signals such as the EGR valve position deviate from a baseline position. A Smith predictor accounts for the feedback delay encountered during the real-time simulation to realize the controller. The feedback delay is caused due to the multiple hardware involved in the simulation loop, namely the dSPACE

controller, AVL Puma, and the engine. The discrete-time step in the controller is 10ms, and the feedback delay is 100 steps (identified using a dedicated experiment); since the feedback delay is more than the time step, the Smith predictor is used in estimating the current output of the system when the actual output feedback is not available. This research work's focuses on accurately modeling the EGR valve, which controls the EGR flow rate and flow to the turbine. This real-time implemented complete engine model that includes airpath, feed gas NO_X emission, and aftertreatment thermal states have the flexibility to simulate modern diesel engines and predict critical states like fuel economy and emissions. This aggregate model is later used for prediction in chapter 4 and chapter 5 in the hierarchical control design.

1.4 Rate-based model predictive controller

Fast engine out transient NO_X limits the SCR conversion efficiency due to the rapid depletion of NH_3 storage ratio in the SCR catalyst, thereby resulting in high tailpipe NO_X, also overdosing of NH_3 causes ammonia slip, which is a regulated pollutant [41]. Hence, in-cylinder NO_X control is required to manage NO_X during cold SCR temperatures and avoid transient engine-out NO_X spikes. However, in-cylinder NO_X control is costly because of the NO_X and fuel economy trade-off. Diesel engine airpath and emission formation are highly nonlinear, and the actuators have cross-sensitivity with other tracking variables. A multivariable feedback controller coordinating EGR and VGT for a gasoline engine is presented in [31]. This controller also accounts for the actuator redundancy and utilizes their cross-sensitivity to achieve demand torque and emissions. Classical control schemes need reference trajectories for the controller to track. Generating references on-board is computationally expensive. Moreover, references that are generated offline may not be optimal at all operating conditions. Last but not least, storing references that are generated offline would demand higher memory allocation. Fortunately, emission limits can be specified as constraints in modern controls, which avoid reference trajectory generation, but requires the real-time solution of a nonlinear optimization problem. In the literature, both linear and non-linear model predictive control (MPC) are widely explored for diesel engine airpath, emission, and aftertreatment control [[32]-[40]]. MPC offers a significant advantage in calibrating multi-input multi-output systems with its intuitive formulation and ability to handle constraints. The modern airpath controller needs to satisfy legislative constraints

like emissions and airpath structural safety constraints like intake manifold maximum pressure, turbocharger maximum speed, and exhaust gas maximum temperature.

Linear offset-free MPC [34] was of primary interest due to the controller's integral effect of achieving zero tracking error at a steady-state condition. In [36], two MPC methods are compared to achieve offset-free tracking. Firstly, using an integrator with actuator-saturation-based anti-windup logic and the Kalman filter to estimate plant-model mismatches. This study's results highlight the advantages of the Kalman-filter-based approach in the presence of system variability. Explicit MPC was preferred over online MPC due to the benefit of estimating MPC solutions with linear affine functions. Moreover, avoiding solving quadratic programs online, reduces the computational load. However, explicit MPC demands higher memory requirements to store explicit solutions covering multiple operating conditions and constraints. A comparison of the complexity of the online solution of active-sets quadratic programs versus the online evaluation of explicit solutions was presented in [36]. An explicit MPC formulation for an engine modeled with first-order transfer functions to control intake manifold pressure and compressor flow through EGR and VGT valve is presented in [37]. A second-order linear explicit rate-based MPC formulation for airpath management by coordinating VGT, EGR valve, and throttle actuators is presented [38]. This work highlights the advantage of scheduling a reduced number of plant realizations with the explicit rate-based formulation. A two-state second-order polynomial model for intake manifold pressure and EGR flow rate control was formulated as an unconstrained nonlinear program which is solved with an integration time step of 32 ms, and a control move made every 64 ms and prediction horizon of 320 ms [39]. Results in this paper show that nonlinear optimization is feasible on an ECU. A gain scheduled linear plant model identified using system identification, an explicit linear MPC formulation is solved with a sequential convex program [40]. A fast calibration technique is proposed to reduce the calibration effort with plant scheduling, and its efficacy is experimentally demonstrated in [40].

In chapter four, a rate-based MPC controller formulation to track a reference intake manifold pressure with engine-out NO_X emission constraint was presented. Conventional engine consists of a EGR valve and a waste gate to explicitly control EGR flow rate and intake manifold

pressure respectively. However, in this engine the arrangement of the EGR valve and the lack of a wastegate to explicitly control the intake manifold pressure challenges the control of boost and EGR flow rate by only using the EGR valve. For this reason, the start of injection (SOI) and EGR valve position is used as the control variables to track intake manifold pressure while satisfying engine-out NO_X constraint. EGR is primarily used for intake manifold pressure control and SOI is a fast actuator and hence it is efficient in controlling transient NO_X. This paper also shows the feasibility of using online MPC, achieved by avoiding plant scheduling and using a single plant model to cover the entire engine operating range. This is because full state feedback through measurements for all important states is used and the linear plant model is used to predict one-step ahead. This significantly reduced the controller calibration effort and memory requirement. The linear plant model used in the controller was obtained by linearizing the physics-based reduced-order airpath and the NO_X emission model presented in chapter 3. Full state feedback is achieved with the existing engine physical sensors, and the non-physical states are estimated using a Kalman filter. This rate-based MPC controller was experimentally validated in a hardware-in-the-loop setup with a gain-scheduled torque controller. Two different cases are compared; first, an unconstraint case in which the engine-out NO_X constraint was removed, and second, a constrained case in which the engine-out NO_X constraint is enforced.

1.5 Hierarchical predictive thermal management and fuel optimization

Integrated control of engine and aftertreatment realizes an adaptive online calibration scheme, where the fuel efficiency is maximized to its best subject to satisfying tailpipe NO_X emission constraint. This synergistic control skews the tradeoff between engine-out NO_X and fuel economy when the aftertreatment conversion efficiency allows it. For instance, when the SCR catalyst temperature is below light-off temperature, the drop in SCR NO_X conversion efficiency and the corresponding increase in tailpipe NO_X can be reduced by controlling the engine out NO_X. Similarly, when the SCR is warmed up, the engine calibration set points can be shifted to produce the best fuel economy, and the warmed-up SCR can efficiently reduce the corresponding increase in engine-out NO_X. The advantage of this control scheme is further leveraged using the vehicle route preview. The SCR efficiency depends significantly on the

catalyst temperature and ammonia (NH_3) storage ratio. The hydrolyzed urea injected at the urea mixer located upstream of SCR uses the exhaust energy to decompose into ammonia. The SCR thermal dynamics and the urea thermochemical reactions have very slow dynamics, so a long prediction horizon is needed to balance with future fuel savings the extra fuel consumed to operate the engine slightly inefficiently to generate the heat for the catalyst warm up. In this work, we only considered the thermal dynamics and assumed that the baseline controller will manage the ammonia dosage and storage. For best NO_X conversion efficiency, the SCR catalyst site needs to have an equimolar concentration of NO_X and NH_3. Other groups have used route preview information to help the controller predict the NH_3 storage requirement ahead of time and take corrective action to avoid NH_3 starvation or NH_3 slip.

Another assumption we made in our work is that the baseline engine controller maintains the desired ratio of nitrogen oxides in the engine-out exhaust. The ratio of NO_2 to NO_X in the engine-out NO_X significantly influences the SCR NO_X reduction efficiency. A ratio of 0.5 is reported to be optimal to facilitate both fast and slow reactions in the SCR [70]. In this current work we did not control the ratio of NO_2 to NO_X and it is controlled by the stock engine calibration.

Model predictive control was identified as an ideal candidate to handle time-delayed response and generating predictive control sequences based on preview information and the imposed constraints. In [41], an integrated emission management concept was introduced, where the optimal control problem is solved using Pontryagin's minimum principle (PMP), and the results show up to 3 % benefit in fuel economy and 2.5 % benefit in the total fluid cost (fuel cost + urea cost). In [42], an online causal equivalent emission minimization strategy (EEMS) to reduce both CO_2 and other emissions using optimization weight were presented. Further, the cycle dependence of the optimization weight was avoided by using an online adaptation derived using the Hamilton-Jacobi-Bellman equation and a physics-based approximation of the optimal cost-to-go function. The optimal control problem is solved using PMP. Results show that the EEMS strategies were very close to the theoretical non-causal optimum. However, the trip time needs to be known a priori to calibrate the optimization weight to satisfy the emission limit. In [43], a nonlinear model predictive controller-based diesel engine and SCR controls was proposed, with SOI and urea solution injection rate as the control inputs. Simulation results

under the US06 driving cycle show up to 9.36 % and 9.50 %, respectively, for lumped SCR systems and two cell SCR systems.

In [44], an integrated emission management problem was solved using dynamic programming (DP) and PMP. Further, compared with a sub-optimal real-time implementable strategy derived based on an equivalent consumption minimization strategy (ECMS). The results show that the sub-optimal solution deviates only by 0.16 % from the optimum. In [45], a reduced-order long-horizon predictive thermal management for diesel engine and aftertreatment system is presented. A static airpath model augmented with a three-state aftertreatment thermal model is used to explore the benefit of using long-horizon preview information of up to 30 s. The results show that the controller can achieve a faster warm-up of SCR at the expense of the fuel economy and recovers some of the initial fuel expense once the aftertreatment is warmed up. On a cycle averaged basis, the catalyst conversion efficiency increases to 4.5 % with a 3 % improvement in fuel economy. With the onset of connected autonomous trucks, research in predictive control of engine and aftertreatment is gaining significance due to preview information availability. In [46], an energy and emission-conscious adaptive cruise controller for a connected autonomous truck is presented. A 40 s preview information from the lead vehicle is utilized in deriving fuel and emission optimal speed planning. Simulation results show 5 – 15 % improvement in fuel economy is possible along with a 0 – 25 % reduction in tailpipe NO_X. The high-level controller can be designed to set the terminal constraint for the low-level controller and tracked in a receding horizon [46]. Table 1-1 compares important publications on the integrated engine and aftertreatment predictive control for this thesis work.

Table 1-1: Comparison of key publications on the integrated engine and aftertreatment predictive control with this thesis work

Control variables		Previous work					
		TNO Automotive [41] & [44]		ETH Zurich [42]	Ohio State University [43]	Volvo group Sweden [68]	Our Work
In-cylinder	(SOI/EGR/FRP/Pim)	EGR/VGT/DEF	EGR/VGT/DEF	SOI	SOI	Engine-out NOx	SOI/EGR/Pim
After treatment	Thermal Management	✓	✓	N/A	N/A	✓	✓
	Model based Urea injection	✓	✓	N/A	DEF injection rate	N/A	N/A
Simulation/Experiment		Simulation	Experiment	Simulation	Simulation	Simulation	Simulation/Experimental validation
Control formulation		Pontryagin Minimum Principle	Boundary surface Dynamic Programming RT-PMP	ECMS-based CO2 and tailpipe NOx optimal control Weight of the cost function expressed as HJB	Nonlinear MPC	Nonlinear MPC	High level controller- Nonlinear MPC Low level controller- Linear MPC
Sampling time [s]		N/A	N/A	1 s	Not given 150 s comp time for US06	N/A	High level controller 1 s Low level controller 0.01 s
Prediction horizon [s]		N/A	N/A	1800	10 steps	600	High level controller 20 s Low level controller 0.1 s
Year		2011	2014	2014	2015	2019	2021
Results		2-3 % reduction in fuel consumption and operating cost	Close to global optimal solution, with 0.16 % deviation from DP results	0.05 % CO2 0.104 % NOx	9.36 % fuel benefit 2.46 PPM NH_3 < 10 PPM 62.8 % lower tailpipe NOx	NOx is below a set reference (0.46 g/kWh).	0.8 % fuel benefit 13 % reduction in NOx tailpipe

In chapter five, a hierarchical predictive controller is introduced. As shown in Figure 1-3, the architecture consists of two MPC controllers with different prediction horizons. The different models developed in the previous chapters were utilized in designing the predictive controller architecture. The high-level (supervisory) controller utilizes a long prediction horizon of 20 s to provide fuel and NO_X emission optimal intake manifold pressure and SOI reference. The high-level controller uses a static airpath model to predict engine out exhaust temperature and exhaust mass flow rate which are used as an input to the dynamic aftertreatment thermal model. The low-level MPC controller utilizes a short prediction horizon of 0.1 s and tracks the reference intake manifold pressure and SOI; this controller is experimentally validated and presented in chapter 4. The low-level MPC controller also controls the fast transient engine-out NO_X spikes, which is enforced as a constraint. The torque controller along with the Smith predictor is used to track the demand engine torque, and a reference governor is used to regulate the engine air to fuel equivalence ratio λ above a reference λ_{ref} to avoid smoke. This complete control architecture was programmed and applied on a rapid prototype controller and validated in real-time through a software-in-the-loop (SIL) simulation with the nonlinear virtual engine model consisting of engine airpath, NO_X, and aftertreatment model.

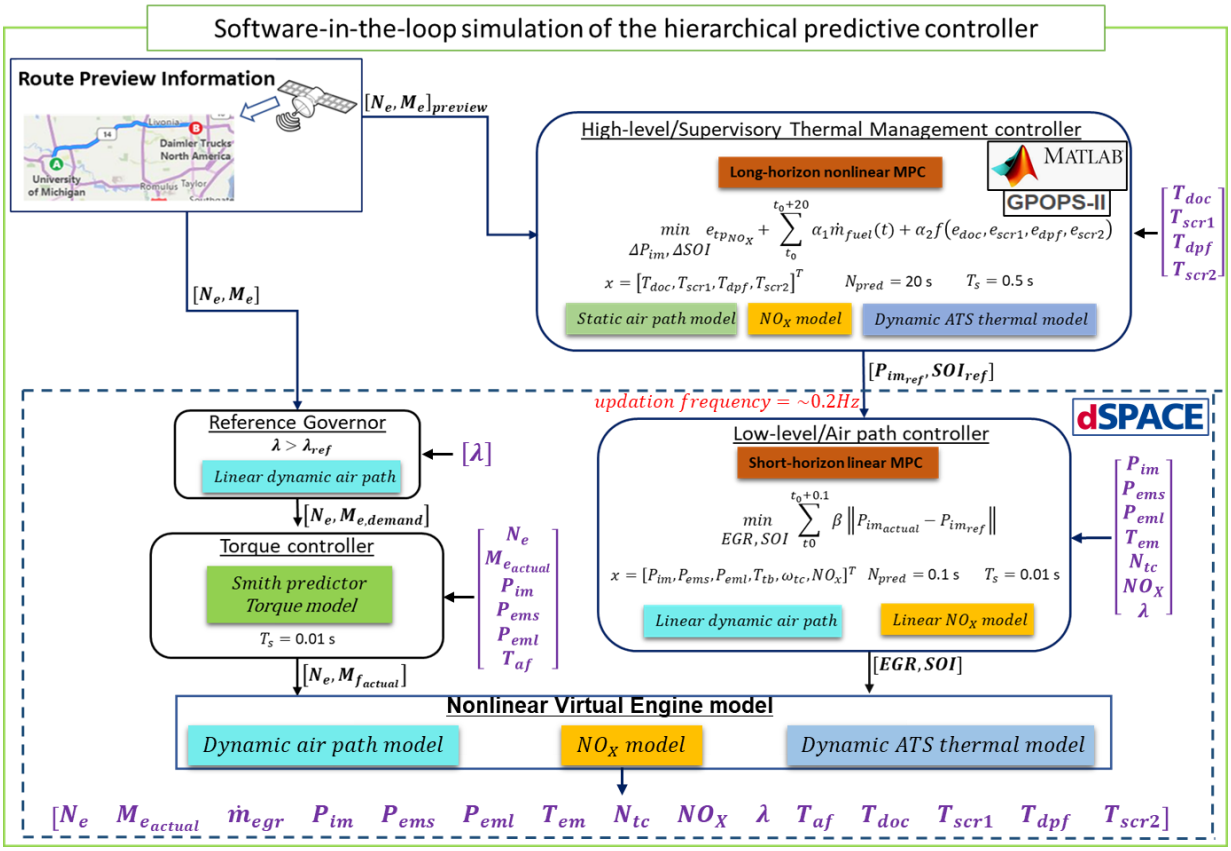

Figure 1-3: Integrated engine and aftertreatment control with hierarchical predict controller software-in-the-loop architecture

1.6 Thesis Outline and Contributions

It has been shown in the literature that the current heavy-duty diesel engine research focuses on improving fuel economy while addressing the upcoming very stringent emission norms. With the advancement in connectivity infrastructure, the availability of route preview information opens new avenues for real-time implementation of predictive control. To realize a real-time MPC, significant efforts have been made in designing this thesis research, and the controllers developed thereof to be practically implementable with the existing engine sensors.

Chapter 1 covers the modeling literature review and compares the state of the art on the integrated engine and aftertreatment predictive control. Chapter 2 shows the development and

experimental validation of a cycle-averaged NO_X emission model. Chapter 2 specifically highlights the physics-based engine-out NO_X model that can be used in the engine controller without in-cylinder pressure sensors. This model uses typical inputs which are available onboard in an engine control unit. Chapter 3 covers the development and validation of the engine airpath and aftertreatment thermal model. Key highlights of this chapter are the development of a nonlinear airpath model for a diesel engine with a EGR valve arrangement and the model order reduction to facilitate the use of a large integration time step from 0.1 ms to 10 ms for computational speed. Chapter 4 shows the control of transient NO_X and air path, using a rate-based model predictive controller. Key highlights of this chapter are the design of a rate-based model predictive controller to track a reference intake manifold pressure with instantaneous engine-out NO_X emission constraints and the hardware-in-the-loop experimental validation with the torque controller. Chapter 5 shows the Hierarchical predictive thermal management and fuel optimization. Specific highlights of this chapter are, design of hierarchical MPC to control slow aftertreatment states and fast airpath states and the design of hierarchical MPC to control slow aftertreatment states and fast airpath states. Chapter 6 concludes this thesis with specific observations made through this study and providing direction for future work.

The main contributions of this thesis are summarized as follows:

1. **NO_X model:** The first contribution of this work is to develop a physics-based NO_X emission model that can be used in predictive applications (i.e., without any sensor feedback or need for an in-cylinder pressure sensor). This model can accurately capture the fast transient $NO_{X,}$ and it can predict the effect in NO_X for change in engine calibration parameters like SOI, EGR, FRP, NOP, intake manifold pressure, and temperature. This work was presented and published at DSCC 2019 [20] and LDSC 2021 [21].
2. **Reduced-order airpath and aftertreatment thermal model:** Following the previous work, a full-order airpath model addressing the EGR valve, which controls both intake manifold pressure and EGR mass flow rate, is designed. A minimal realization of the full order model helped achieve a practically feasible integration time step (i.e., from 0.1 ms to 10 ms), which is experimentally validated. An aftertreatment thermal model and NO_X emission model are augmented with the reduced-order airpath model to evaluate the airpath model accuracy and

NO_X - thermal model robustness. This integrated model is a virtual engine model that serves for SIL and HIL simulations. Real-time implementation of this model in a rapid prototype controller and a gain-scheduled torque controller equipped with a Smith predictor to account for network communication delay was experimentally validated. This work was presented at SAE WCX 2020 [30].

3. **Rate-based model predictive controller:** A short-horizon predictive controller to track a reference boost pressure with NO_X constraint was developed. A rate-based MPC was designed based on the linearization of the previously developed virtual engine model. This controller avoids plant scheduling by using full state feedback from experimentally measured sensor signals, and the optimization is performed online. Experimental results show up to 1.4 % improvement in BSFC, 2 % reduction in engine-out NO_X, 40 % reduction in tailpipe NO_X, and a 6 % reduction in brake-specific Urea consumption (BSUC). This controller finds applicability in any hierarchical architecture or as a stand-alone controller. This work was accepted for publication and presentation at the IFAC E-COSM 2021.
4. **Hierarchical predictive controller for the integrated engine and aftertreatment control:** A hierarchical control architecture is conceptualized for the integrated engine and aftertreatment control. The supervisory controller utilizes a prediction horizon of 20 s to effectively control the slow aftertreatment thermal dynamics with the control inputs intake manifold pressure and SOI. The low-level controller has a short horizon of 0.1s, which tracks the reference boost with transient NO_X control enforced as a constraint. This hierarchical control architecture is real-time implementable, and it is validated by implementing this architecture in a rapid prototype controller. Real-time SIL simulation results show fuel benefit along with faster aftertreatment warm-up.

Chapter 2 Cycle-averaged Physics-based NOx Model

In this chapter, a semi-empirical NO_X model structure, as presented in [19], is considered and extended to include the effect of fuel injection pressure, injection rate shaping on NO_X and an adiabatic flame temperature model, which would capture the effect of exhaust gas recirculation (EGR) is presented. Besides, a step-by-step procedure to identify the model parameters is shown. The engine has a EGR valve arrangement, which controls both the EGR mass and the turbine flow. Thereby the EGR mass and intake pressure variations are coupled. Also, the model works with the typical signals which are available on a production engine ECU. Specifically, the model can be used in an engine without in-cylinder pressure sensors. The model is experimentally validated on a heavy-duty engine, and the NO_X prediction is compared with measurements from a CLD500 fast NO_X analyzer to check the model's capability to predict NO_X during steady-state and transient engine operations.

2.1. Cycle averaged NOx model

The NO_X model predicts the engine-out NO_X emissions in a cycle averaged basis (i.e., $\hat{n}_{NO_x}$ in mole/volume of exhaust gas). As shown below in (2.1), a global NO_X formation reaction is considered with NO and NO_2 as NO_X constituents.

$$\frac{1}{2}N_2 + \frac{x}{2}O_2 \underset{r_{bw}}{\overset{r_{fw}}{\rightleftarrows}} (2-x)NO + (x-1)NO_2 \equiv NO_X \qquad (2.1)$$

Where, r_{fw} and r_{bw} are the forward and backward reaction rates, respectively. In this work, engine-out NO_X concentration is assumed to be composed of 80 % NO and 20 % NO_2 by volume at all engine operating conditions. Experimental results performed on the engine shown in Figure 2-3 with the baseline engine controller verify this ratio at a wide range of conditions shown in Figure 2-1. Therefore, the stoichiometric coefficient x is assumed to be 1.2. The effect of

individual engine actuators in altering NO to NO_X ratio which is studied in [71] is not considered in this study. Also, the effect of the pilot, post, and other multiphase injection strategies on NO_X are ignored for his study. The start of injection SOI defined in this thesis refers to the main injection timing. The amount of in-cylinder residual gas compared to the external EGR is very negligible. Thus, the in-cylinder residual gas effect on NO_X is also neglected.

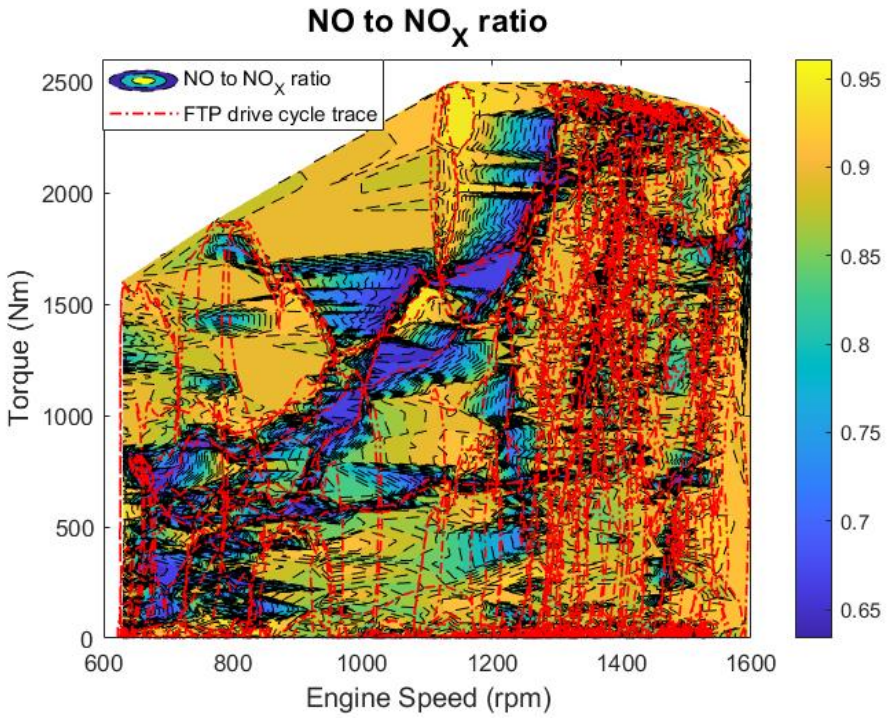

Figure 2-1: Comparison of nitrogen monoxide to nitrogen oxides ratio at different operating points collected over a federal test procedure cycle

Oxides of nitrogen are mainly formed at the flame front, where the gas's temperature is higher than 2000 K in the presence of oxygen and nitrogen molecules [49]. In a diesel engine, the NO_X formation predominantly occurs in a crank angle window between the start of combustion, which is assumed as 10 % mass fraction of fuel burnt (CA10) to 90 % mass fraction of fuel burnt (CA90). Experimental data at different engine operating points shows that the duration between CA10 and CA90 is ~30 crank angle degrees. Hence, the start of combustion to 30 degrees after the start of combustion is considered as the NO_X formation duration. Thus one

can calculate the number of moles of NO_X (n_{NOx}) formed on a cycle averaged basis by the product of the gas volume (V_{reac}) undergoing the reaction and the difference between the forward reaction rate (r_{fw}) and backward reaction rate (r_{bw}) integrated over the NO_X formation duration [19]

$$n_{NOx} = \int_{\varphi SOC}^{\varphi SOC+30^0} V_{reac}(\varphi)\left[r_{fw}(\varphi) - r_{bw}(\varphi)\right]d\varphi. \tag{2.2}$$

By the rate law,

$$r_{fw}(\varphi) = K_{fw}\left(\theta(\varphi)\right)\,[\mathrm{N_2}]^{0.5}\;\;[\mathrm{O_2}]^{0.6}, \tag{2.3}$$

$$r_{bw}(\varphi) = K_{bw}\left(\theta(\varphi)\right)\;\;[\mathrm{NO_x}], \tag{2.4}$$

with K_{fw} as the forward reaction constant and K_{bw} as the backward reaction constant.

To avoid the crank angle (φ) resolved reaction zone volume $V_{reac}(\varphi)$, it is represented as an approximated scalar value $\tilde{V}_{reac}$. Hence the approximated number of NO_X moles $\tilde{n}_{NO_x}$ is given by

$$\tilde{n}_{NOx} = \tilde{V}_{reac}\int_{\varphi soc}^{\varphi soc+30^0}\left[k_{fw}\left(\theta(\varphi)\right)\,[N_2]^{0.5}\,[O_2]^{0.6} - k_{bw}\,\left(\theta(\varphi)\right)\,[NO_x]\right]d\varphi\,. \tag{2.5}$$

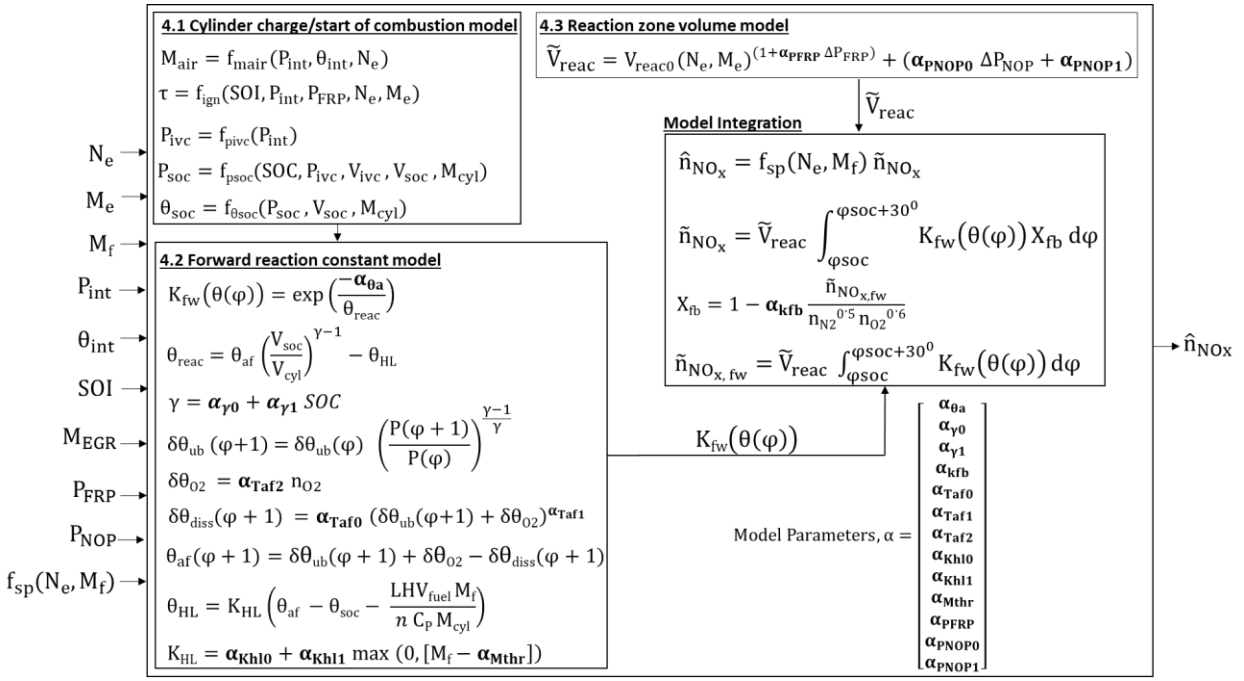

Figure 2-2: Overall structure of the model showing the model inputs and output

One can define the ratio of forward to the backward reaction X_{fb} as

$$X_{fb} = \left\{1 - \frac{k_{bw}(\theta(\varphi))\,[NO_x]}{K_{fw}(\theta(\varphi))\,[N_2]^{0.5}\,[O_2]^{0.6}}\right\}. \tag{2.6}$$

The NO_X concentrations $[NO_X]$ in (2.6) are approximated as the end of combustion concentration, and it are produced by the forward reaction. The concentrations of n_{N_2} and n_{O_2} are concentration at the beginning of combustion. Further, the gas concentrations are represented in moles per unit volume (2.6) becomes

$$X_{fb} = \left\{1 - \frac{k_{bw}(\theta(\varphi))}{k_{fw}(\theta(\varphi))}\,\frac{(V^{0.5})_{N_2}\;(V^{0.6})_{O_2}}{(V)_{NOx}}\;\frac{n_{NOx,fw}}{(n^{0.5})_{N_2}\,(n^{0.6})_{O_2}}\right\}. \tag{2.7}$$

Assuming the ratio of reaction constants and volume will not change between operating conditions [19], a model parameter ($\alpha_{K_{fb}}$) is introduced

$$\alpha_{K_{fb}} = \frac{k_{bw}\big(\theta(\varphi)\big)}{k_{fw}\big(\theta(\varphi)\big)} \frac{(V^{0.5})_{N_2}\,(V^{0.6})_{O_2}}{(V)_{NOx}}. \tag{2.8}$$

Substituting α_{Kfb} in (2.7),

$$X_{fb} = \left\{1 - \alpha_{K_{fb}} \frac{n_{NOx,fw}}{(n^{0.5})_{N2}\,.\,(n^{0.6})_{O2}}\right\}. \tag{2.9}$$

Then (2.5) can be written as

$$\tilde{n}_{NO_x} = \tilde{V}_{reac} \int_{\varphi soc}^{\varphi soc+30^0} K_{fw}\big(\theta(\varphi)\big)\,[N_2]^{0.5}\,[O_2]^{0.6}\,X_{fb}\,d\varphi. \tag{2.10}$$

The concentrations of $[N_2]$ and $[O_2]$ in (2.10) are neglected because the effect of oxygen concentration is captured in the adiabatic flame temperature model explained later. The ratio of forward to the backward reaction X_{fb} partially accounts for the effect of N_2 and O_2 concentration. Hence, the NO_X formed in the forward reaction $\tilde{n}_{NO_{x,fw}}$is given by

$$\tilde{n}_{NO_{x,fw}} = \tilde{V}_{reac} \int_{\varphi soc}^{\varphi soc+30^0} K_{fw}\big(\theta(\varphi)\big)\,d\varphi\,. \tag{2.11}$$

The approximated number of moles of NO_X formed in a cycle is given by

$$\tilde{n}_{NO_x} = \tilde{n}_{NO_{x,fw}}\,X_{fb}. \tag{2.12}$$

The approximated number of moles of NO_X denoted as $\tilde{n}_{NOx}$ in (2.12) is further corrected with a calibration factor f_{sp} to calculate the final estimate of NO_X denoted as $\hat{n}_{NOx}$. The calibration factor is stored as an offline map referenced versus engine speed and mass of fuel

$$f_{sp}\big(N_e, M_f\big) = \frac{n_{NO_x,sp}\big(N_e, M_f\big)}{\tilde{n}_{NO_x,sp}\,\big(N_e, M_f\big)}. \tag{2.13}$$

The estimated number of moles of NO_X formed in a cycle is given by

$$\hat{n}_{NO_x} = f_{sp}\big(N_e, M_f\big)\,\tilde{n}_{NO_x}. \tag{2.14}$$

It is important to note here that $\hat{n}_{NO_x}$ is the final NO_X estimated by the model and $\tilde{n}_{NO_x}$ is the approximated NO_X that is based on (2.5) that avoids the crank angle resolved terms.

2.2. Experimental setup and parameter tuning procedure

This research aims to develop a cycle-averaged NO_X model that could be implemented using the standard signals available in the conventional engine control unit. Figure 2-2 shows the model's overall structure with speed and torque as the exogenous inputs. Other inputs from the ECU are the mass of fuel M_f, the mass of exhaust gas recirculation M_{EGR}, the start of injection timing SOI, fuel rail pressure $P_{FRP,}$ and needle opening pressure P_{NOP}. Intake manifold pressure P_{int} and temperature θ_{int} are highly dependent on the engine operating environment, and these parameters can be estimated or measured. The scaled parameter $\tilde{n}_{NOx}$ is modeled based on the physical relation between NO_X and engine operating point specific parameters SOI, M_{EGR}, P_{int}, $P_{FRP,}$ and P_{NOP}.

A 12.8 L heavy-duty diesel engine is used in this work with specifications listed in Table 2-1. Figure 2-3 shows the engine's schematic layout. Varying the EGR valve position will directly control the EGR flow rate and the turbine's small scroll flow rate. So, the M_{EGR} and P_{int} sweeps are coupled. The NO_X model parameters are identified using experimental data collected at 102 steady-state operating points (setpoints) and a single parameter variation sweep at ten different operating points, as shown in Figure 2-4. Single parameter variation includes SOI, M_{EGR}/P_{int}, P_{FRP}, and P_{NOP}. Two different NO_X measurement devices, the stock engine NO_X sensor and the state-of-the-art fast NO_X analyzer having high response time were used to capture NO_X's transient behavior. The model parameters are identified by solving an optimization problem to minimize the sum of squared errors between the estimate $\hat{Y}$ and measured variable Y.

$$J = \frac{1}{N}\sum_{k=1}^{N}\left|Y(k) - \hat{Y}(k)\right|^2 \tag{2.15}$$

Table 2-1: Engine and NO_X measurement analyzer specification

Engine	**Make**	**Detroit Diesel Corporation**
	Displacement	12.8 L
	Number of cylinders	Inline 6
	Rated Power	375 kW at 1625 RPM
	Rated Torque	2400 Nm at 1075 RPM
	Turbo	Fixed vane turbo without wastegate
	Fuel Injection	1 main injection and 2 post injection
NOx sensor	Make	Continental
	Measurement principle	ZrO_2 based
	Response time	1 second
	Accuracy	±5% of fullscale
CLD500 fast NOx analyzer	Make	Cambustion
	Measurement principle	Chemi-Luminescence
	Response time	10ms
	Accuracy	±1% of the full scale

A setpoint relative model only has to reproduce the output's change relative to its reference value for deviations from these setpoints. The engine control parameters' variation limits are decided based on transient deviations, which the engine encounters during an aggressive transient test cycle. Also, the bounds of variations are limited by peak cylinder pressure, exhaust gas temperature, and the fuel pump's mechanical capability. All the steady-state data were collected at standard test conditions, engine out coolant temperature at 95 ℃, relative humidity 50 %, and 25 ℃ room and intake air temperature.

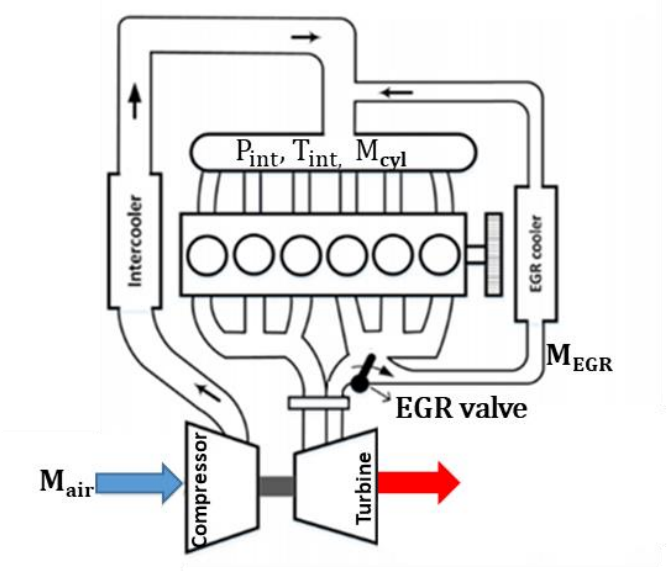

Figure 2-3: Schematic layout of engine showing the exhaust gas recirculation valve

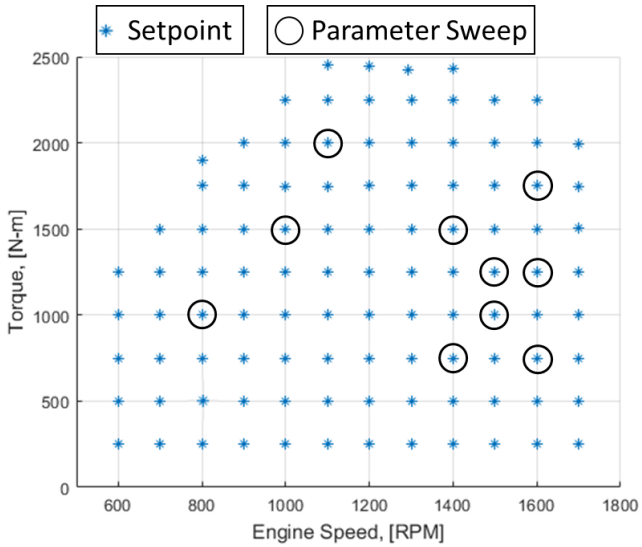

Figure 2-4: Engine operating range showing the selected setpoints (marked as a star) and parameter sweep points tested on the engine (marked with a circle).

Throughout the variation sweep data collection process, the nominal point NO_X value repeatability needs to be ensured, as drifting in nominal value between tests would result in severe error propagation in the identification process. The NO_X sensor is sensitive to water

condensation in the exhaust pipe. Operating the engine at low and mid-loads for a long time will make the sensor provide erroneous NO_X measurement due to water condensation. To avoid this, the test sequence is designed with alternate low and high load points. The step-by-step identification procedure is summarized and shown in Figure 2-14. The calibration factor (f_{sp}) during identification processes is unity.

2.3. NOx model implementation

Figure 2-2 shows the complete structure of the NO_X model. The critical components of the model are the cylinder charge estimation M_{cyl}, forward reaction constant $K_{fw,}$ reaction zone volume V_{reac} and the calibration factor f_{sp}. Physical parameters are introduced in calculating these components of the model. The identification process for each parameter of the model is explained in the below subsections.

2.3.1 Cylinder charge and the start of the combustion model

The cylinder charge M_{cyl}, estimation is based on the speed density relation [50]. The volumetric efficiency η_{vol} is a critical parameter for cylinder charge estimation, and it depends on the engine speed N_e, intake temperature θ_{int}, and pressure P_{int}. A linear polynomial fit, as shown in (2.17) is used to obtain the volumetric efficiency.

$$M_{air} = \eta_{vol} * \frac{P_{int} * V_{disp} * N_e}{2 * R * T_{int}} \tag{2.16}$$

$$\eta_{vol} = \alpha_1 + \alpha_2 * P_{int} + \alpha_3 * P_{int}^2 + \alpha_4 * P_{int}^3 + \alpha_5 * N_e + \alpha_6 * \sqrt{N_e} + \alpha_7 * N_e^2 + \alpha_8 * \theta_{int} \tag{2.17}$$

$$M_{cyl} = M_{air} + \mathrm{M_{EGR}} \tag{2.18}$$

The parameters α_1 to α_8 are identified using steady-state data collected at setpoints. Ignition delay (τ) and temperature of cylinder charge at the start of combustion (θ_{soc}) are the two parameters estimated from the combustion model. The ignition delay period depends on the SOI, P_{int}, P_{FRP}, N_e, and M_e as shown in (2.19). The model works by capturing the ignition delay

variation when the above said parameters are changed from the setpoint's nominal value. The ignition delay (τ) is given by,

$$\tau = \tau_0(N_e, M_e) + \tau_p * \Delta P_{int} + \tau_{rp} * \Delta P_{FRP} + \tau_{SOI} * \Delta SOI, \quad (2.19)$$

$$\Delta P_{int} = P_{int0}(Ne, Me) - P_{int}, \quad (2.20)$$

$$\Delta P_{FRP} = P_{FRP0}(Ne, Me) - P_{FRP}, \quad (2.21)$$

$$\Delta SOI = SOI_0(Ne, Me) - SOI, \quad (2.22)$$

where τ_0 is the ignition delay calculated at the setpoints, and it is stored as a map referenced with engine speed and torque. The model parameters τ_p, τ_{rp} and τ_{SOI} are identified individually using sweeps with a single parameter variation of P_{int} or P_{FRP} or *SOI*, respectively. To identify these parameters, SOC measured with a cylinder pressure sensor is used. The crank angle at 10 % mass fraction burned (CA10) is assumed as the start of the combustion crank angle. The temperature and volume of charge at the start of combustion θ_{soc} depends on the pressure at SOC (P_{soc}) and volume at SOC (V_{soc}), and mass of cylinder charge (M_{cyl}). The volume of the cylinder at intake valve closure V_{ivc} is a constant as the valve timing is fixed. Therefore, θ_{soc} is calculated using equation (2.23) to (2.26)

$$\theta_{soc} = \frac{P_{soc} * V_{soc}}{M_{cyl} * R}, \quad (2.23)$$

$$P_{soc} = P_{ivc}\left(\frac{V_{ivc}}{V_{soc}}\right)^k \quad (2.24)$$

$$P_{ivc} = p_0 * P_{int} \quad (2.25)$$

$$k = k_0 + k_1 * \frac{1}{M_{cyl}} \quad (2.26)$$

where the parameters p_0 , k_0 and k_1 are identified using the measured P_{ivc} and P_{soc} from the cylinder pressure data collected at setpoints. Figure 2-5 compares the measured and estimated

P_{soc} for different steady-state operating points. Results show that the estimation error is smaller than $\pm$ 5%.

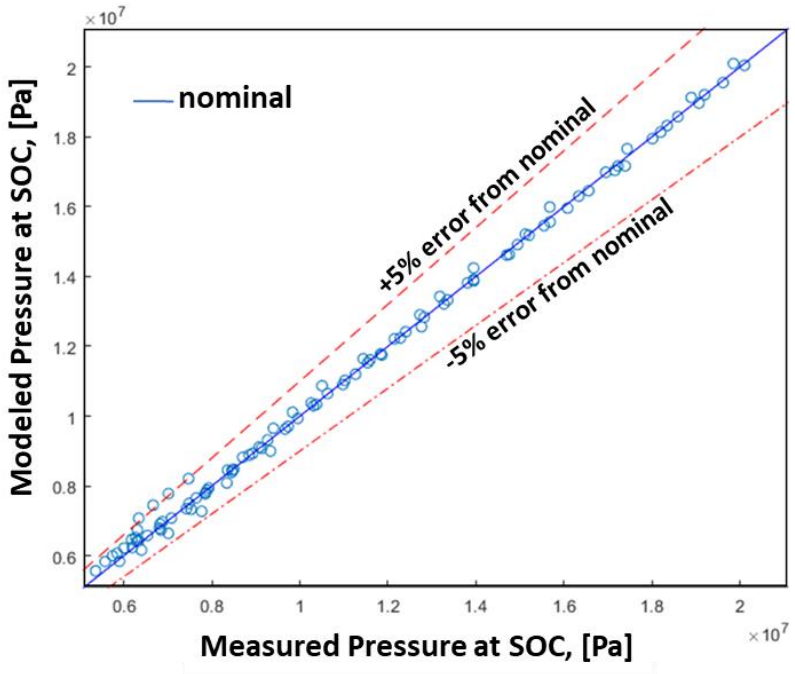

Figure 2-5: Comparison between measured and modeled cylinder pressure at start of combustion

2.3.2 Forward reaction constant model

Based on the Arrhenius law [19], the forward reaction constant (K_{fw}) depends on the activation temperature ($\alpha_{\theta a}$) and the reaction zone temperature (θ_{reac}).

$$K_{fw}\big(\theta(\varphi)\big) = A\ exp\left(\frac{-\alpha_{\theta a}}{\theta_{reac}}\right) \tag{2.27}$$

The pre-exponential factor (A) is assumed to be unity, and the actual value of A is lumped with reaction zone volume ($\tilde{V}_{reac}$) identification, explained later in section 2.4.3. As (2.27) suggests, the higher is the activation temperature slower, the forward reaction rate, and the amount of NO_X formed. Similarly, for a constant activation temperature $\alpha_{\theta a}$ the reaction constant K_{fw} increases with an increase in the reaction zone temperature θ_{reac} as the molecules gain more energy to cross the energy barrier to become the product. The Reaction zone temperature (θ_{reac}) is

modeled as the difference between the flame temperature and the temperature lost to the surrounding gases around the flame front (θ_{HL}).

$$\theta_{reac} = \theta_{af} * \left(\frac{V_{SOC}}{V_{cyl}(\varphi)}\right)^{\gamma-1} - \theta_{HL}. \tag{2.28}$$

Assuming the isentropic process, the adiabatic flame temperature θ_{af} is corrected with the ratio of volumes at SOC and volume of the cylinder between SOC to 30 degrees after SOC using $\left(\frac{V_{SOC}}{V_{cyl}(\varphi)}\right)^{\gamma-1}$, where γ is the isentropic exponent. The isentropic exponential, which is explained later (2.36) in the paper, depends on the injection angle's start and thus varies from cycle to cycle. Hence, the reaction zone temperature (θ_{reac}) is a vector calculated for each engine cycle from SOC to 30 degrees after SOC. The adiabatic flame temperature estimation based on the in-cylinder pressure sensor is addressed in the literature [14] and [15]. However, in this work, a physics-based model is intended to avoid the need for a sophisticated cylinder pressure sensor. To this end, the Adiabatic flame temperature is a function of temperature rise due to compression of unburned gas $\delta\theta_{ub}$, the temperature rise due to combustion of fuel $\delta\theta_{O2}$ and the gas dissociation $\delta\theta_{diss}$ [16] as shown in Figure 2-6.

$$\theta_{\mathrm{af}}(\varphi+1) = \delta\theta_{\mathrm{ub}}(\varphi+1) + \delta\theta_{\mathrm{O2}} - \delta\theta_{\mathrm{diss}}(\varphi+1) \tag{2.29}$$

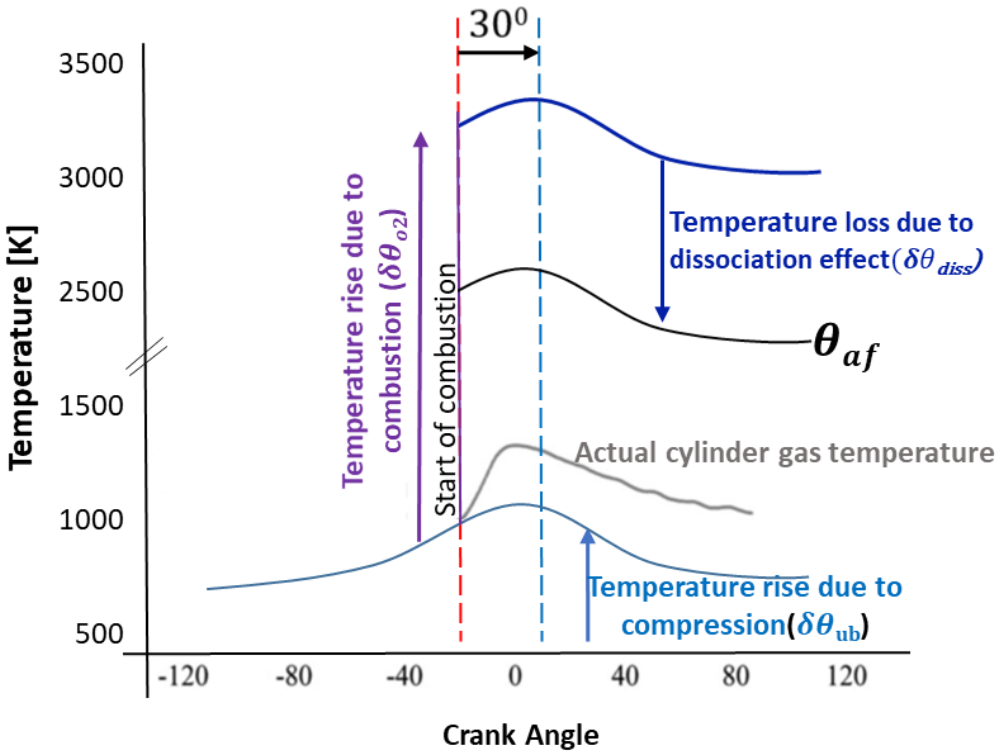

Figure 2-6: Different components of the adiabatic flame temperature model

From the combustion model, the pressure and temperature at the start of combustion is known, further the cylinder pressure trace due to compression $\delta\theta_{ub}$ is obtained using ideal gas law, as shown in (2.30).

$$\delta\theta_{ub}(\varphi+1) = \delta\theta_{ub}(\varphi)\left(\frac{P(\varphi+1)}{P(\varphi)}\right)^{\frac{\gamma-1}{\gamma}}. \tag{2.30}$$

Where,

$$P(\varphi+1) = \frac{M_{cyl}\, R\, \delta\theta_{ub}(\varphi)}{V_{CYL}(\varphi+1)} \tag{2.31}$$

With initial conditions:

$$\delta\theta_{ub}(\varphi = \varphi_{soc}) = \theta_{SOC} \text{ and} \tag{2.32}$$

$$P(\varphi = \varphi_{soc}) = P_{SOC}. \tag{2.33}$$

The temperature rise due to combustion is given by,

$$\delta\theta_{O_2} = \alpha_{Taf2} \times n_{O2} \tag{2.34}$$

Where n_{O2} is the concentration of oxygen before combustion. The temperature lost due to dissociation of gases is accounted by,

$$\delta\theta_{diss}(\varphi) = \alpha_{Taf0}[\delta\theta_{ub}(\varphi) + \delta\theta_{O2}]^{\alpha_{Taf1}} \tag{2.35}$$

with α_{Taf0}, α_{Taf1} and α_{Taf2} as model parameters identified using M_{EGR}/P_{int} variation sweep. As explained earlier, due to the unique design of this engine's air path, the M_{EGR} and P_{int} variations are coupled (i.e., changing the EGR valve would change both intake pressure and M_{EGR}). The concentration of n_{O2} changes with EGR variation. The target adiabatic flame temperature is calculated by identifying the adiabatic flame temperature at each operating point using EGR variation sweep data and the parameters α_{Taf0}, α_{Taf1}, and α_{Taf2} are identified and validated as shown in Figure 2-7. The isentropic exponent is a significant factor that controls the reaction zone temperature, and it is linearly correlated with the SOC using the initial conditions provided in Table 2-2, the model parameters $\alpha_{\gamma 0}$ and $\alpha_{\gamma 1}$ as shown in (2.36) and α_{kfb} shown in (2.9) are identified with SOI variation sweep shown in Figure 2-8.

$$\gamma = \alpha_{\gamma 0} + \alpha_{\gamma 1} SOC, \tag{2.36}$$

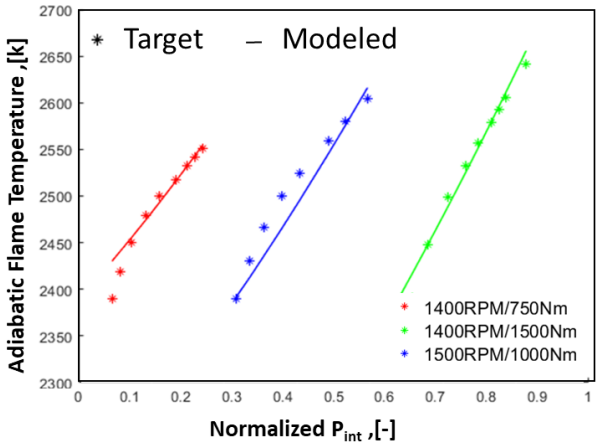

Figure 2-7: Comparison of adiabatic flame temperature target and modeled for different intake pressure

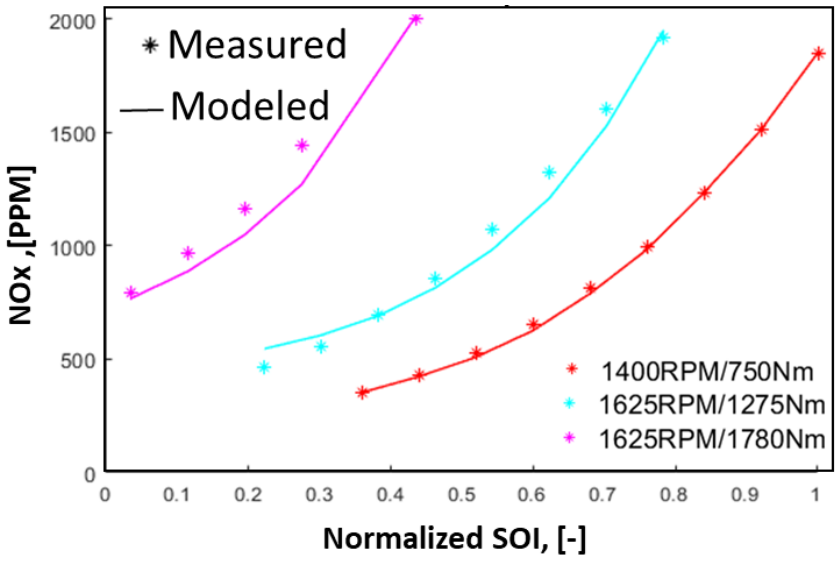

Figure 2-8: Comparison of measured and modeled nitrogen oxides with the identified parameters for different start of injection.

The reaction zone temperature θ_{reac} in (2.28) depends on the adiabatic flame temperature (2.29) and the temperature lost to the surroundings gas θ_{HL}. This depends on the temperature difference between the NO_X formation zone temperature, which is assumed to be the adiabatic flame temperature θ_{af} and the surrounding gas temperature θ_{surr}.

$$\theta_{HL} = K_{HL}\left(\theta_{af} - \theta_{surr}\right) \tag{2.37}$$

$$K_{HL} = \alpha_{KHL0} + \alpha_{KHL1} * max\left(0, \left[\alpha_{Mthr} - M_f\right]\right)^2 \tag{2.38}$$

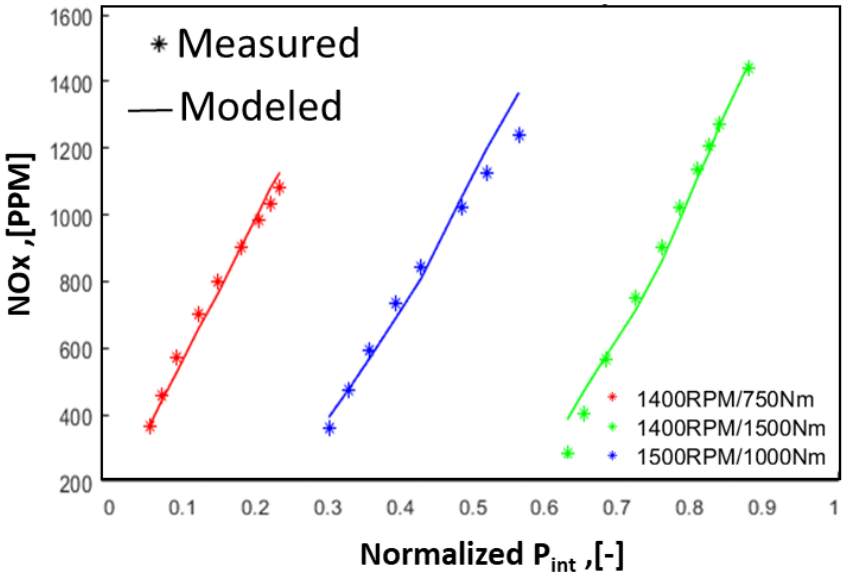

Figure 2-9: Comparison of measured and modeled nitrogen oxides with the identified parameters for different intake manifold pressure.

The heat transfer coefficient K_{HL} (a dimensionless number) is a lumped parameter that depends on the fuel-injected quantity. The higher the fuel quantity, the larger the boundary surrounded by the burned gas; hence the formation zone interaction with the cooler charge is less; in that condition, the heat transfer to the surrounding gas is less, so the heat transfer coefficient can become negative. A fuel threshold α_{Mthr} is introduced to identify the quantity of fuel above which the heat transfer is negative, at which the NO_x formation zone gains heat from the burned gas [19]. The temperature of the charge surrounding the formation zone θ_{surr} is the sum of the charge temperature at SOC and the rise in temperature due to burned gas in the cylinder, which is the temperature rise due to fuel burned, as shown in (2.39).

$$\theta_{surr} = \theta_{SOC} + \frac{LHV\ M_{fuel}}{n\ C_p\ M_{cyl}} \tag{2.39}$$

Where n is the fraction of cylinder mass, which absorbs the heat released by combustion of fuel, here a value of n = 0.5 is used [19] and [51].

2.3.3 Reaction zone volume

The reaction zone volume V_{reac} is the volume of gas undergoing the reaction to form NO_X. The reaction zone volume $\tilde{V}_{reac}$ depends on the engine speed N_e, Torque M_e, fuel rail pressure $P_{FRP,}$ and needle opening pressure P_{NOP}.

$$\tilde{V}_{reac} = [V_{reac0}(N_e, M_e)]^{(1+\alpha_{PFRP}*\Delta P_{FRP})} + \alpha_{PNOP0} * \Delta P_{NOP} + \alpha_{PNOP1} \quad (2.40)$$

$$\Delta P_{FRP} = P_{FRP0}(N_e, M_e) - P_{FRP} \quad (2.41)$$

$$\Delta P_{NOP} = P_{NOP0}(N_e, M_e) - P_{NOP} \quad (2.42)$$

V_{reac0} is the nominal reaction zone volume calculated at each setpoint where ($\Delta P_{FRP} = \Delta P_{NOP} = \alpha_{PNOP1} = 0$), and it is stored as a map referenced with speed and torque. The parameters α_{PFRP}, α_{PNOP0} and α_{PNOP1} used in (2.40) are identified in the following two steps.

Step 1: α_{PFRP} is identified using the fuel rail pressure sweep data with setpoint P_{NOP} and V_{reac0}, the results are validated, as shown in Figure 2-10.

Step 2: Needle opening pressure P_{NOP} is another variable for this engine, which varies the fuel injection rate shaping, as shown in Figure 2-11. Different rate shapes of injection have a significant effect on NO_X and fuel economy. α_{PNOP0} and α_{PNOP1} are used to capture the effect of P_{NOP} on $V_{reac.}$ P_{NOP} changes the injection rate shape, and its effect is included as $(\alpha_{PNOP0} * \Delta P_{NOP} + \alpha_{PNOP1})$ in (2.40).

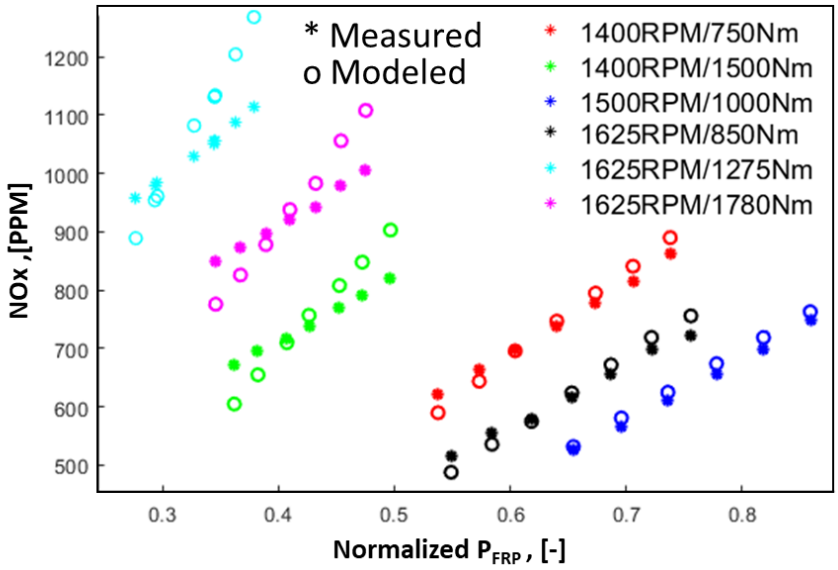

Figure 2-10: Comparison of measured and modeled nitrogen oxides for different fuel rail pressure.

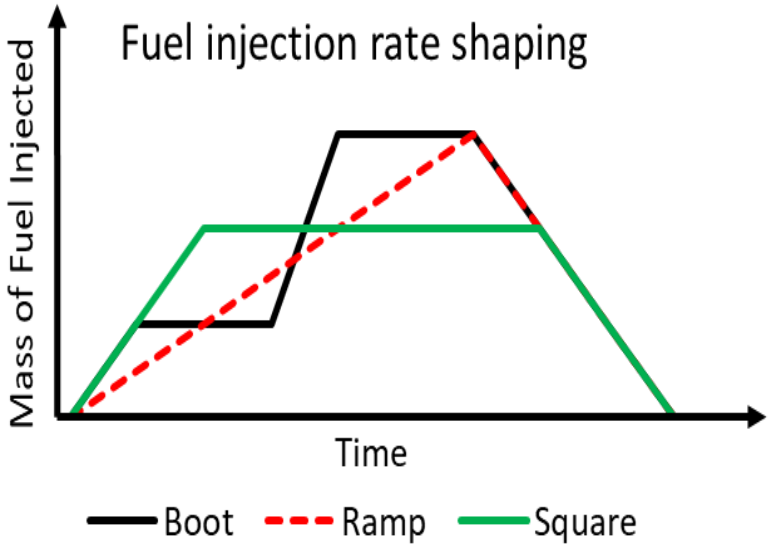

Figure 2-11: Comparison of different injection rate shaping which are switched through needle opening pressure variations.

A nominal map for P_{NOP} is created with the steady-state data. Using the P_{NOP} sweep data and the value of V_{reac0}, α_{PFRP} identified in step 1 and 2, respectively, identify α_{PNOP0} and α_{PNOP1}.

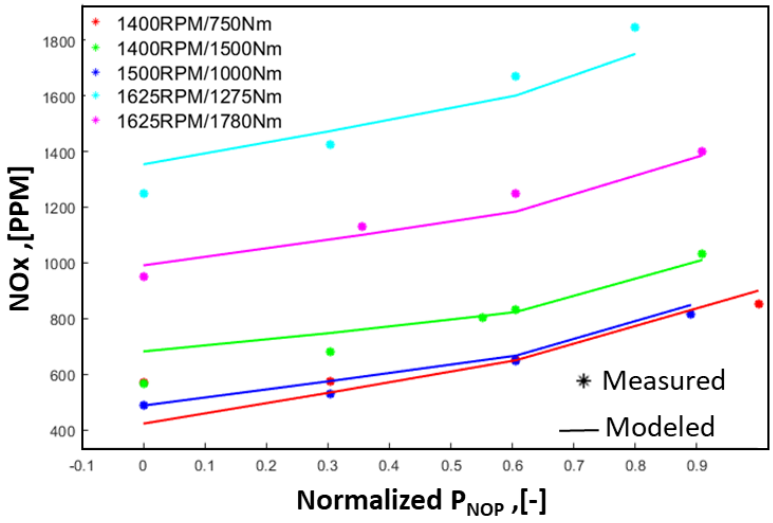

Figure 2-12: Comparison of measured and modeled nitrogen oxides for different needle opening pressure

2.3.4 Calibration factor

The calibration factor f_{sp} in (2.13) is calculated throughout the engine operating range at the setpoint and stored as an offline map, as shown in Figure 2-13. Table 2-2 shows the final value of the parameters identified.

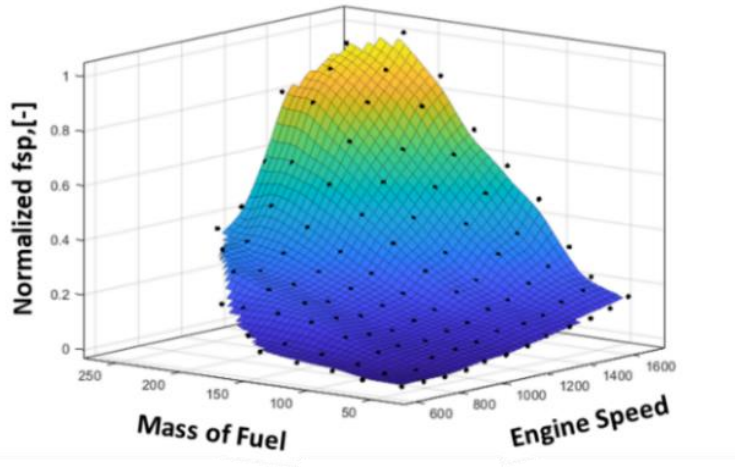

Figure 2-13: Calibration map as a function of engine speed and mass of fuel

Table 2-2: Initial and final value of the model parameters

Symbol	Physical Parameter	Initial value	Final value
$\alpha_{\theta a}$	Activation Temperature	27000	32527
α_{Taf0}	Adiabatic Flame Temperature	10000	10517
α_{Taf1}		$1.5e^{-9}$	$1.48e^{-9}$
α_{Taf2}		-0.5	-0.45
$\alpha_{\gamma 0}$	Isentropic exponent	1.34	1.103
$\alpha_{\gamma 1}$		0	-0.092
α_{kfb}	The ratio of reaction constants	1	23.65
α_{PFRP}	Reaction Zone Volume	0	$4.5e^{-9}$
α_{PNOP0}		0	-0.0519
α_{PNOP1}		0	0.0506
α_{Khl0}	Heat loss at reaction zone boundary parameters	0	0.0103
α_{Khl1}		0	$4.108e^{7}$
α_{Mthr}	Fuel mass threshold	0	$87e^{-5}$

The steps involved in the parameter identification processes are summarized in Figure 2-14. These steps are suggested and summarized for an engine without a wastegate or VGT. For an engine with a separate EGR valve and P_{int} actuator, then use P_{int} sweep for step 6 and EGR sweep for steps 2 and 4.

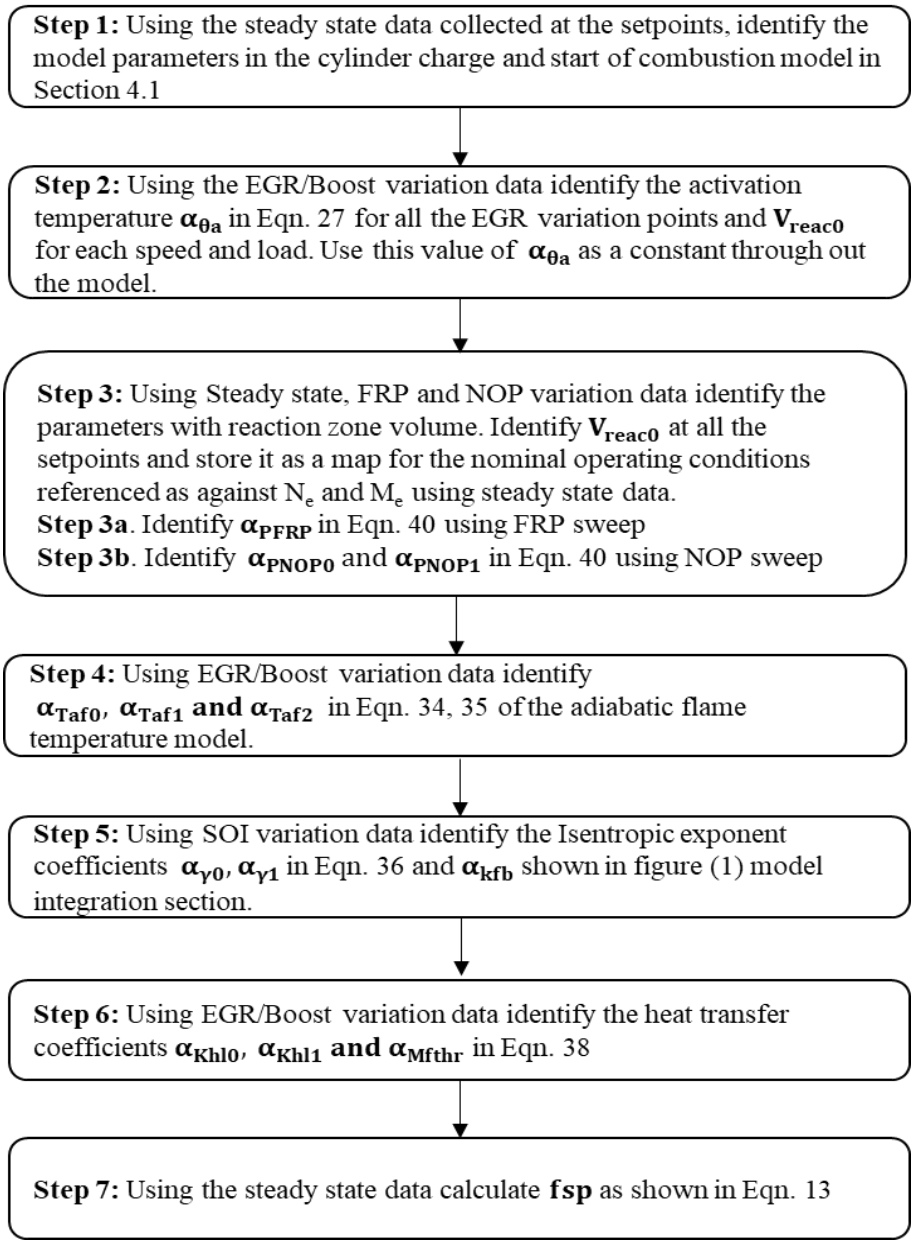

Figure 2-14**:** Summary of steps in model parameter identification

2.4 Results and discussion

The model is validated experimentally at both steady-state and transient operations. Figure 2-15 shows the model's capability to predict steady-state operations. This data set also includes data with a single parameter variation of $SOI/M_{EGR}/P_{int}/P_{FRP}$ individually used during parameter identification. Results show that the maximum error is 6.2 %.

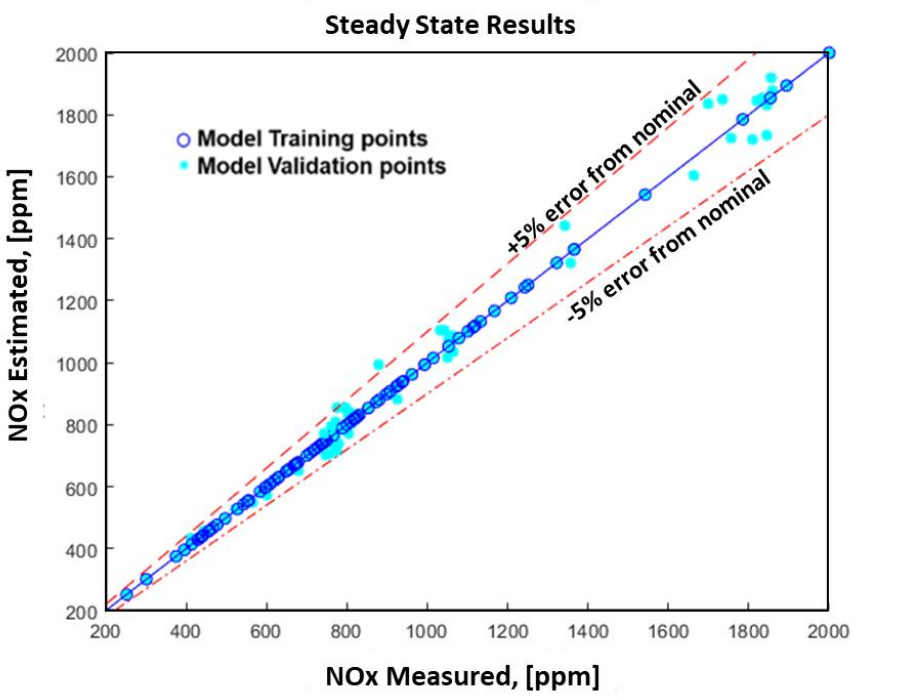

Figure 2-15**:** Comparison of oxides of nitrogen measured with estimated at steady-state operating conditions with a change in nominal operating parameters.

The model predicted NO_X is compared with the two other NO_X measurement devices over a section of the federal test procedure (FTP) cycle in Figure 2-16. It is observable that the NO_X model can capture the transient trends, which is evident from the fast NO_X measurement. Transient NO_X contribution to the total FTP cycle NO_X is significant. Hence capturing these transient NO_X trends during tip-in and tip-out is indispensable. The model prediction on a complete FTP cycle is compared in Figure 2-17. Figure 2-18 shows the transient NO_X prediction with step changes in speed and torque. The NO_X modeled is within ±3 % bound throughout.

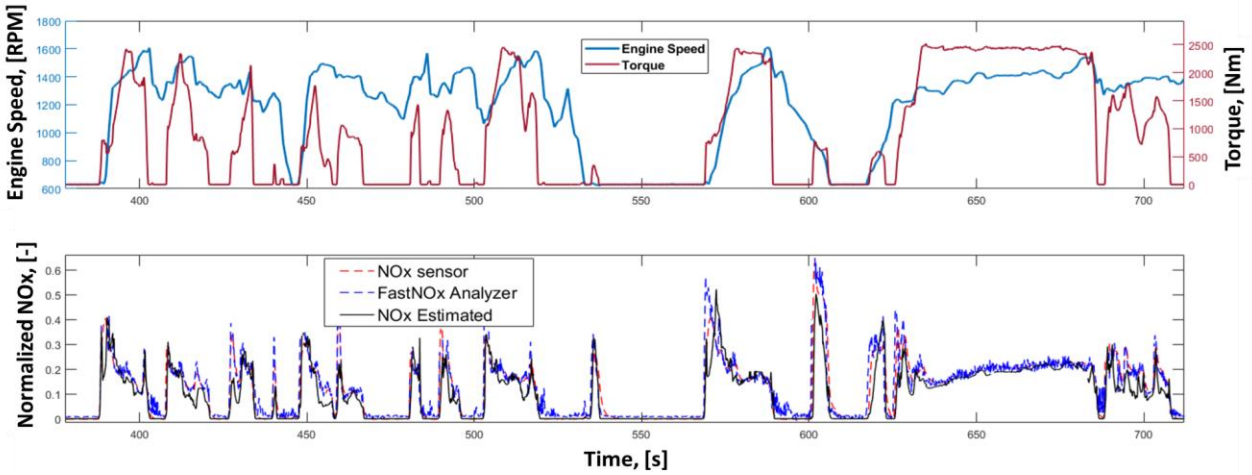

Figure 2-16: Comparison of oxides of nitrogen measured with estimated at transient

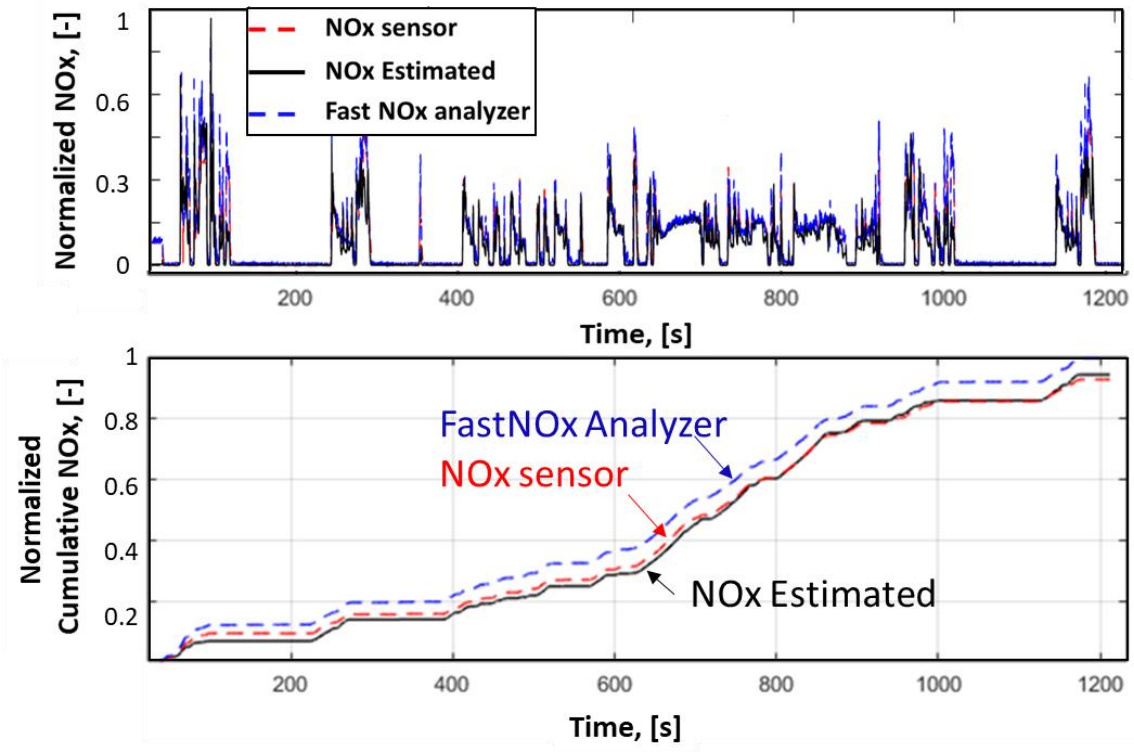

Figure 2-17: Comparison of cumulative oxides of nitrogen over a federal test procedure cycle

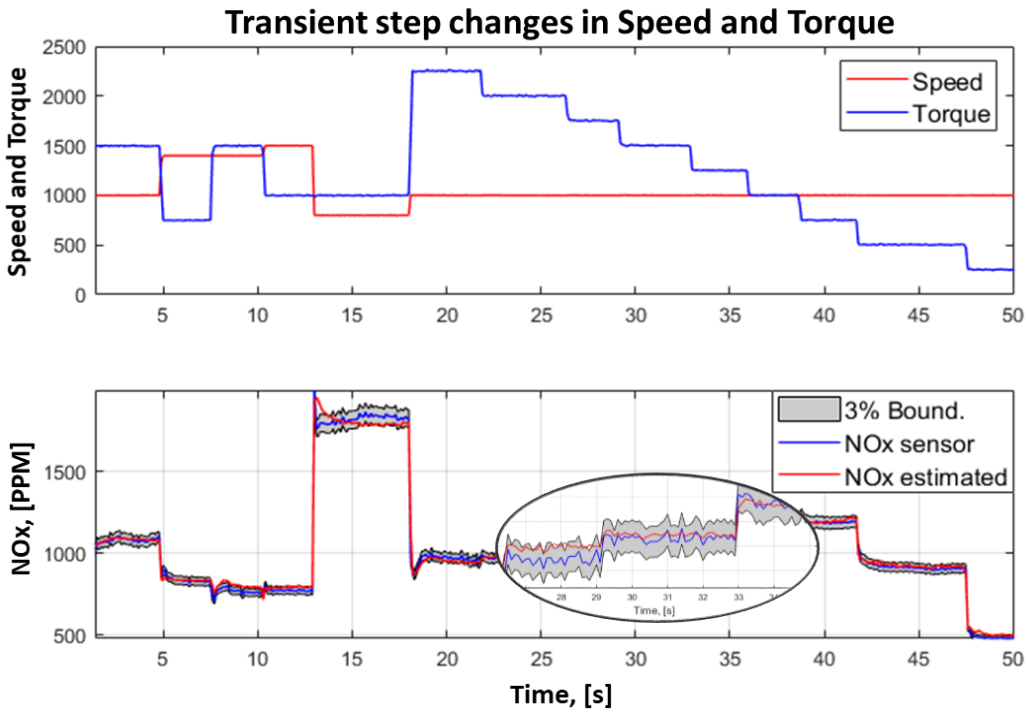

Figure 2-18**:** Comparison of oxides of nitrogen with transient step changes in speed and torque

2.5 Conclusion

A physics-based NO_X model, which can be used in a diesel engine control unit without a need for a cylinder pressure sensor, is developed. The model was structured to predict the impact of major diesel engine control variables, including $SOI, M_{EGR}, P_{int}, P_{FRP}$, and P_{NOP} on the engine-out NO_X emissions. Experimental data validated the model accuracy, and a maximum error of only 6.2 % was observed. The model's transient performance was also evaluated with an engine run over the transient federal test procedure for heavy-duty engines, and an accuracy of 93 % was observed for the accumulative NO_X at the end of the cycle. The proposed NO_X model is recommended for online and predictive engine control applications with the cycle-averaged architecture design.

Chapter 3 Reduced-order Airpath and Aftertreatment Thermal Model

In this chapter, the development of a physics-based full-order air path model is described for a modern air path system in which the EGR valve controls both the EGR flow rate and intake manifold pressure. A step-by-step model order reduction procedure is presented to realize a low-order air path model and enable real-time implementation with the feasibility to use higher execution sampling time. The reduced air path model is then used to calculate the input variables required for a cycle-averaged NO_X model and an aftertreatment thermal model. With the three sub-models, the engine fuel efficiency and emissions are predicted on a rapid prototyping system. A gain scheduled PID controller for closed-loop control of engine torque is developed to manipulate the engine pedal position and ensure tracking of the desired torque even when the control signals such as the EGR valve position deviate from a baseline position. A Smith predictor is used to account for the feedback delay encountered during the real-time simulation to realize the controller. This research work's focuses on modeling the EGR valve shown in Figure 3-2, which controls both the EGR flow rate and flow to the turbine. Besides, the real-time implemented complete engine model that includes airpath, feed-gas NO_X emission, and aftertreatment thermal states can simulate modern diesel engines and predict critical states of fuel economy and emissions.

3.1 Experimental setup, specifications, and test matrix

A class 8 truck heavy-duty 12.8 L diesel engine with a rated power of 375 kW at 1625 RPM and rated torque of 2400 Nm at 1075 RPM and an aftertreatment system are studied in this work. The engine has a twin-scroll fixed geometry turbo with a flapper type EGR valve, which controls both the EGR flow rate and the exhaust flow rate to the turbine small scroll, as shown in Figure 3-2 the EGR valve can take any position from completely closing the EGR loop or completely closing the flow to the turbine small scroll. Therefore, the EGR valve controls both the EGR flow rate and the intake manifold pressure without needing a wastegate. To develop the models,

steady-state data was collected at 102 setpoints, which are evenly spaced over the complete engine operating range, as shown in Figure 3-3. As shown in Table 3-1, sensors with specifications were used to measure temperature, pressure, and NO_X. The fast NO_X analyzer is critical in this work to capture the fast transient NO_X.

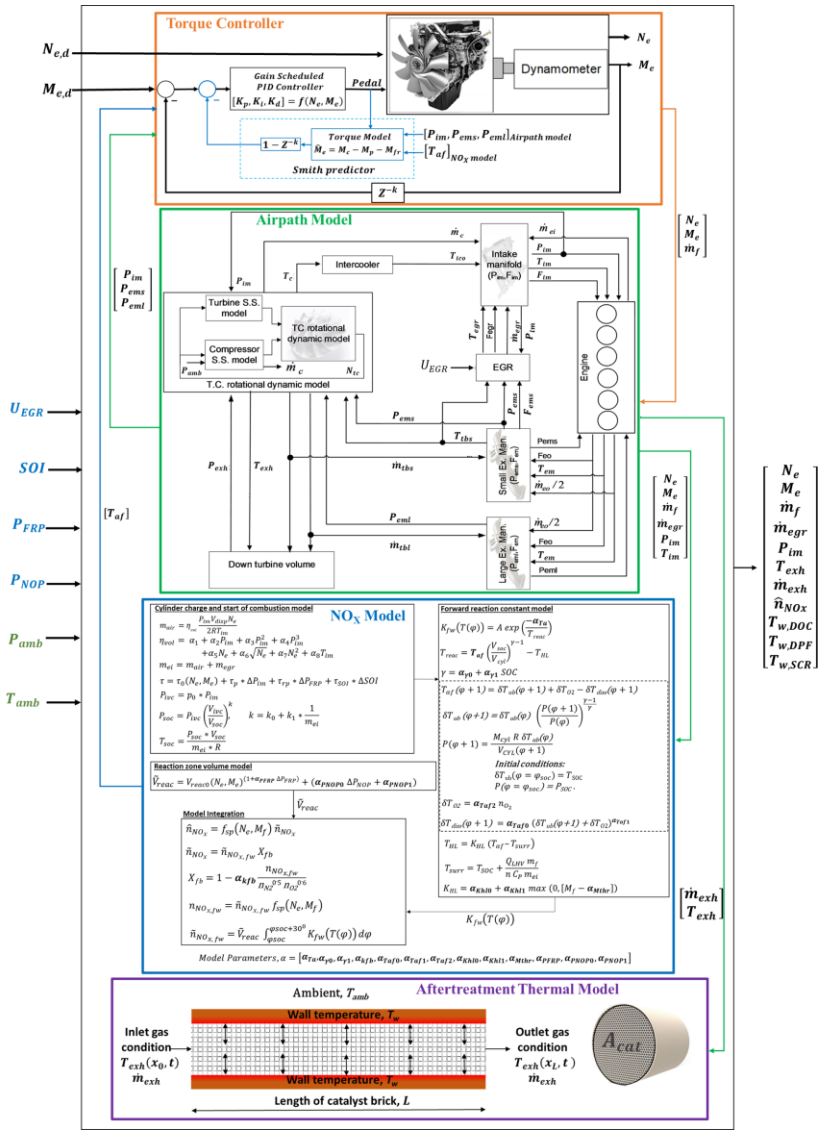

Figure 3-1: Overall structure of the physics-based engine and aftertreatment thermal model showing the interaction between the sub-models and some of the critical model inputs and outputs.

As circled in Figure 3-3, single parameter variation of Start of Injection (*SOI*), Exhaust Gas Recirculation valve position (U_{egr}), Fuel Rail Pressure (P_{FRP}) and Needle Opening Pressure

(P_{NOP}) are conducted at ten different setpoints. The parameter sweep points are selected based on the real-world operating conditions of this engine which is also the most visited operating point over an federal test procedure (FTP) cycle. Five are used to calibrate the model from the total parameter sweep data set at ten different points, and five are used to validate the model. One set of hot FTP transient data is used to calibrate the parameters in the aftertreatment thermal model. The final validation is conducted over an FTP cycle with the complete model on a rapid prototyping controller.

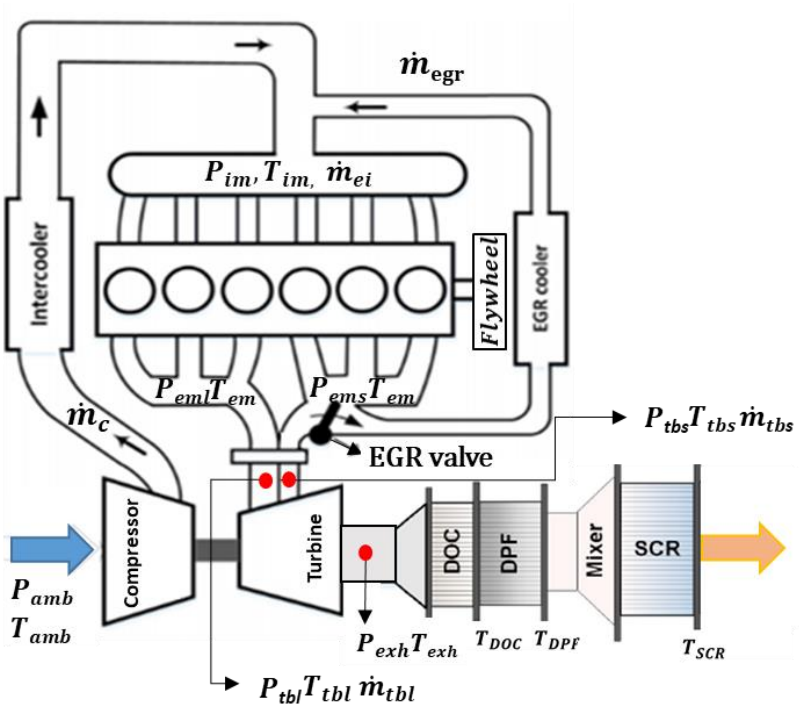

Figure 3-2: Schematic layout of the diesel engine and the aftertreatment system.

Table 3-1: Specification of sensors used for model development in this work.

Temperature sensor	**K type thermocouple, +/- 2 ^{0}C accuracy**
Pressure sensor	**0-15 psi gauge type, ±0.25 % accuracy**
NOx sensor	**0-2000 PPM, ±5 % full-scale accuracy, 1 second response time**
Fast NOx Analyzer	**0-2000 PPM, ±1 % full-scale accuracy, 10 ms response time**

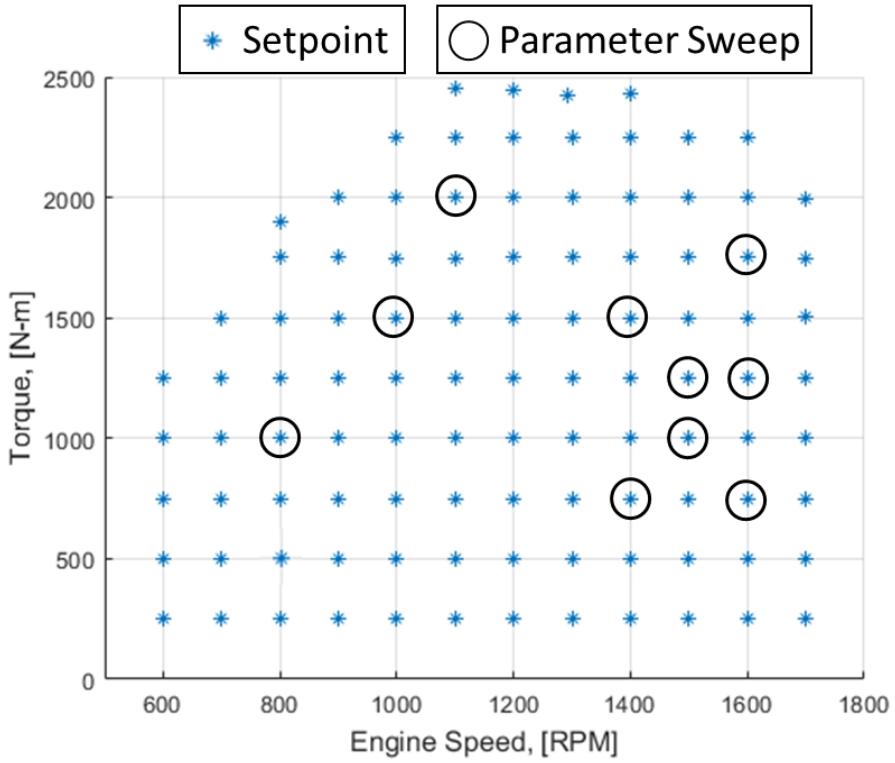

Figure 3-3: Engine operating range showing the setpoints (marked in asterisk) and parameter variation points (encircled).

3.2 Airpath Model

The engine airpath model comprises of sub-models for predicting temperatures, pressures, flows, and the engine's power at both steady-state and transient conditions. The air path model's accuracy lays a solid foundation for the good performance of the rest of the other engine and aftertreatment models. The airpath model is divided into sub-models, as shown in Figure 3-1 to capture individual component's physical properties. The sub-models include the engine flow rate model, the engine torque model, the exhaust manifold temperature model, the EGR flow model, the compressor flow, the compressor efficiency model, and the turbine flow model. Dynamic models include the filling dynamics in the intake, exhaust, and turbine out manifolds, thermal dynamics in exhaust manifolds, upstream turbine, intake burned gas dynamics, and the turbine rotational dynamics. The sub-models are first tuned individually, and they are assembled and fine-tuned as an aggregate model.

The airpath model for this engine's previous generation was presented in [61] and [62]. Specific sub-components of the airpath model are updated to accommodate the hardware changes and improve the prediction of the exhaust gas enthalpy and engine torque, which are critical for estimating the aftertreatment thermal dynamics and fuel economy. The presented exhaust manifold temperature model utilizes an assumption of instantaneous heat release process [63], and the resulting model shows better accuracy in capturing the trend with variation in engine control parameters, including *SOI* and U_{egr}. Moreover, the updated engine torque model can predict the change in torque with the relative change in *SOI* and U_{egr}. The turbine model is also updated compared to the model developed in [62] to predict the variations of turbine inlet pressure caused by the EGR valve [64] shown in Figure 3-2.

3.2.1 Exhaust Manifold Temperature

The exhaust manifold gas temperature is critical as it serves as the boundary condition for the engine and the aftertreatment present downstream. This model is required to capture the effect on exhaust gas temperature with the change in *SOI* and U_{egr}. It is assumed that combustion happens instantly at the start of combustion (*SOC*), which is after a certain ignition delay δSOC after SOI

$$SOC = SOI + \delta SOC \tag{3.1}$$

The cylinder volume, V, is a function of crank angle, so the cylinder volume at intake valve closing (V_{ivc}), the start of combustion (V_{soc}), and exhaust valve opening (V_{evo}) are well-defined. The in-cylinder temperature and pressure before combustion T_{bc} and P_{bc} can thus be expressed as follows,

$$T_{bc} = T_{im}\left(\frac{V_{ivc}}{V_{soc}}\right)^{\gamma_c - 1} \tag{3.2}$$

$$P_{bc} = P_{im}\left(\frac{V_{ivc}}{V_{soc}}\right)^{\gamma_c} \tag{3.3}$$

where γ_c is the polytropic compression coefficient. After combustion, the in-cylinder temperature and pressure become T_{ac} and P_{ac} which can be written as,

$$T_{ac} = T_{bc} + \left(1 - \frac{m_{egr}(1 + AFR_s)}{(m_{ei} + m_f)(1 + \lambda\, AFR_s)}\right)\frac{Q_{LHV}}{c_v(1 + AFR_c)} \tag{3.4}$$

$$P_{ac} = P_{bc}\frac{T_{ac}}{T_{bc}} \tag{3.5}$$

Then the in-cylinder mixture expands towards evo as follows,

$$T_{evo} = T_{ac}\left(\frac{V_{soc}}{V_{evo}}\right)^{\gamma_e - 1} \tag{3.6}$$

$$P_{evo} = P_{ac}\left(\frac{V_{soc}}{V_{evo}}\right)^{\gamma_e} \tag{3.7}$$

where γ_e is the polytropic expansion coefficient. Finally, the exhaust gas leaves the cylinder, and the temperature becomes the following,

$$T_{em} = T_{evo}\left(\frac{P_{ems}}{P_{evo}}\right)^{\frac{\gamma_e - 1}{\gamma_e}} + c_0 + c_1\, m_f \tag{3.8}$$

The model tuning parameters $\delta SOC, c_0$ and c_1 are identified with the nonlinear least-squares method using steady-state SOI variation data. It is also assumed that the gas temperature in the two exhaust manifold banks connected to three cylinders each, as shown in Figure 3-2, have the same temperature i.e T_{em}, T_{ems} and T_{eml} are equal. The validation results of this model are shown later in Figure 3-8.

3.2.2 Turbine Flow

The turbine used in this engine is a fixed geometry twin-scroll turbine without wastegate. The exhaust manifold has two banks, each connected to three cylinders. The exhaust gas flow from the manifold close to the flywheel is split into EGR flow and flow to turbocharger small scroll by the EGR valve, whereas the exhaust gas in the other manifold entirely flows to the turbine large scroll, as shown in Figure 3-2. The turbine flow model is developed by simulating the interaction between the turbine's two scrolls and the EGR valve on the turbine flow. The turbine flow estimation is very critical as it serves as model input to estimate P_{ems} and P_{eml} which will be described later in (3.39) and (3.40).

The theoretical corrected flow rate to turbine small $\dot{m}_{tbs,c}$ and large $\dot{m}_{tbl,c}$ inlets (note: c term in the subscripts denote corrected) are given by,

$$\dot{m}_{tbs,c} = \dot{m}_{tbs}\frac{\sqrt{T_{em}}}{P_{tbs}} \text{ and } \dot{m}_{tbl,c} = \dot{m}_{tbl}\frac{\sqrt{T_{em}}}{P_{tbl}} \tag{3.9}$$

Where $\dot{m}_{tbs}$ and $\dot{m}_{tbl}$ are mass flow rate of exhaust through turbine small and large scroll. T_{em} is the exhaust manifold gas temperature. P_{tbs} and P_{tbl} are exhaust gas pressure in the turbine, small and large scroll.

The corrected turbocharger speed $N_{tc,c}$ is given by,

$$N_{tc,c} = N_{tc}\sqrt{\frac{T_{ref}}{T_{em}}} \tag{3.10}$$

T_{ref} is a reference temperature which is 305 K in this work,

$$\dot{m}_{tbs} = \frac{\dot{m}_{ei} + \dot{m}_f - \dot{m}_{egr}}{2} \text{ , and } \dot{m}_{tbl} = \frac{\dot{m}_{ei} + \dot{m}_f}{2}. \tag{3.11}$$

The mass flow rate of EGR $\dot{m}_{egr}$ is given by,

$$\dot{m}_{egr} = \frac{\left(a_1 U_{egr} + a_2 U_{egr}^2\right) P_{tbs}}{\sqrt{(RT_{em})}}\left(\frac{P_{im}}{P_{tbs}}\right)^{\frac{1}{\gamma}}\sqrt{\frac{2\gamma}{\gamma - 1}\left(1 - \left(\frac{P_{im}}{P_{tbs}}\right)^{1-\frac{1}{\gamma}}\right)}. \tag{3.12}$$

Where a_1 and a_2 are model constants to estimate the effective EGR valve opening area.

The estimated corrected flow rate $\hat{\dot{m}}_{tbl,c}$ and $\hat{\dot{m}}_{tbs,c}$ are given by,

$$\hat{\dot{m}}_{tbl,c} = (d_0 + d_1 r)\sqrt{1 - \Pi_{tl}^{d_2 + d_3 r}} \text{ and, } \hat{\dot{m}}_{tbs,c} = r\,\hat{\dot{m}}_{tbl,c}. \tag{3.13}$$

The asymmetry parameter r depends on pressure ratio Π and corrected turbocharger speed $N_{tc,c}$,

$$r = c_1 + c_2\Pi_{ts} + c_3\Pi_{tl} + c_4 N_{tc,c} + c_5\Pi_{ts}\Pi_{tl} + c_6\Pi_{ts}N_{tc,c} + c_7\Pi_{tl}N_{tc,c} + c_8\Pi_{ts}\Pi_{tl}N_{tc,c} \tag{3.14}$$

where the pressure ratios in the turbine small and large scroll are given by,

$$\Pi_{ts} = \frac{P_{exh}}{P_{tbs}}, and\ \Pi_{tl} = \frac{P_{exh}}{P_{tbl}}. \tag{3.15}$$

where $d_0 - d_3$ and $c_1 - c_8$ are tuning parameters and P_{exh} is the pressure of exhaust gas downstream turbine. Steady-state EGR sweep data with measured turbine inlet and outlet pressure ($P_{tbs},\ P_{tbl}\ and\ P_{exh}$) are used to calculate the theoretical corrected flow rate $\dot{m}_{tbs,c}$ and $\dot{m}_{tbl,c}$ calculated in (3.9) and using the nonlinear least-squares method, the tuning parameters (3.14) are identified. The effect of EGR is not much pronounced below 40 % EGR command, so correction factors $CF_{tbs}(U_{egr}, N_{tc})$ and $CF_{tbl}(U_{egr}, N_{tc})$ are used for those operating points where U_{egr} is less than 40 % to correct the estimated corrected flow, and at other operating points, the value of the correction factor is unity.

$$\dot{m}_{tbs} = CF_{tbs}(U_{egr}, N_{tc})\hat{\dot{m}}_{tbs,c} \tag{3.16}$$

$$\dot{m}_{tbl} = CF_{tbl}(U_{egr}, N_{tc})\hat{\dot{m}}_{tbl,c} \tag{3.17}$$

As shown in Figure 3-4, the error calculated between modeled $\dot{m}_{tbs}$ and $\dot{m}_{tbl}$ from above and theoretically corrected values from (3.9) for the validation measured data set The tuned turbine model shows good agreement with the data, with an average relative error of 7 %.

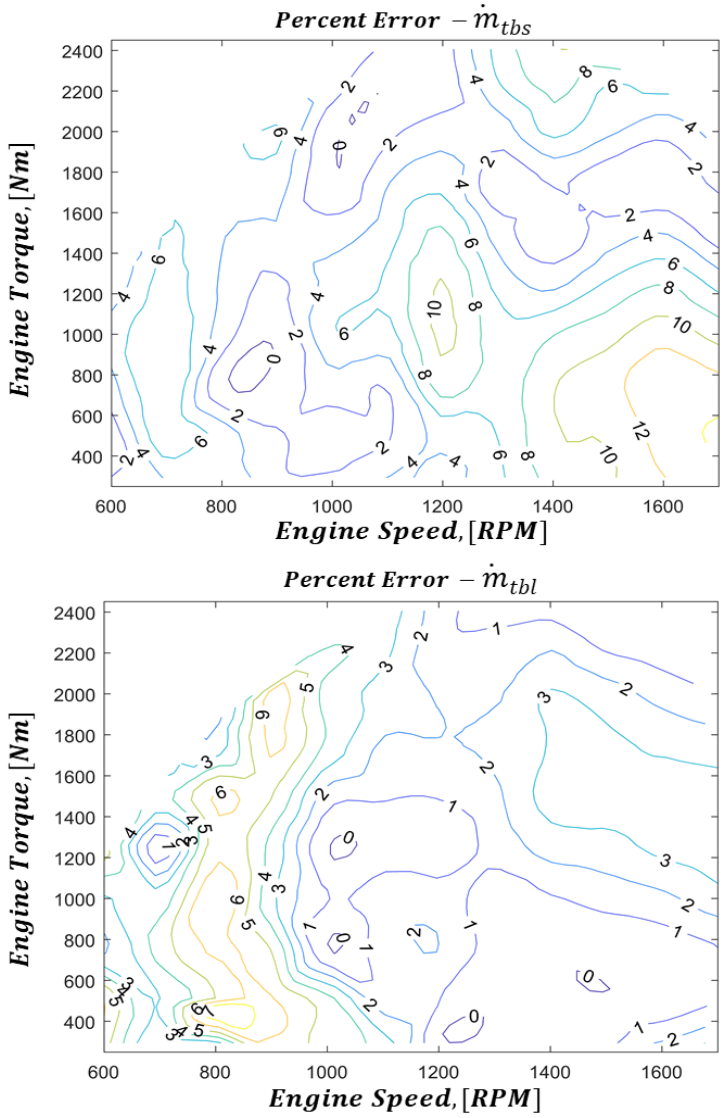

Figure 3-4: Relative error map for modeled turbine flow for the entire engine operating range calculated with steady state data.

3.2.3 Engine Torque

The engine torque model is developed to capture the torque change with respect to SOI and EGR variation and change in engine speed and fuel injection. The estimated brake torque $\widehat{M}_e$ is modeled as follows,

$$\widehat{M}_e = M_c - M_p - M_{fr}. \tag{3.18}$$

The engine brake torque estimated $\widehat{M}_e$ depends on the torque generated due to the combustion of fuel M_c (conventionally called as gross indicated torque), pumping loss M_p and friction loss M_{fr}. Please refer to section 13.2 in [2] for fundamentals in deriving the brake torque model shown in (3.). Since the SOI and U_{egr} affect the combustion parameters such as the polytropic expansion coefficient and charge dilution, correction factors CF_{SOI} and CF_{egr} are included with combustion torque, as shown in (3.). CF_{SOI} captures the effect on brake torque with the change in fuel injection timing SOI and CF_{EGR} captures the effect on brake torque with a change in charge dilution.

$$\widehat{M}_e = CF_{SOI,egr} M_c - M_p - M_{fr}. \tag{3.19}$$

$CF_{SOI,egr}$ is the ratio of the correction factors in (3.2). The correction factor CF_{SOI} shown in (3.2) is a linear function that depends on the relative difference between the nominal SOI (SOI_0) and actual SOI showed in (3.2). Nominal fuel injection timing SOI_0 is the steady-state SOI crank angle for particular engine speed and mass of fuel injected per engine stroke m_f which is stored as an offline map.

$$CF_{SOI,egr} = \frac{CF_{SOI}}{CF_{egr}}, \tag{3.20}$$

$$CF_{SOI} = 1 + \alpha_1 \delta_{SOI} + \alpha_2 \delta_{SOI}^2, \tag{3.21}$$

$$\delta_{SOI} = SOI_0(N_e, m_f) - SOI. \tag{3.22}$$

The correction factor CF_{egr} is modeled as a function of speed, torque, adiabatic flame temperature and δ_{egr}, which is the relative difference between the nominal EGR valve position u_{egr0} and actual EGR valve position u_{egr} shown in (3.2). The EGR ratio is defined as the ratio between the mass of EGR in the engine intake air mass to the sum total mass of intake air and mass of EGR. With the increase in EGR dilution, the adiabatic flame temperature T_{af} decreases, as shown in Figure 3-5 for various engine operating conditions, and correspondingly there is a drop in-cylinder pressure, and temperature which results in reduced torque, and this effect is captured by the inclusion of the term T_{af} in (3.24). The T_{af} model is explained in (3.25), and it is calculated in the NOx emission model explained later in the paper. For the complete structure of adiabatic flame, temperature refers to [20]. The adiabatic flame temperature depends on the temperature increase due to compression of unburned charge (δT_{ub}), temperature increase due to

the combustion of fuel (δT_{O_2}) and loss in combustion gas temperature due to gas dissociation (δT_{diss}).

$$\delta_{egr} = u_{egr0}(N_e, m_f) - U_{egr}, \tag{3.23}$$

$$CF_{egr} = 1 + \theta_1 \delta_{egr} N_e + \theta_2 \delta_{egr} m_f + \theta_3 \delta_{egr} T_{af}. \tag{3.24}$$

The adiabatic flame temperature T_{af} is given by,

$$T_{af} = \delta T_{ub} + \delta T_{O_2} - \delta T_{diss}. \tag{3.25}$$

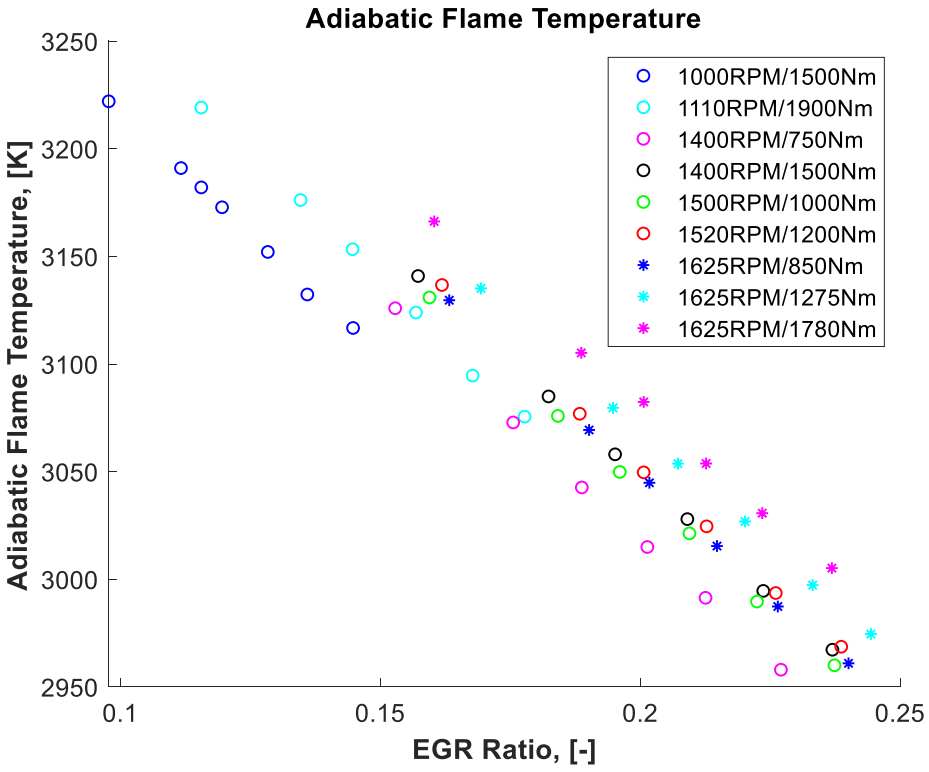

Figure 3-5: Impact of the exhaust gas dilution on adiabatic flame temperature for various engine speed and torque.

The resulting engine torque model predicts an average relative error of 2.7 % and captures the trend caused by changing SOI and EGR, shown in Figure 3-6.

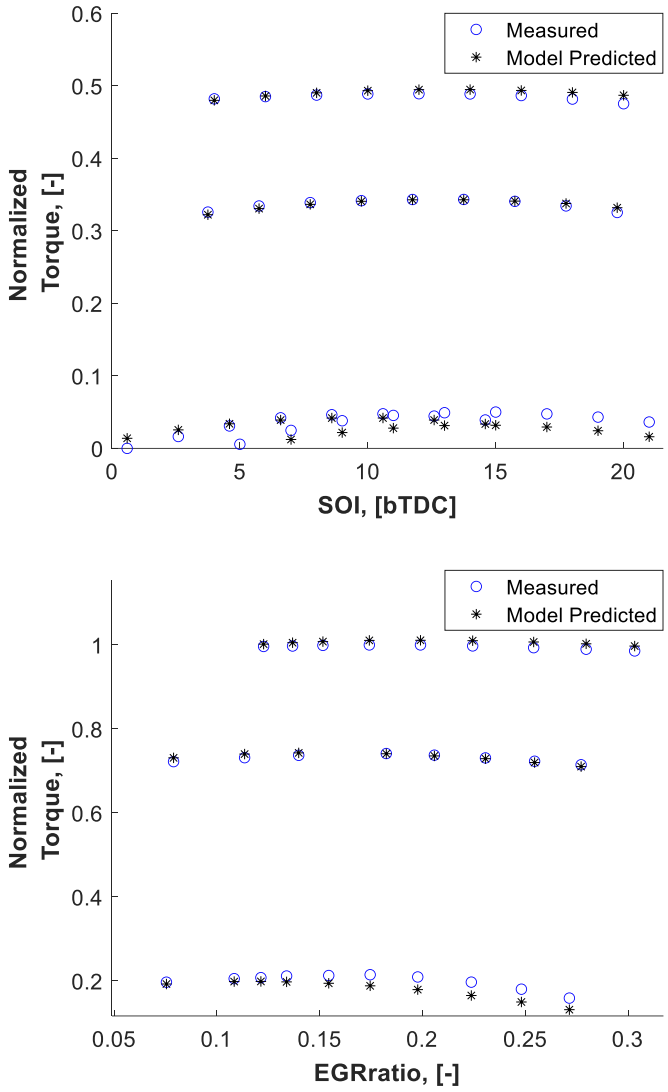

Figure 3-6: Comparison of model-predicted torque and measured for variation in start of injection (top plot) and exhaust gas recirculation ratio (lower plot).

3.3 Airpath model order reduction

The full order airpath model consists of nine states,

$$X = \left[P_{im}, P_{ems}, P_{eml}, N_{tc}, T_{tb}, P_{exh}, F_{im}, F_{ems}, T_{Exh,m}\right]. \tag{3.26}$$

To convert the full order model into a fast running and real-time implementable model, a discrete model with a sample time of at least 10 ms was targeted in this paper to reduce the computational burden without sacrificing the advantages of the full order model to efficiently capture the transient dynamics of EGR, intake pressure, exhaust temperature, and torque. The sample time

determines the model accuracy and stability. The larger the sample time, the higher the state difference between consecutive steps, and the states may not converge, resulting in an unstable model or poor prediction. Reducing the number of states increases the probability of using a higher sampling time because of the reduction in states' convergence time. However, removing key states would reduce the model performance. The original 9-state model shown in (3.26) is reduced by replacing the exhaust pressure (P_{exh}), burned gas fractions ($F_{im}\ and\ F_{ems}$) and exhaust manifold thermal dynamics ($T_{Exh,m}$) models with static models.

The exhaust pressure downstream turbine P_{exh} depends on the enthalpy of the turbine outgas, and it is mainly dependent on the mass flow through the turbine and the temperature of exhaust gas T_{exh}. The start of injection (SOI) affects the turbine upstream gas temperature. For example, retarded injection after the top dead center increases the exhaust gas temperature. EGR valve position determines the mass of exhaust gas diverted between EGR and turbine. A static model is developed as a function of engine speed N_e, the mass of fuel m_f, SOI and U_{egr} as shown in (3.28). The term δ_{SOI} and δ_{EGR} are previously defined in (3.2) and (3.23). The mass of exhaust gas in the turbine downstream is defines as m_{exh}.

The exhaust pressure P_{exh} in the full order model is as follows,

$$\dot{P}_{exh} = \frac{RT_{exh}}{V_{exh}}(m_{tbs} + m_{tbl} - m_{exh}). \tag{3.27}$$

The P_{exh} in reduced-order model is given by,

$$P_{exh} = P_{t0}\left(N_e, m_f\right) + \alpha_1\delta_{SOI} + \alpha_2\delta_{egr}. \tag{3.28}$$

The model parameters are $\alpha_1$and α_2, which are identified using steady-state variation data of SOI and U_{egr} respectively. The nominal exhaust pressure P_{t0} is calculated and stored as an offline map and referenced against speed and mass of fuel. In [51] for a fixed geometry turbine, a map of pressure ratio is generated for various mass flow rates and density of exhaust gas. However, to avoid a vast data collection process, to generate the pressure ratio map using a turbocharger flow bench is used in this work.

The burned gas fraction in the full order model is as follows,

$$\dot{F}_{im} = \frac{RT_{im}}{P_{im}V_{im}}\left[(F_{ems} - F_{im})\, m_{egr} - F_{im}\, m_c\right], \tag{3.29}$$

$$\dot{F}_{ems} = \frac{RT_{ems}}{P_{ems}V_{ems}}\left[(F_{eo} - F_{ems})m_{tbs}\right], \tag{3.30}$$

$$F_{eo} = \frac{(1 + AFR_S)m_f + F_{im}m_{ei}}{m_f + m_{ei}}. \tag{3.31}$$

The model is reduced further by considering the fast dynamics of burned gas fraction,

$$F_{im} = F_{ems}\left(\frac{m_{egr}}{m_{egr} + m_c}\right), \tag{3.32}$$

$$F_{ems} = F_{eo}. \tag{3.33}$$

The exhaust manifold thermal dynamics $T_{Exh,m}$ in the full-order model is as follows,

$$\dot{T}_{Exh,m} = m_{eo}C_{p,exh}(Q_1 - Q_2), \tag{3.34}$$

$$Q_1 = h_1A_1(T_{em} - T_w), \tag{3.35}$$

$$Q_2 = h_2A_2(T_w - T_{amb}). \tag{3.36}$$

where Q_1 is heat transfer from the exhaust gas to the manifold interior wall, and Q_2 is from exterior wall to ambient air with convective heat transfer coefficients $h_1$and h_2 respectively. The surface area of the manifold interior and outer wall are A_1 and A_2 which are model parameters. T_{amb} refers to the gas temperature surrounding the exhaust manifold, in the current experimental setup at engine dynamometer, T_{amb} refers to the test cell temperature; however, in the vehicle level T_{amb} would refer to under the hood temperature. The thermodynamic state $T_{Exh,\,m}$ which will account for the heat lost in the exhaust manifold from the exhaust gas to the manifold wall has slow dynamics, and it is approximated as the temperature of the gas upstream turbo as shown below in (3.37). Note that $T_{tb} = T_{tbl} = T_{tbs}$.

$$T_{Exh,\,m} = T_{tb}. \tag{3.37}$$

The reduced-order model has five states as shown below,

$$X = [P_{im}, P_{ems}, P_{eml}, N_{tc}, T_{tb}], \tag{3.38}$$

$$\dot{P}_{im} = \frac{R\,T_{im}}{V_{im}}\left(m_c + m_{egr} - m_{ei}\right) \tag{3.39}$$

$$\dot{P}_{ems} = \frac{R\,T_{em}}{V_{ems}}\left(\frac{m_{eo}}{2} - m_{egr} - m_{tbs}\right) \tag{3.40}$$

$$\dot{P}_{eml} = \frac{R\,T_{em}}{V_{eml}}\left(\frac{m_{eo}}{2} - m_{tbl}\right) \tag{3.41}$$

$$\dot{N}_{tc} = \frac{1}{J}\left(M_{turbo} - M_{comp}\right) \tag{3.42}$$

$$\dot{T}_{tb} = m_{eo}\,C_p\left(h_3A_3(T_{em} - T_{tb}) - h_4A_4(T_{tb} - T_{exh})\right) \tag{3.43}$$

To reduce the model further T_{tb} was approximated as T_{em} with the assumption that the temperature drop between the exhaust port to the turbine inlet is negligible. However, removing the exhaust thermal loss state introduces a significant error in intake pressure estimation and EGR estimation, as shown in Figure 3-7. Hence, it is concluded here that the model cannot be reduced to less than five states.

The reduced-order 5-state model is validated with experimental data, as shown in Figure 3-7. The four critical airpath outputs selected for comparison are EGR mass flow rate, intake manifold pressure, turbocharger speed, and torque. The fuel injection quantity is not directly affected by the model order reduction because it is controlled independently by the torque controller see section 3.7 for details. However, the torque prediction varies between different model orders; this would change the fuel injection quantity when the torque controller attempts to reduce the tracking error between predicted and the desired torque. The nine state is the full-order model, eight state is without $T_{Exh,\,m}$, six state is without $T_{Exh,\,m}$, F_{im} and F_{ems}, five state is without $T_{Exh,\,m}$, F_{im}, F_{ems} and P_{exh}, and four state is without $T_{Exh,\,m}$, F_{im}, F_{ems}, P_{exh} and T_{tb}. Table 3-2 compares the root mean square error (RMSE) calculated between model-predicted and measured values over an FTP for different model orders. Figure 3-7 shows that the prediction accuracy was not significantly affected by model order reduction up to 5-state. With the reduced-order airpath model, the fundamental sampling time or time step was 10 ms compared to the sampling time of 0.1 ms required for the full-order 9-state model.

Table 3-2: Comparison of RMSE and time step between full order and reduced-order model.

	Root Mean Square Error calculated between estimation and measurement over a HOT FTP cycle				
Number of State	$P_{im}, [bar]$	$EGR, [g/str]$	$Torque, [Nm]$	$NO_X, [PPM]$	$Time\ step, [ms]$
9 state	0.070	0.086	83	130	0.1
8 state	0.099	0.164	132	131	1
6 state	0.165	0.173	144	135	1
5 state	0.159	0.092	77	137	10
4 state	0.253	0.197	98	179	10

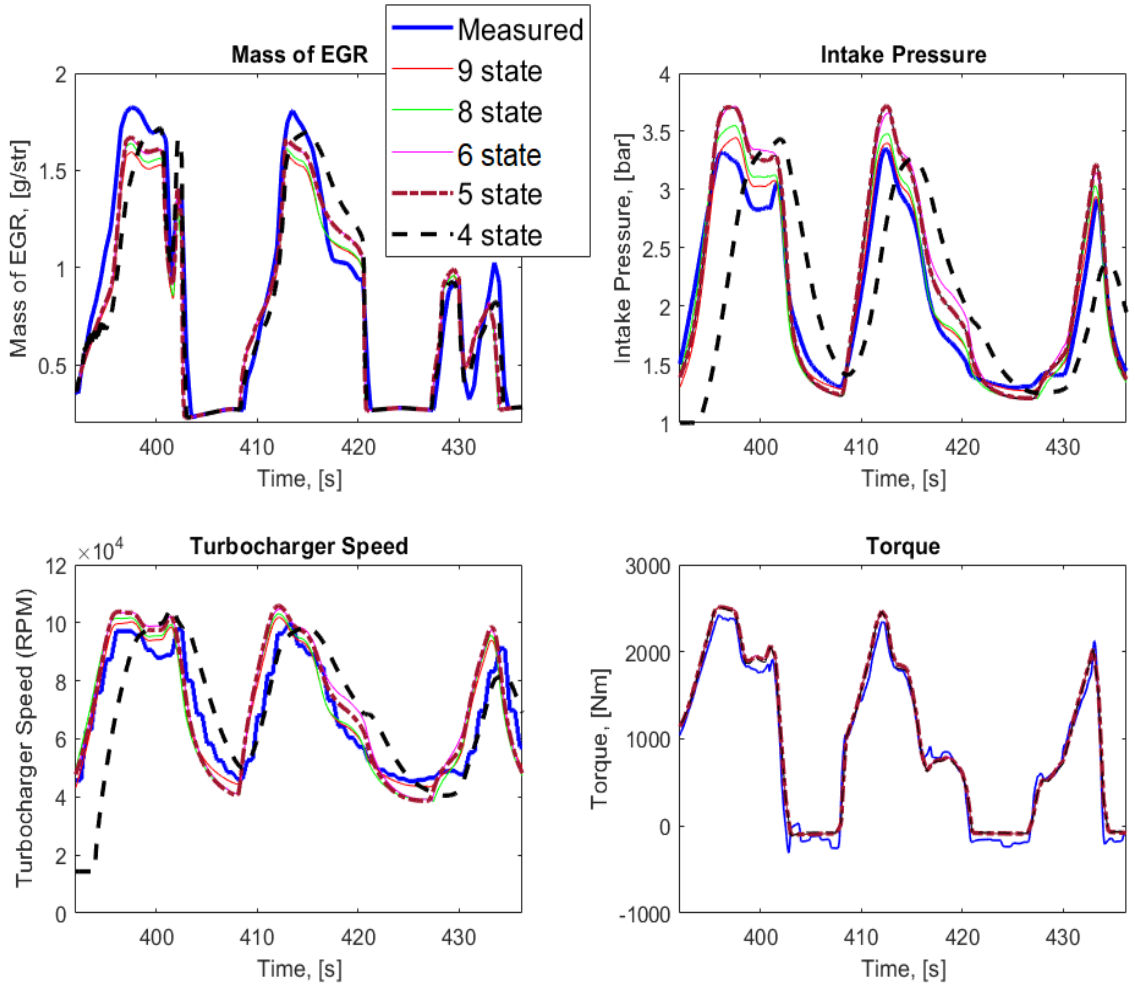

Figure 3-7: Comparison of model prediction by different airpath model order over a federal test procedure cycle.

One of the main objectives of this airpath model is to predict the change in airpath states with the change in SOI and U_{egr}. As shown in Figure 3-8, the model was validated with the experimentally collected steady-state variation of SOI and U_{egr} The experiment was conducted at speed-torque control mode, so the speed and torque are constant. In Figure 3-8, with a change in SOI from the nominal point, the exhaust gas enthalpy changes, affecting the turbocharger speed, and the air path model can capture that effect. The change in the turbocharger dynamics affects intake manifold pressure and EGR mass estimation, and that can be observed from the plot. It should be noted that during SOI sweep, all other engine control parameters like U_{egr}, P_{FRP} and P_{NOP} were maintained at nominal values.

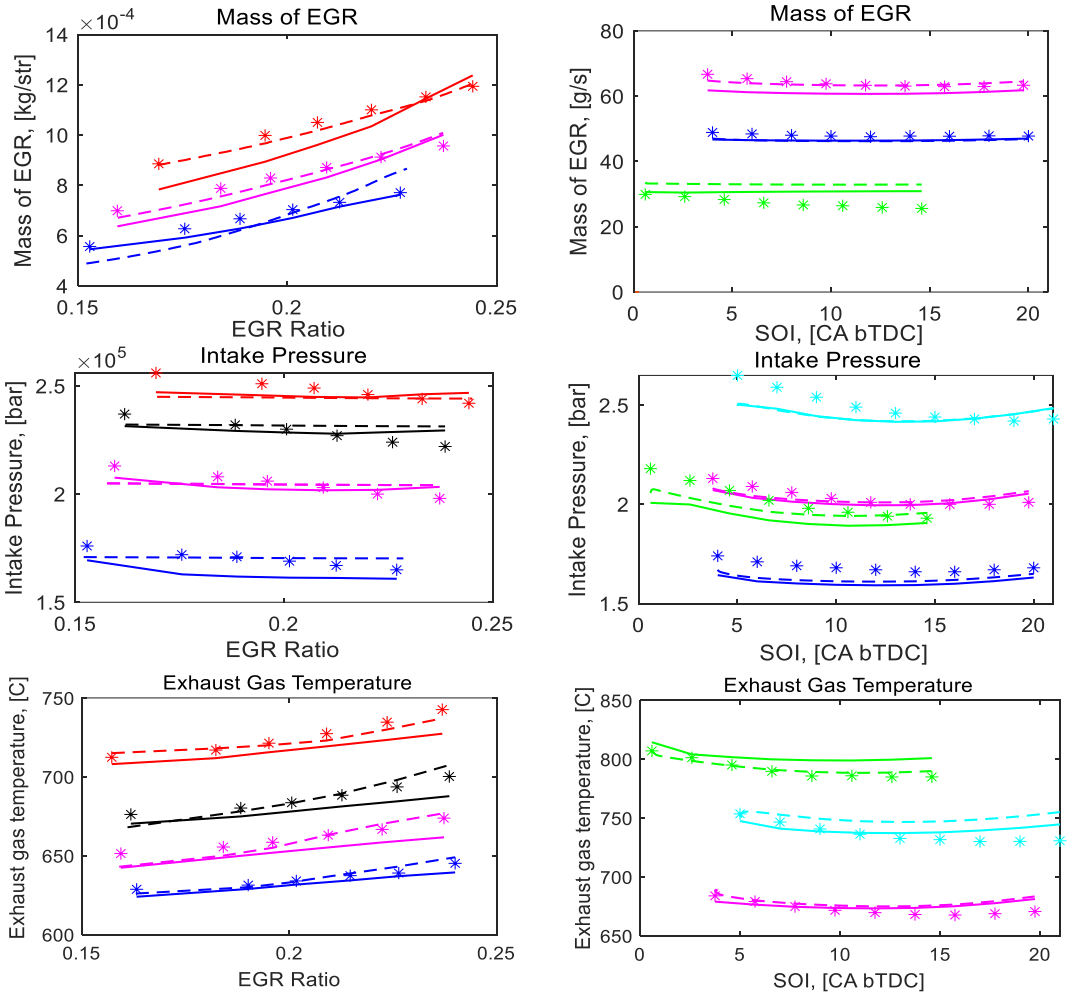

Figure 3-8: Plot showing the comparison of 9 state airpath model (broken lines), five state airpath model (solid lines), and measured value (asterisk) for variation in exhaust gas recirculation valve position and start of injection at different speeds and load conditions.

3.4 Feed gas NOX Emission Model

A physics-based NO_X model developed in the previous work [20] for this engine with an overall structure, as shown in Figure 3-9, is integrated along with the reduced-order airpath model. In [20], the critical inputs to the NO_X model P_{im}, T_{im} and m_{egr} are from measurements, in this paper the performance of the reduced-order airpath model is evaluated by feeding these inputs from the reduced-order model. A brief outlook about the NO_X model is provided in the below section to provide a complete model experience to the reader. A global NO_X formation equation assumes that the total NO_X formed is composed of 80 % NO, and 20 % NO_2 is considered.

$$\frac{1}{2}N_2 + \frac{x}{2}O_2 \rightleftarrows (2-x)NO + (x-1)NO_2 \equiv NO_X \tag{3.44}$$

The theoretical NO_X formed in the formation interval from SOC to 30 degree after SOC is given by,

$$NO_X = \int_{SOC}^{SOC+30} V_{reac}(\varphi)\ [r_{fw}(\varphi) - r_{bw}(\varphi)]\, d\varphi. \tag{3.45}$$

To obtain cycle averaged NO_X formation estimation and to avoid crank angle resolved NO_X, the approximated theoretical NO_X ($\tilde{n}_{NO_x}$) is given by,

$$\tilde{n}_{NO_x} = X_{fb}\,\tilde{V}_{reac} \int_{SOC}^{SOC+30} K_{fw}\big(T(\varphi)\big)\, d\varphi\,. \tag{3.46}$$

Finally, the approximated NO_X is compensated by a calibration factor based on the steady-state map and the final estimated NOx ($\hat{n}_{NOx}$) is given by,

$$\hat{n}_{NOx} = f_{sp}(N_e, m_f)\,\tilde{n}_{NO_x} \tag{3.47}$$

The model inputs such as intake manifold pressure P_{im}, intake manifold temperature T_{im} and Mass of EGR M_{egr} are obtained from the air path model derived in the previous section. Control variables SOI, U_{egr}, P_{FRP} and P_{NOP} are obtained from the actual ECU values. The mass flow rate of fuel injected $\dot{m}_f$ is obtained from the torque controller explained later in the paper.

The integrated airpath and NOx model is tested over the federal test procedure (FTP) cycle. The comparison is made between the full-order nine-state model, reduced-order five state airpath model, and the NOx model performance with measured airpath inputs, as shown in Figure 3-10. A fast NOx analyzer is used to capture the transient NOx more accurately. It can be observed that the feed-gas NOx estimation with the 5-state model, 9-state model, and measured inputs are very close, and the reduced order airpath model can predict the transient dynamics, which are crucial for controlling transient NO_X emission.

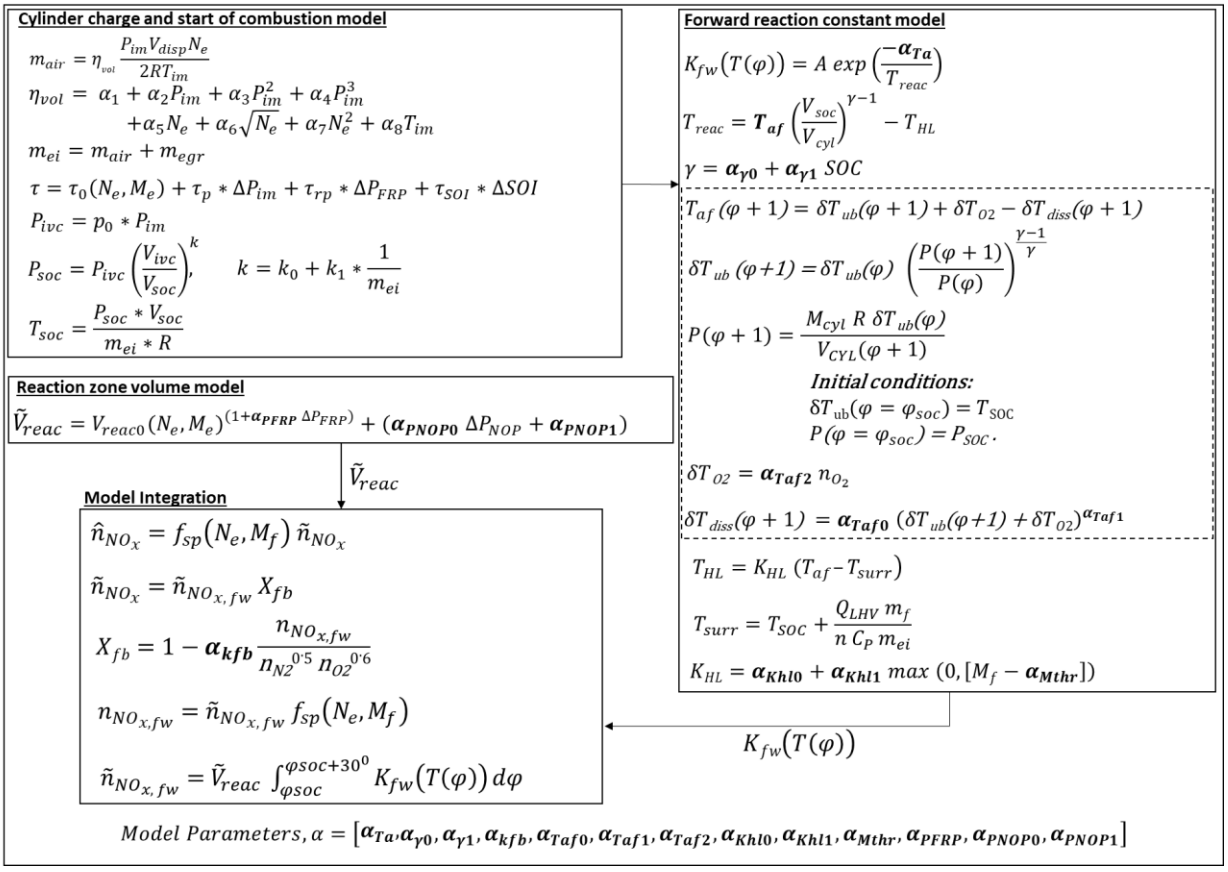

Figure 3-9: Overall structure of the physics-based oxides of nitrogen model.

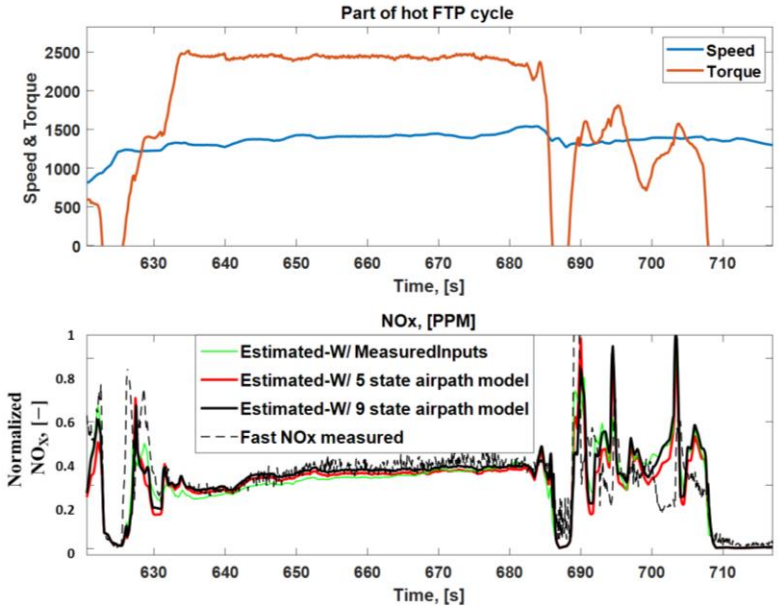

Figure 3-10: Comparison between the oxides of nitrogen estimated with the 9 state airpath model, 5 state airpath model, and with measured inputs against measurement with the fast oxides of nitrogen analyzer.

3.5 Aftertreatment Thermal Model

The advanced aftertreatment system for this heavy-duty engine consists of a DOC, DPF, and SCR in this order downstream of the turbine. The thermal model assumes a lumped thermal mass for DOC, DPF, and SCR [45]. However, the model parameters are identified individually, corresponding to their respective boundary conditions. As shown in Figure 3-11, the inputs to the model are the mass flow rate of exhaust gas $\dot{m}_{exh}$ and the turbine out gas temperature T_{exh} which are estimated from the reduced-order airpath model.

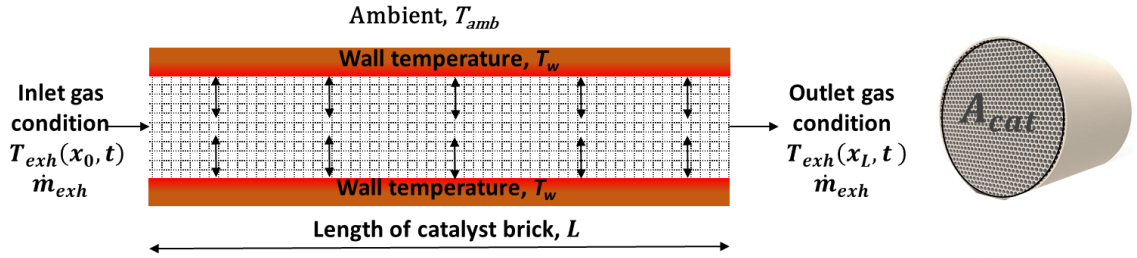

Figure 3-11: Schematic of the main variables in a single catalyst brick.

The heat conduction from the gas to the catalyst brick and exothermic reactions inside the catalyst are ignored. The model calculates the temperature gradient along the catalyst length L and the gas temperature $T_{exh}(x_L, t_k)$ at the exit of the catalyst block x_L at time t_k is given by,

$$T_{exh}(x_L, t_k) = \frac{hA_{cat} * L\big(T_w(x_L, t_k) - T_{exh}(x_0, t_k)\big)}{\dot{m}_{exh}(t_k) \times C_{p,g}} + T_{exh}(x_0, t_k). \tag{3.48}$$

The catalyst wall temperature T_w along the length is given by,

$$T_w(x_L, t_{k+1}) = \frac{hA_{cat}\big(T_{exh}(x_0, t_k) - T_w(x_L, t_k)\big) - hA_{amb}(T_w(x_L, t_k) - T_{amb})}{M_{cat}C_{p,cat}} \times \Delta t + T_w(x_L, t_k) \tag{3.49}$$

The convective heat transfer coefficient h and the surface area of the catalyst exposed to ambient A_{amb} are lumped together as a single parameter hA_{amb} and it is correlated with the exhaust flow rate as shown below,

$$hA_{amb} = \alpha_1 (W_{eo})^{\alpha_2} \tag{3.50}$$

$$Model\ parameters = \big[hA_{cat}, M_{cat}C_{p,cat}, L, \alpha_1, \alpha_2\big]. \tag{3.51}$$

The specific heat of the gas at constant pressure was assumed as a constant, which is 1050 J/kg/K, T_{amb} corresponds to ambient temperature, and Δt is discretization time (10 ms). The five model parameters stated in (3.51) are identified using hot FTP data with the measured gas temperature at both catalyst inlet and outlet locations for DOC, DPF, and SCR. The change in thermal properties of the DPF due to soot loading can be captured by adding additional terms in (3.4), which would depend on the pressure difference across the DPF.

3.6 Implementation and Validation

To enable the model validation and ensure load following while the airpath actuators are optimized for BSFC and $BSNO_X$ in later sections, a torque controller is developed and implemented. The reduced airpath model integrated with the NO_X emissions and aftertreatment thermal models are implemented in a rapid prototyping controller. A gain-scheduled PID controller is designed in order to track the desired torque $M_{e,d}$, with the pedal as a controller output variable and measured torque M_e as feedback variable shown in Figure 3-12.

$$\dot{M}_f(t) = K_p(N_e, M_e)\, e(t) + K_i(N_e, M_e) \int e(t)\, dt + K_d(N_e, M_e)\, \dot{e}(t) \tag{3.52}$$

The gains for proportional K_p, integral K_i and derivative K_d depends on the engine speed and measured torque. The error $e = M_{e,d} - M_e$ is the difference between demand and measured torque. The controller is designed by using plant models obtained at different engine speeds and torques. The plant model is a single-input single-output (SISO) model with fuel quantity as input and engine brake torque as output. Experimental data collected at 10 different operating point marked in circles in Figure 3-3 is used for system identification. The controller gains are tuned to achieve a response time of 0.2 s for a step-change in demand torque (i.e., $\Delta M_{e,d}$ = 150 Nm) and a minimum gain cross over frequency of 5 rad/s for the entire engine operating range. The plant model transfer function for the dominant pole is shown below in (3.53) and the corresponding controller transfer function is shown below in (3.54).

$$P(s) = \frac{76.28}{s + 2.39} \tag{3.53}$$

$$C(s) = \frac{0.0184s + 0.14}{s} \tag{3.54}$$

To account for the feedback delay encountered during real-time communication, a Smith predictor was designed. The modified controller transfer function $\bar{C}$ which accounts for the delay of k steps is,

$$\bar{C} = \frac{C}{1 + C\, \widehat{M}_e(1 - Z^{-k})} \tag{3.55}$$

where C is the gain scheduled PID controller and the modeled torque $\widehat{M}_e$ is from (3.18). The delay $k = 100$ steps were experimentally determined by measuring the time it takes to send an actuator signal from dSPACE to engine and receive it back. However, it can randomly change depending on the communication network performance, the constant delay of 100 steps is verified by repeating the test multiple times. Figure 3-12 shows the overall structure of the controller with a predictor and the various I/O feedback signals.

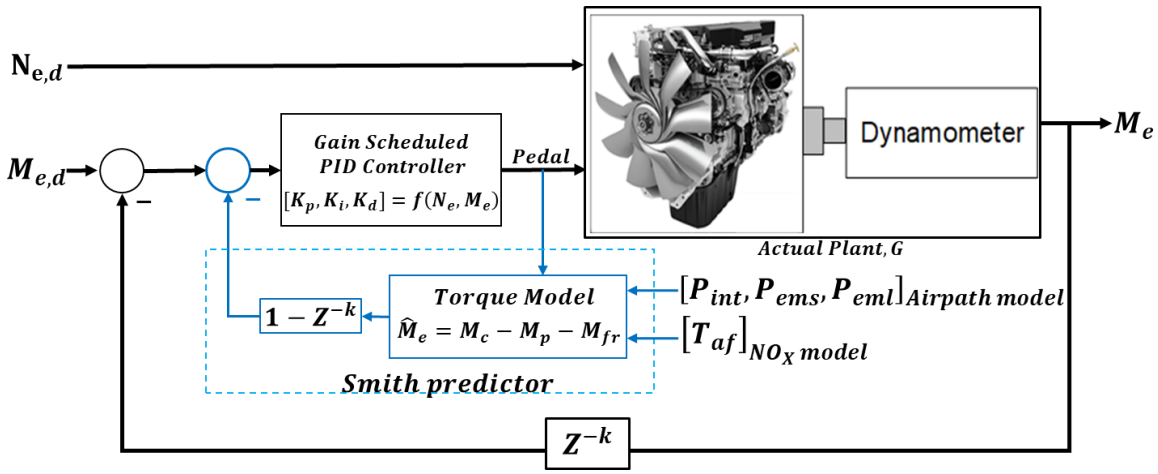

Figure 3-12: Integration of the gain scheduled proportional integral derivative controller with the Smith predictor into the testing system.

The reduced-order airpath, NOx, and aftertreatment thermal models, along with the gain scheduled torque controller with Smith predictor, are embedded in dSPACE rapid prototyping controller using Runge Kutta discrete solver with a time step of 10 ms. As shown in Figure 3-13, ECU variables are communicated via a CAN communication line. The dynamometer and other sensors are controlled and measured by a central test cell control system. Figure 3-14 compares the torque reference tracking performance with and without Smith predictor, and it can be observed that the Smith predictor reduces the overshoot caused by the communication delay. The delay in the feedback from the plant and the delay in sending the controller response to the plant causes the controller to overreact causing the overshoot and undershoot. By using the torque model in the Smith predictor the model response guides the controller during the delay period.

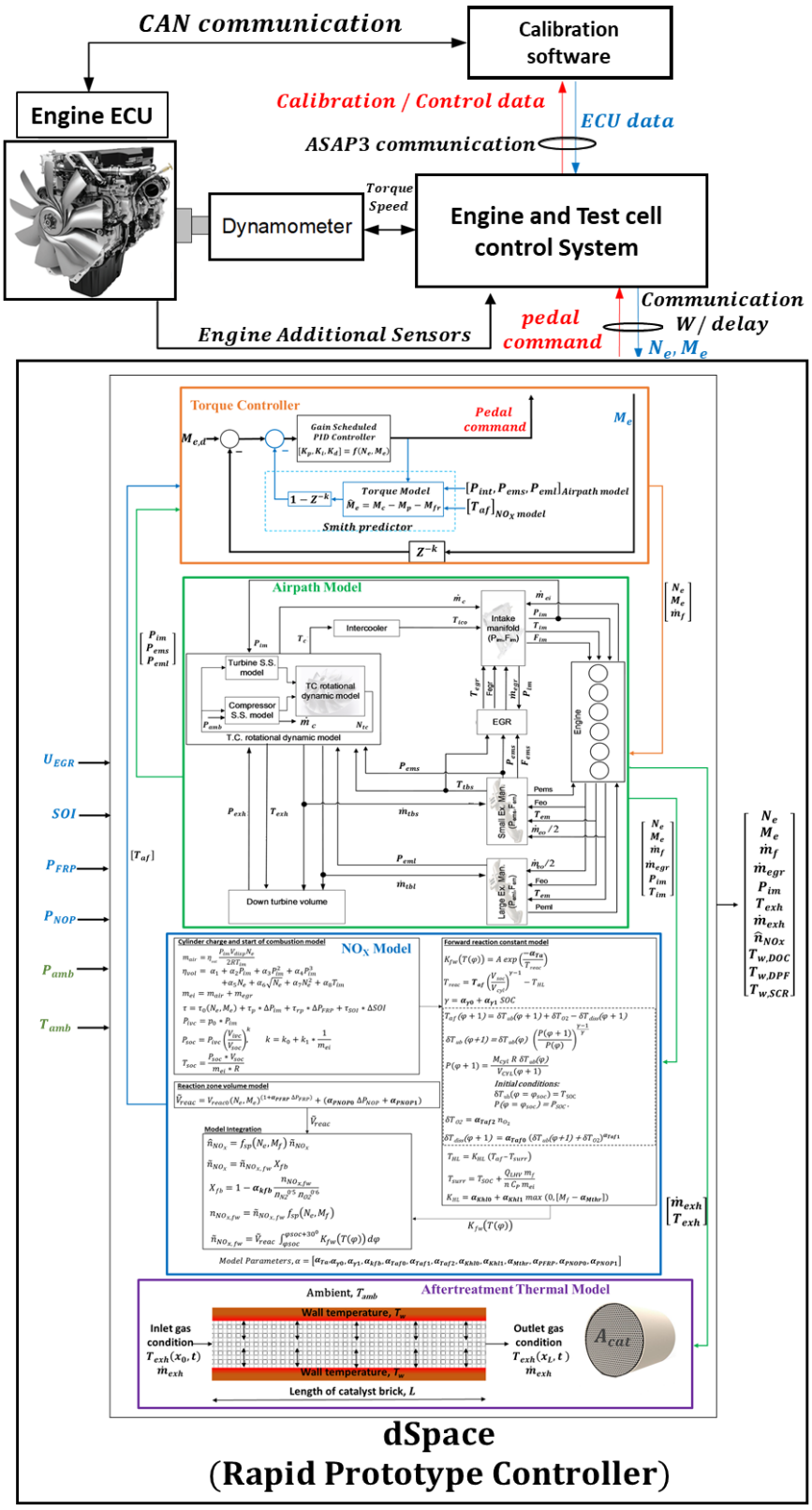

Figure 3-13: Hardware in loop experimental set up.

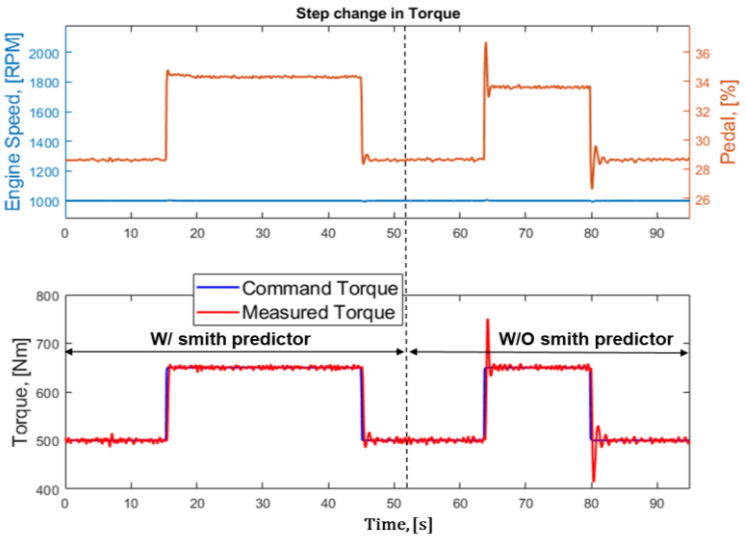

Figure 3-14: Plot showing the improved reference tracking performance of the pedal controller with Smith predictor.

A part of the FTP cycle highlighting the torque reference tracking performance of the torque controller with the Smith predictor loop is shown in Figure 3-15. The torque controller can track the commanded torque very closely without any significant overshoot during the aggressive FTP test cycle.

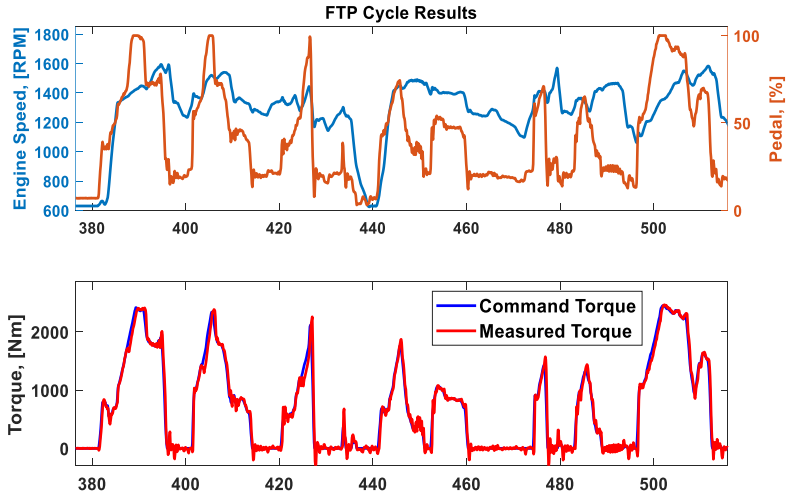

Figure 3-15: Comparison of commanded and measured torque response with gain scheduled proportional integral derivative controller with Smith predictor.

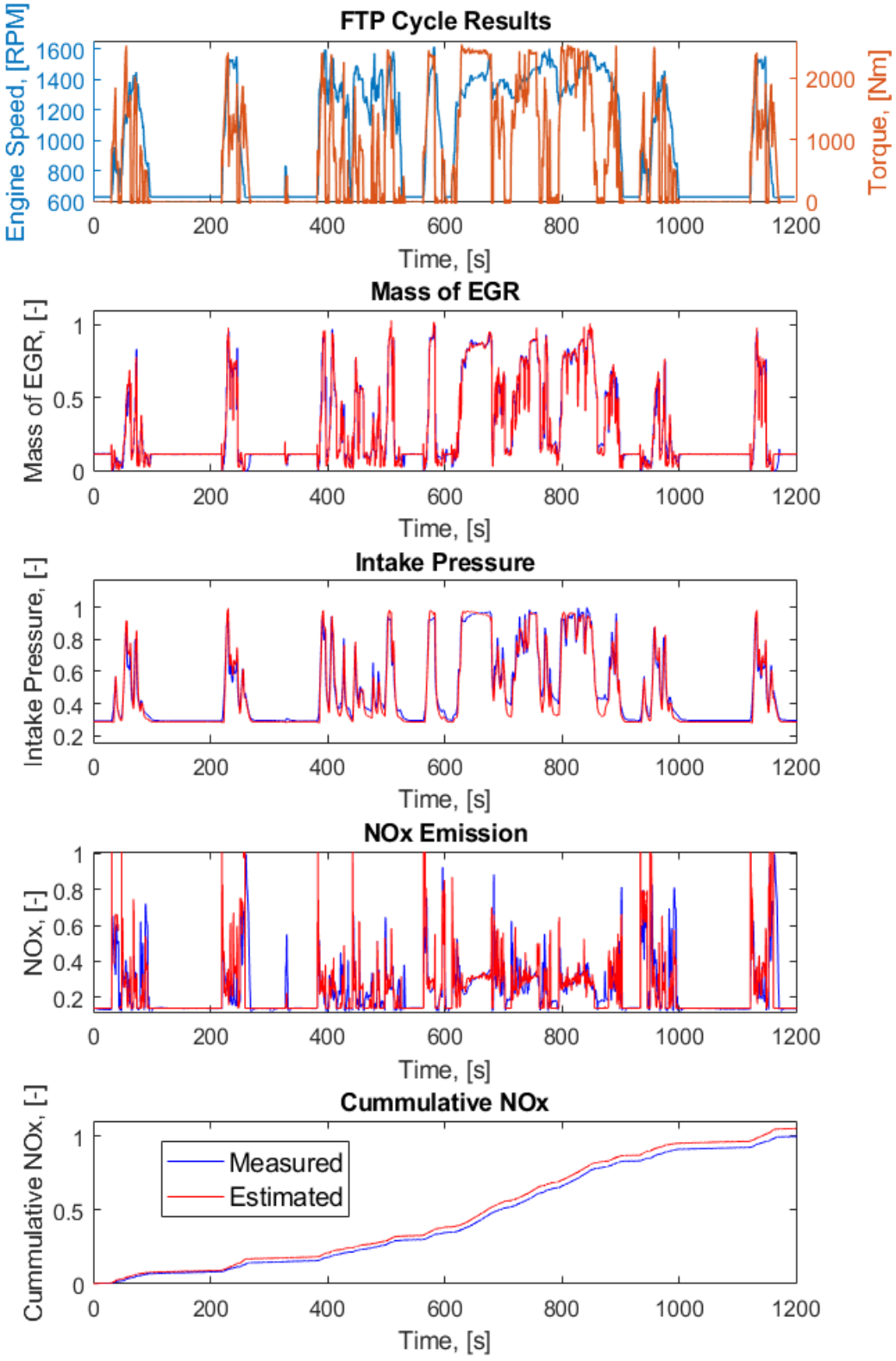

Figure 3-16: Plot comparing airpath and oxides of nitrogen model prediction with measurement.

The results are shown in Figure 3-16, and Figure 3-17 with the closed-loop torque controller tracking the reference FTP torque. Figure 3-16 shows the comparison between model-predicted and measured values of EGR, intake manifold pressure, and NO_X (normalized) for a complete FTP cycle. It is observed that the reduced-order model can predict the fast transients in the mass of EGR, intake pressure, NO_X, and aftertreatment thermal states. The cumulative NOx estimated over an FTP cycle is more than 95 % accurate compared to the measured value. Figure 3-17 shows the comparison between estimated and measured exhaust gas temperature for DOC, DPF, and SCR simulated for a hot FTP cycle. It is observed that the thermal model can effectively capture the transient temperature evolution.

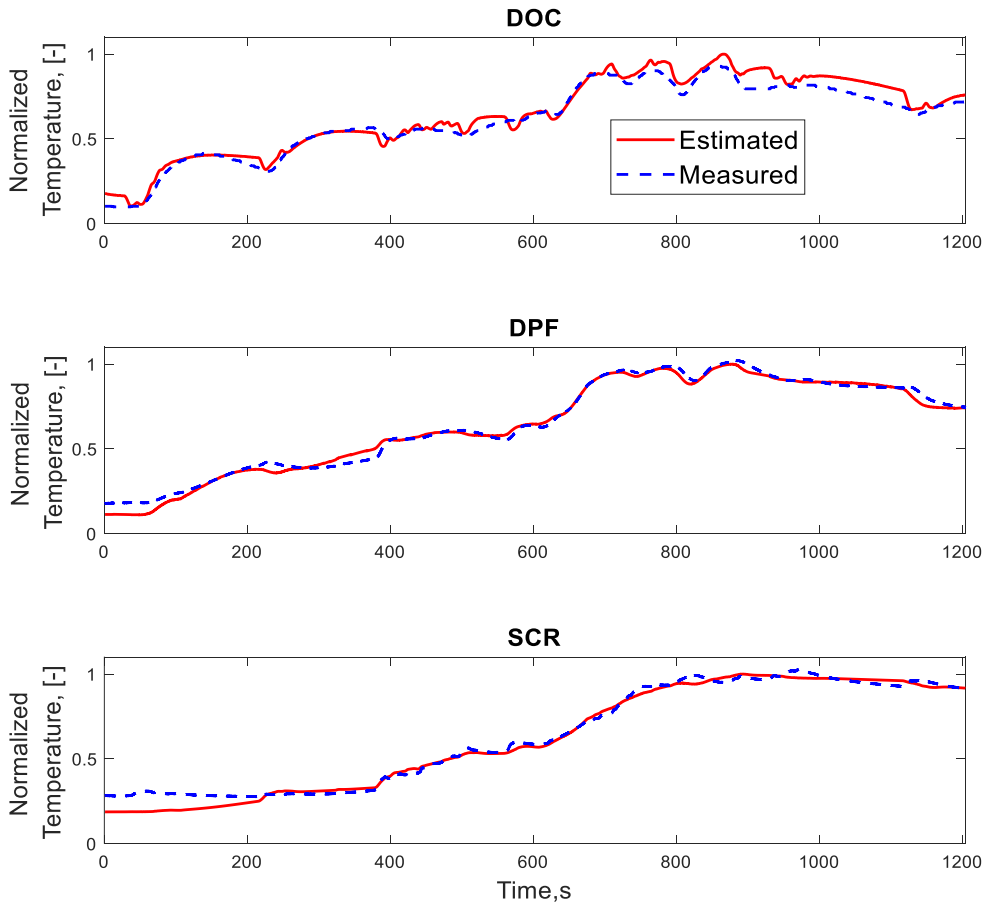

Figure 3-17: Comparison of normalized catalyst temperature over the federal test procedure cycle between estimated and measured data.

3.7 Summary

A framework is presented for integrated modeling of a heavy-duty diesel engine airpath and NOx emissions as well as aftertreatment thermal behavior. The models were developed with high sensitivity to control variables, enabling reliable prediction of vehicle fuel consumption and tailpipe emissions for a modern diesel engine with a modern airpath design. With the reduction of the model order, real-time implementation with a larger execution step size was realized on rapid prototype hardware. Tested and compared with experiments, the NOx emission model captured critical transients using estimated input variables from the reduced-order air path model. The cumulative NOx emission estimation over a federal test procedure (FTP) cycle is more than 95 % accurate compared to the measured value. A gain scheduled torque controller with an integrated Smith predictor for network signal communication delay cancelation was used to track the demanded torque despite disturbance from manipulating the control signals. The presented model provides a solid basis for virtual simulation and real-time predictive control applications in the next chapters and inspires continuation of this line of work and approach for the future efficient and clean combustion engines.

Chapter 4 Rate-based Model Predictive Controller

In this chapter, a rate-based MPC controller formulation to track a reference P_{im} with engine-out NO_X ($NO_{X_{eng}}$) emission constraint is presented. The unique EGR valve arrangement in this engine introduces challenges for independent control of P_{im}, and EGR flow rate. The start of injection (SOI) and EGR valve position are used as the control variables to track P_{im} with engine-out NO_X constraint. This chapter takes the opportunity of using online linear MPC with full state feedback. With the state feedback it is seemingly possible to manage associated airpath nonlinearities and achieve a one-step ahead prediction. This approach also significantly reduces the controller calibration effort and memory requirement. The plant model for the one-step prediction is obtained by the linearization of a physics-based reduced-order airpath and engine-out NO_X model. This rate-based MPC controller was experimentally validated with the gain-schedule torque controller of chapter 3 and augmented with a Smith predictor to compensate for hardware-in-loop network communication delay.

4.1 Linear engine airpath and NOx emission model

In this section, the linearized reduced order physics-based nonlinear engine and emissions model is explained. The reduced-order airpath and engine-out NO_X models were integrated and linearized around a nominal operating point at engine speed 1000 RPM and engine torque 1500 Nm. This nominal point corresponds to vehicle cruising speed at 70 miles per hour.

Table 4-1 shows the linearized airpath and NO_X emission model states, and inputs. The integration time step of the linear model is 10 ms. The model relies on six nonlinear states, specifically 3 pressure states P_{im}, P_{eml}, P_{ems} in the intake, exhaust large, exhaust small manifolds, the temperature T_{tb}, the turbocharger speed ω_{tc} and the engine-out NOx $NO_{X_{eng}}$. The inputs to the nonlinear airpath model are engine speed N_e, mass of fuel M_f, EGR valve position, and start of fuel injection crank angle. Due to the nonlinear dynamics of this valve, accurate one-

step prediction EGR flow rate depends on all the exhaust states P_{eml}, P_{ems}, and T_{tb}. Hence removing those states results in poor prediction per the model order reduction procedure explained in section 3.3.

Table 4-1: Linear model states, inputs and outputs

	Symbol	***Description***	***Units***
States	P_{im}	Intake manifold pressure perturbation	kPa
	P_{ems}	Exhaust manifold pressure at small scroll perturbation	kPa
	P_{eml}	Exhaust manifold pressure at large scroll perturbation	kPa
	T_{tb}	Temperature of gas upstream turbocharger perturbation	K
	ω_{tc}	Turbocharger angular velocity perturbation	1/s
	$NO_{X_{eng}}$	Engine out NO_X concentration perturbation	ppm
Inputs	U_{EGR}	EGR valve position perturbation	%
	U_{SOI}	Start of fuel injection crank angle perturbation	Crank angle degrees

The airpath and NO_X emission model in linear discrete time form is represented by statespace with state, input and output matrices A, B, $C = I_{6\times6}$ and $D = 0$, since full state feedback is assumed. The discrete-time step is represented with the the perturbed state, and input are given by,

$$x = \left[P_{im}\ P_{ems}\ P_{eml}\ T_{tb}\ \omega_{tc}\ NO_{X_{eng}}\right]^T \tag{4.1}$$

$$u = [U_{EGR}\ U_{SOI}]^T \tag{4.2}$$

$$y = \left[P_{im}\ P_{ems}\ P_{eml}\ T_{tb}\ \omega_{tc}\ NO_{X_{eng}}\right]^T \tag{4.3}$$

As shown in (4.3) output vector $y = x$ since full state feedback is assumed given the sensing. The steady-state values of the state, input, and output are denoted by the vectors $x \in \mathbb{R}^6$, $u \in \mathbb{R}^2$, and $y \in \mathbb{R}^6$. The exogenous inputs to the model are engine speed N_e and mass of fuel M_f.

4.2 Rate-based MPC controller

The rate-based MPC controller is a linear quadratic-based command tracking formulation that directly exploits the incremental model and offers zero steady-state offsets when the constraints are inactive in the presence of constant additive disturbances, as shown in [38], [67]. We define the state rate ($\Delta x_k = x_k - x_{k-1}$), control rate ($\Delta u_k = u_k - u_{k-1}$), and P_{im} tracking error ($e_k = P_{im} - r_{k-1}$). where r is the desired P_{im} reference.

$$\Delta x_k = x_k - x_{k-1}, \tag{4.4}$$

$$\Delta u_k = u_k - u_{k-1}, \text{and} \tag{4.5}$$

$$e_k = P_{im} - r_{k-1} \tag{4.6}$$

where r is the desired P_{im} reference. Table *4-2* shows the actual physical constraints. Constraints are applied on P_{im} and $NO_{X_{eng}}$ to ensure safe engine operation and to control fast transient engine out NO_X.

Table 4-2. Actual physical constraints

Constraint	***Symbol***	***Minimum***	***Maximum***
State	P_{im}	98 kPa	400 kPa
	$NO_{X_{eng}}$	0 ppm	$NO_{X_{cstr}}$ ppm
Control	U_{EGR}	5%	95%
	U_{SOI}	-10 bTDC	20 aTDC

where $NO_{X_{cstr}}$ is a time-varying engine-out NO_X constraint in ppm. The extended state vector is given by:

$$x_k^{ext} = [\Delta x_k^T \; e_k^T \; u_{k-1}^T \; x_{k-1}^T]^T. \tag{4.7}$$

where,

$$\Delta x_{k+1} = A\Delta x_k + B\Delta u_k, \text{and} \tag{4.8}$$

$$e_{k+1} = CA\Delta x_k + CB\Delta u_k + e_k. \tag{4.9}$$

The extended state prediction model is given by:

$$x_{k+1}^{ext} = \bar{A}x_k^{ext} + \bar{B}\Delta u_k, \tag{4.10}$$

where,

$$\bar{A} = \begin{bmatrix} A & 0 & 0 & 0 \\ CA & I_{n_e \times n_e} & 0 & 0 \\ 0 & 0 & I_{n_u \times n_u} & 0 \\ I_{n_x \times n_x} & 0 & 0 & I_{n_x \times n_x} \end{bmatrix}, \text{and} \tag{4.11}$$

$$\bar{B} = \begin{bmatrix} B & CB & I_{n_u \times n_u} & 0 \end{bmatrix}^T. \tag{4.12}$$

where $n_x = 6$ is the number of states, $n_u = 2$ is the number of inputs, and $n_e = 1$ is the number of tracking variables.

4.2.1 Quadratic cost

The quadratic cost J_N, assuming the prediction, control, and constraint horizons are all equal to N is expressed as below:

$$\min_{\Delta u_k \epsilon \{0, \ldots . N-1\}} J_N = (x_N^{ext})^T P_N (x_N^{ext}) + \sum_{k=0}^{N-1} [(x_k^{ext})^T Q^{ext} (x_k^{ext}) + (\Delta u_k)^T R^{ext} (\Delta u_k)] \tag{4.13}$$

The terminal penalty P_N is added to ensure closed-loop stability.

$$\tilde{A} = \begin{bmatrix} A & 0 \\ CA & I_{n_e \times n_e} \end{bmatrix}, \tilde{B} = \begin{bmatrix} B \\ CB \end{bmatrix}, Q = diag[0\ Q_e], R_{n_u \times n_u}, \text{and } P_N = diag[\tilde{P}_\infty\ 0] \tag{4.14}$$

where $\tilde{P}_\infty$ is the solution of the discrete-time algebraic Riccati equation corresponding to $\tilde{A}$ and $\tilde{B}$ calculated at the model linearization point. Q_e is weight for tracking, and R is the weight for control actuator. Based on experimental iteration the value for Q_e was chosen as 1000 and the value for is $R = diag[1, 1]$. The discrete plant model corresponding to the linearization point at 1000 engine RPM and 1500 Nm engine torque is provided in .

4.2.2 Quadratic cost solution

The cost function J_N is reduced to standard quadratic program (QP) form as shown in (4.1 and 4.) with the state and control constraints; refer to for the details. A standard dual projected gradient algorithm is used to solve the cost function; refer to Appendix B for the complete algorithm. The solver runs in warm-start strategy by using the previous iteration solution as the initial condition for the next iteration, except for the first iteration in which the initial condition is zero.

$$\min_{U\epsilon\mathbb{R}^{N\times n_u}} J_N = \frac{1}{2}U^T HU + q^T U, \text{and} \tag{4.15}$$

$$subject\ to\ GU \leq W + Tx_0. \tag{4.16}$$

where U is the solution vector, H is the Hessian matrix, q is a linear function with initial conditions, W is the constraint vector, and G is the state vector. This implicit MPC formulation for real-time control is made possible by avoiding plant scheduling. The latter involves multiple matrix inversions, which is an expensive computational load and prevents us from a real-time implementation. A single plant model is selected in the entire engine operating range and used in conjunction with the nonlinear plant model to provide feedback through an observer.

4.2.3 Kalman Filter

Full state feedback x_{meas} is available through the engine-mounted sensors. The non-physical rate-based state $\Delta\hat{x}_k$ is estimated using a Kalman filter using (4.3) and (4.). The implementation of this control algorithm is shown in Figure 4-1. The gain k is designed for the state and output rates which control the direct feedthrough. The value of $k = 0.95 \times [I_{5\times5}]$ which is obtained by trial and error method observing the controller tracking performance.

$$\hat{x}_k = A\hat{x}_{k-1} + Bu_{k-1} + k(x_{meas} - \hat{x}_{k-1}) \tag{4.17}$$

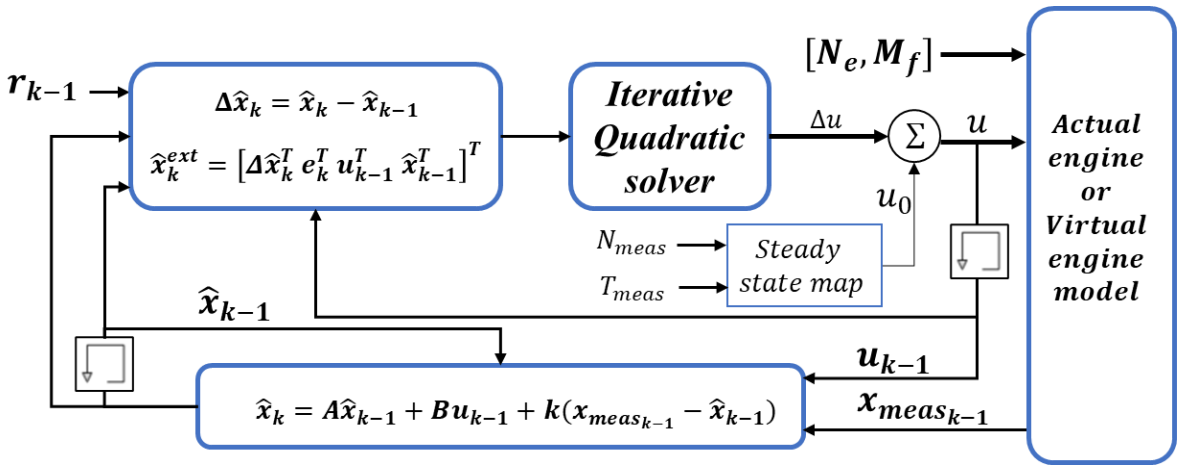

Figure 4-1 Schematic layout of rate-based model predictive controller implementation

The presented controller can also be integrated with the nonlinear observer for engines without a turbocharger speed sensor similar to the one shown in [56] and [69]. For an engine without turbocharger speed sensor, a nonlinear observer may be needed to estimate the turbocharger speed based on the available feedback signals. The high sampling frequency (100 Hz) of the measurements helps correct the linearized model prediction error at other operating points. The effect of sensor dynamics, especially with the NO_X sensor and its impact on Kalman filter estimation, is not considered in the current study.

4.3 Real-time implementation

In this section, the rate-based MPC is implemented in a real-time environment and validated through simulation and HIL experiments.

4.3.1 Simulation results

The rate-based model predictive controller is simulated with the nonlinear physics-based engine and emission model. The prediction, control, and constraint horizon are equal, and it is ten steps with an integration step time of 10 ms. As shown in Figure 4-2, subplot 1, the reference intake manifold pressure (r) marked in the dashed black line is varied in steps to observe the controller performance in handling reference tracking and constraints handling. The U_{EGR} and U_{SOI} are constrained between 5 % to 95 % and 6.5 to 10.5, respectively. Four different engine-

out NO_X constraint (NOx_{cstr}) are evaluated 2000 ppm (blue), 1500 ppm (magenta), and 1000 ppm (cyan), and their corresponding plots in P_{im}, U_{EGR} and U_{SOI} are shown in Figure 4-2. It can be observed that when NO_X is unconstrained, the controller achieves good tracking of the reference r with zero steady-state offset. As the NOx_{cstr} is tightened, U_{SOI} retards faster to satisfy the constraint. However, the U_{EGR} does not change significantly, and this is due to the plant dynamics that SOI has a faster response to control NO_X then the EGR valve position. Nevertheless, if NOx_{cstr} is too tight, like in the case with 1000 ppm (cyan), the U_{SOI} is retarded to the minimum, and the U_{EGR} is forced to open to satisfy the constraint, and thereby it causes loss of tracking in P_{im} (8 s – 10 s). The constraint violations observed in 1000 ppm case between 7 s to 8 s, 12 s to 14 s, and 16 s to 18 s are due to the U_{SOI} actuator saturation.

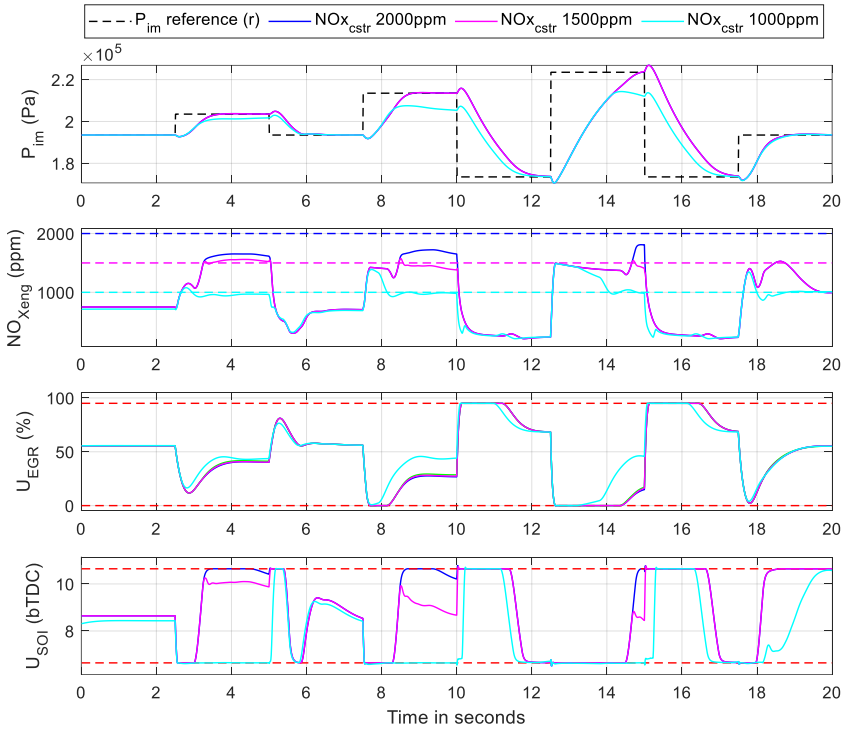

Figure 4-2: Simulation results for step changes in intake manifold pressure reference and oxides of nitrogen constraint at a constant engine speed and torque.

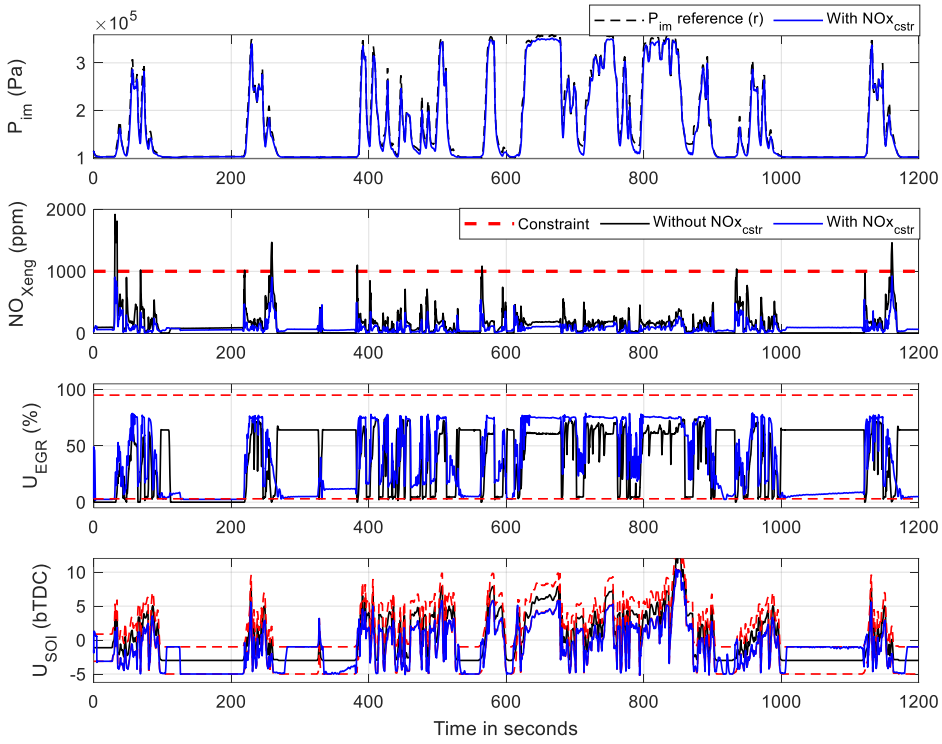

Figure 4-3: Simulation results with rate-based model predictive controller for federal test procedure cycle

As shown in Figure 4-3, the rate-based MPC formulation is simulated to verify the federal test procedure (FTP) cycle's transient performance. The reference P_{im} is the measured intake manifold pressure in the stock engine, and the corresponding U_{EGR}, U_{SOI}, and NO_X are shown in the black line. The MPC controller is evaluated to track the reference boost with the NO_X constraint set at 1000 ppm. The MPC controller tracks the reference P_{im} with a RMSE maximum P_{im} error of 34 kPa. In the unconstrained case as in the stock engine, transient NO_X spikes up to 1900 ppm are observed, while with the MPC controller, the NO_X never exceeds the set 1000 ppm. Typically, the stock U_{SOI} is calibrated to produce maximum brake torque and best fuel economy. The MPC U_{SOI} is constrained within $\pm$2-degree crank angle bTDC from the stock SOI to avoid incurring a hefty fuel penalty. The objective of this controller is to use SOI only to reduce transient NO_X and achieve P_{im} tracking through the EGR valve. Figure 4-4 shows a closer range of the FTP simulation results, where the MPC controller retards the U_{SOI} to satisfy NO_X constraint. Due to U_{SOI} saturation, the U_{EGR} is redundant and does not close further to improve boost, resulting in poor tracking performance, and it can be avoided by relaxing the control constraints on the U_{SOI} .

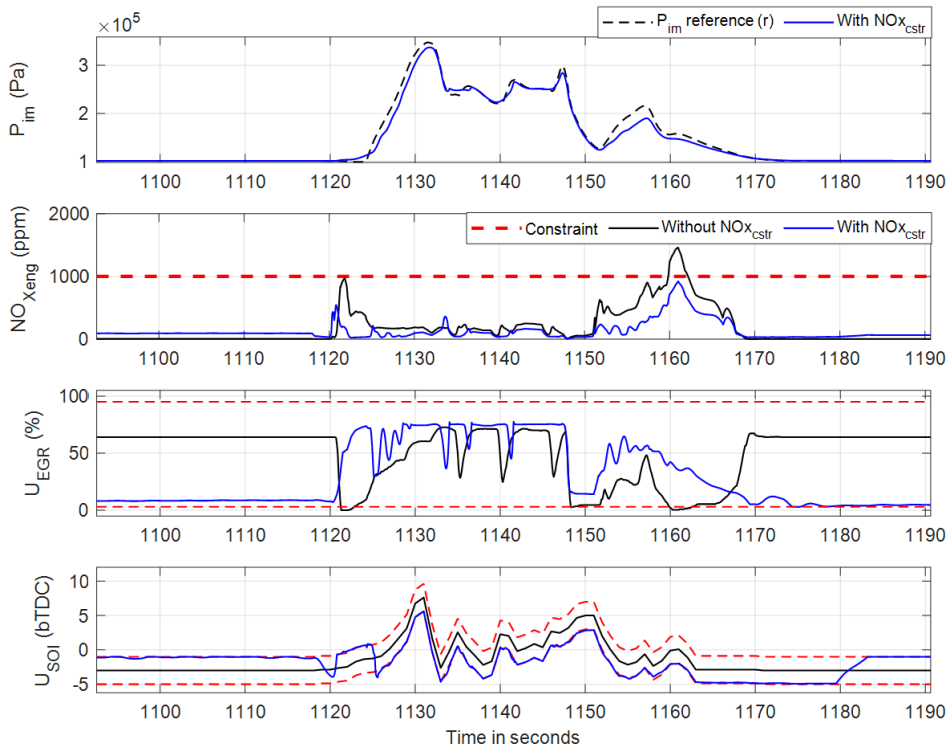

Figure 4-4. Simulation results with the model predictive controller for federal test procedure cycle.

4.3.2 Experimental results

As shown in Figure 4-5, the rate-based MPC controller was implemented in a rapid prototype controller (dSPACE), with the engine and the dynamometer hardware-in-the-loop.

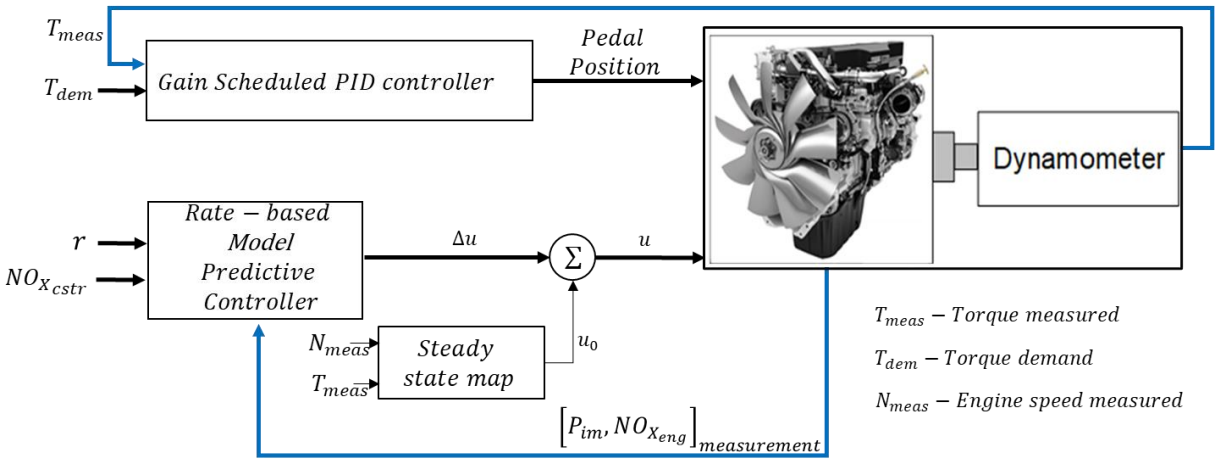

Figure 4-5. Schematic layout of rate-based model predictive controller experimental setup

A gain scheduled torque controller is used to track the reference torque trajectory. A Smith predictor is augmented with the torque controller to compensate for the communication delay between the various hardware and over the network. The controller is experimentally validated with step changes in r and NOx_{cstr} as shown in Figure 4-6. The nominal values of U_{SOI} and U_{EGR} are from a look-up table referenced against actual engine speed and torque. The MPC EGR is constrained to be between 5 % and 95 %. The SOI is constrained between $\pm\ 2^0$ bTDC from the nominal SOI. The controller can effectively track the reference r; offset in tracking is observed when the actuators hit the constraints. The torque controller can maintain the demand torque of 1000 Nm by controlling the pedal position. As shown in Figure 4-7, the controller is experimentally validated over an FTP cycle where the rate-based MPC controller tracks the reference r (which is the stock engine P_{im}) while also satisfying the time-varying NOx_{cstr}.

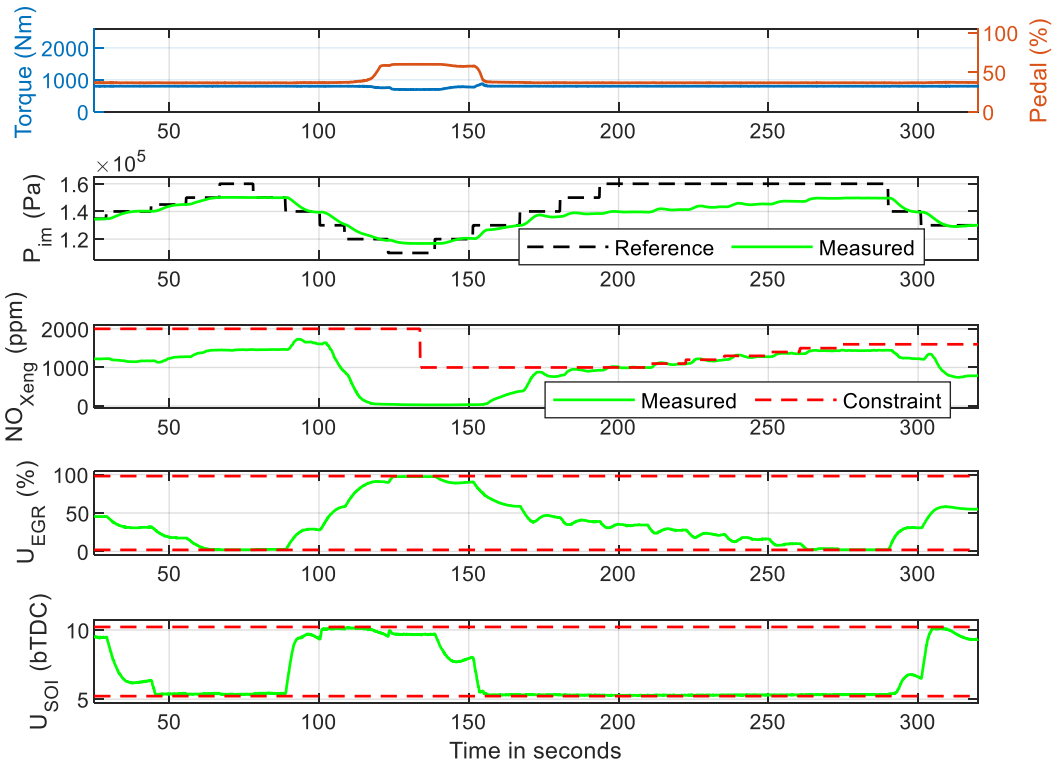

Figure 4-6. Experimental results with rate-based model predictive controller for step changes in reference intake manifold pressure and nitrogen oxides.

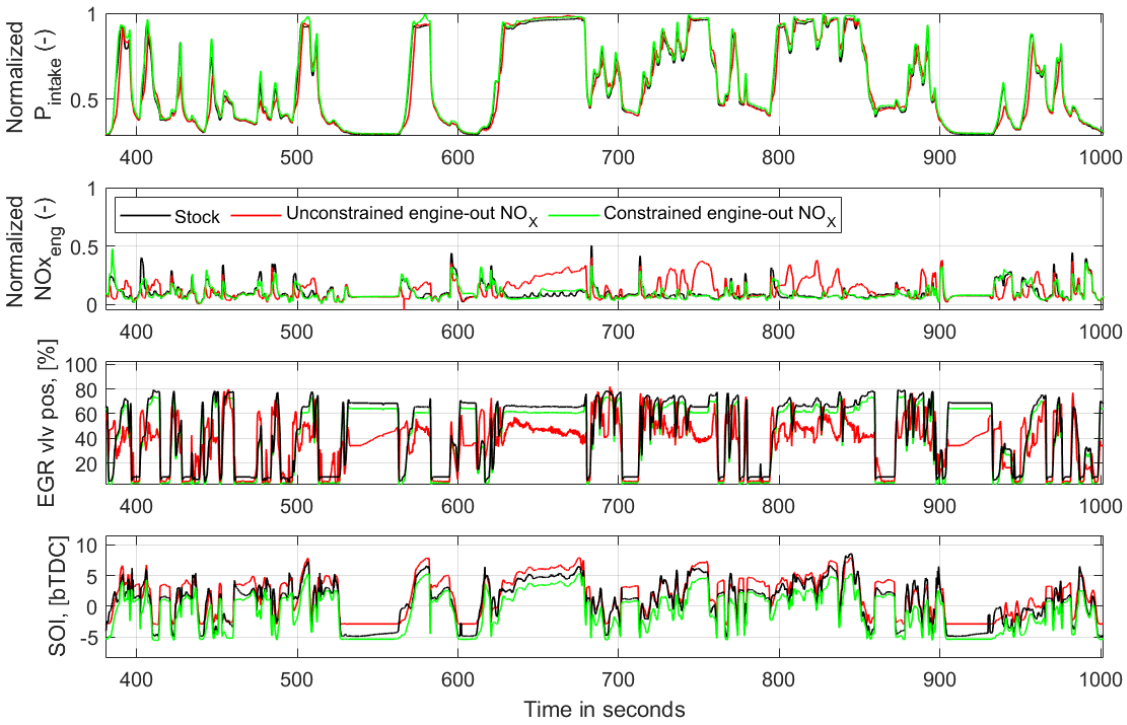

Figure 4-7. Experimental results of rate-based model predictive controller

The MPC controller's effect on aftertreatment performance and some of the critical cycle averaged cumulative parameters are shown in Figure 4-8, and the results are summarized in . Two different cases are compared to evaluate the controller's performance in tracking and constraint handling. First, an unconstraint case, in which the engine-out NO_X constraint NOx_{cstr} was entirely relaxed to evaluate the controller's P_{im} tracking performance. Both U_{EGR} and U_{SOI} are conservatively used to track the reference intake manifold pressure *r*, which increases the fuel economy, which is seen in BSFC benefit of 8.3 %; however, the brake specific engine-out NO_X ($BSNOx_{eng}$) increased by 41 %. The SCR Urea controller attempts to reduce the brake specific tailpipe NO_X ($BSNOx_{tp}$) by increasing the Urea injection quantity by 18 %, which results in 14 % reduction in tailpipe NO_X compared to the stock engine calibration. Second, a constrained case is evaluated, in which the engine-out NO_X constraint is tightened, and now the controller must track the same reference intake pressure *r* as before; while satisfying the time-varying engine-out NO_X constraint NOx_{cstr}. Results show 1.4 % reduction in BSFC, 2 % reduction in engine-out NO_X, 40 % reduction in tailpipe NO_X, and a 6 % reduction in brake specific urea consumption (BSUC).

Table 4-3. Experimental results summary

Critical Metrics (cycle averaged)	***Unconstrained Engine-out NO_X***	***Constrained Engine-out NO_X***
$BSFC$	-8.3 %	-1.4 %
$BSNOx_{eng}$	41 %	-2 %
$BSNOx_{tp}$	-14 %	-40 %
$BSUC$	18 %	-6 %
$Torque\ tracking\ error$	194 Nm (RMSE)	130 Nm (RMSE)
$P_{im}\ tracking\ error$	161.6 kPa (RMSE)	39.2 kPa (RMSE)

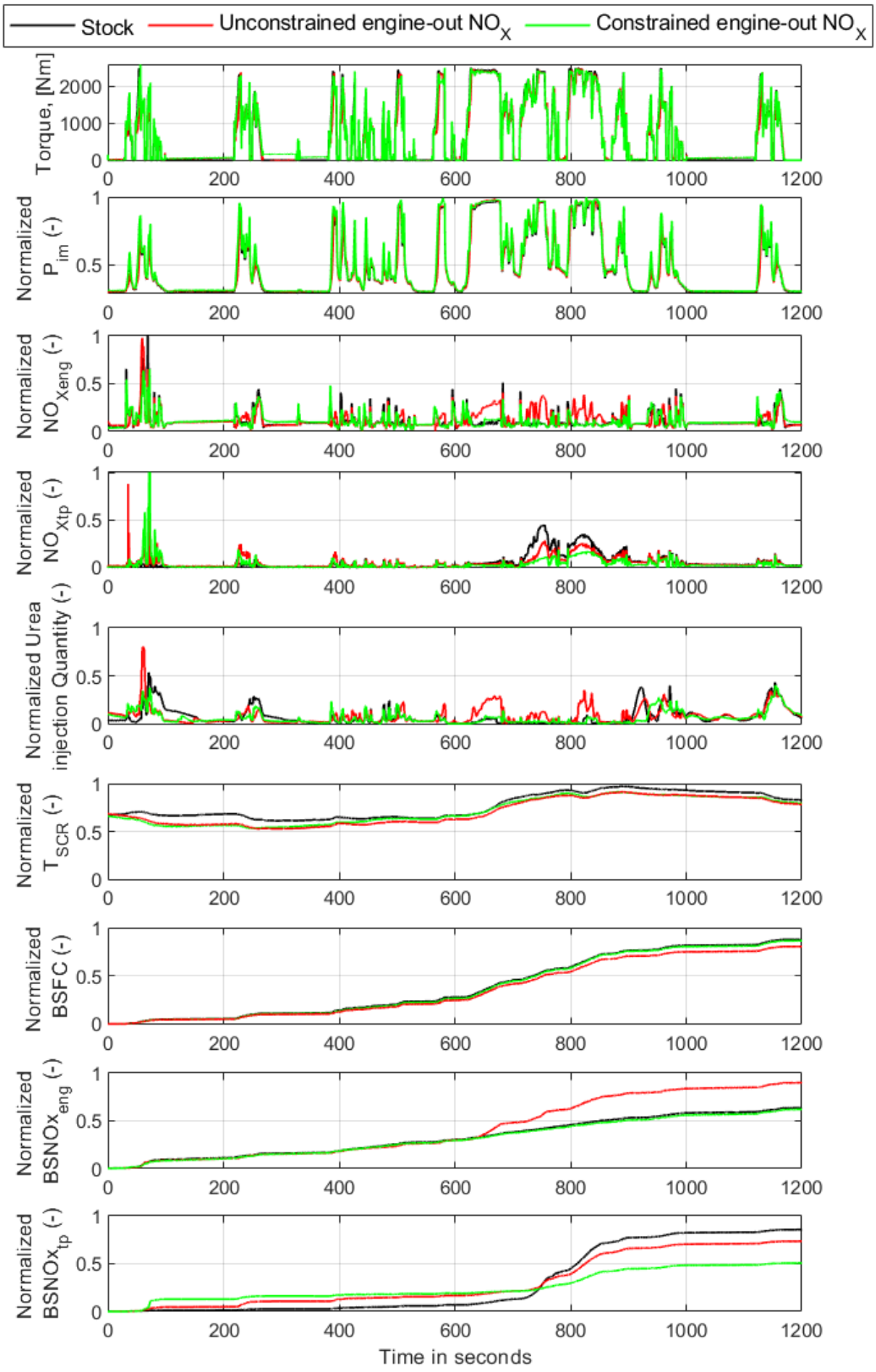

Figure 4-8. Experimental results showing the critical engine and aftertreatment metrics

4.4 Conclusion

Rate based MPC is an effective formulation to track reference P_{im} with NOx_{eng} constraints. The earlier chapter model order reduction allowed us to measure all the states of the model used for the MPC, and thus enabled the real-time implementation in dSPACE. This controller can be used as a stand-alone P_{im} controller or in a hierarchical architecture as will be shown in the next chapter. Experimental results show up to 1.4 % improvement in BSFC, 2 % reduction in engine-out NO_X, 40 % reduction in tailpipe NO_X, and a 6 % reduction in brake specific Urea consumption (BSUC). The effect of sensor dynamics especially with the NO_X sensor and temperature sensors and its effect on Kalman filter estimation along with possible integration with non-linear observer to be addressed in the future work. In this work we implemented a Kalman filter to perform the one-step (0.1 s horizon) prediction needed for the MPC.

Chapter 5 Hierarchical Predictive Thermal Management and Fuel Optimization

In this chapter, a hierarchical predictive controller is introduced to manage the tradeoff between the BSFC and $BSNO_X$. As shown in Figure 5-1, the architecture consists of two MPC controllers with different prediction horizons. The high-level (supervisory) controller utilizes a long prediction horizon of 20 s to provide fuel and NO_X emission optimal intake manifold pressure and SOI reference. The low-level MPC controller utilizes a short prediction horizon of 0.1 s and tracks the reference intake manifold pressure and SOI. The low-level MPC controller also controls the fast transient engine-out NO_X spikes, which is enforced as a constraint as shown in chapter 4. A torque controller which was developed previously shown in chapter 3 is used to track the demand engine torque, and a reference governor is used to regulate λ above a reference λ_{ref} to avoid smoke. This complete control architecture was implemented on a rapid prototype controller and validated in real-time through a software-in-the-loop (SIL) simulation with the nonlinear virtual engine model consisting of engine airpath, NO_X, and aftertreatment model. The sections below are organized as follows. First, an overview of the supervisory controller is presented. Second, the reference governor's details are shown, and finally, the hierarchical predictive controller SIL implementation and validation results are presented.

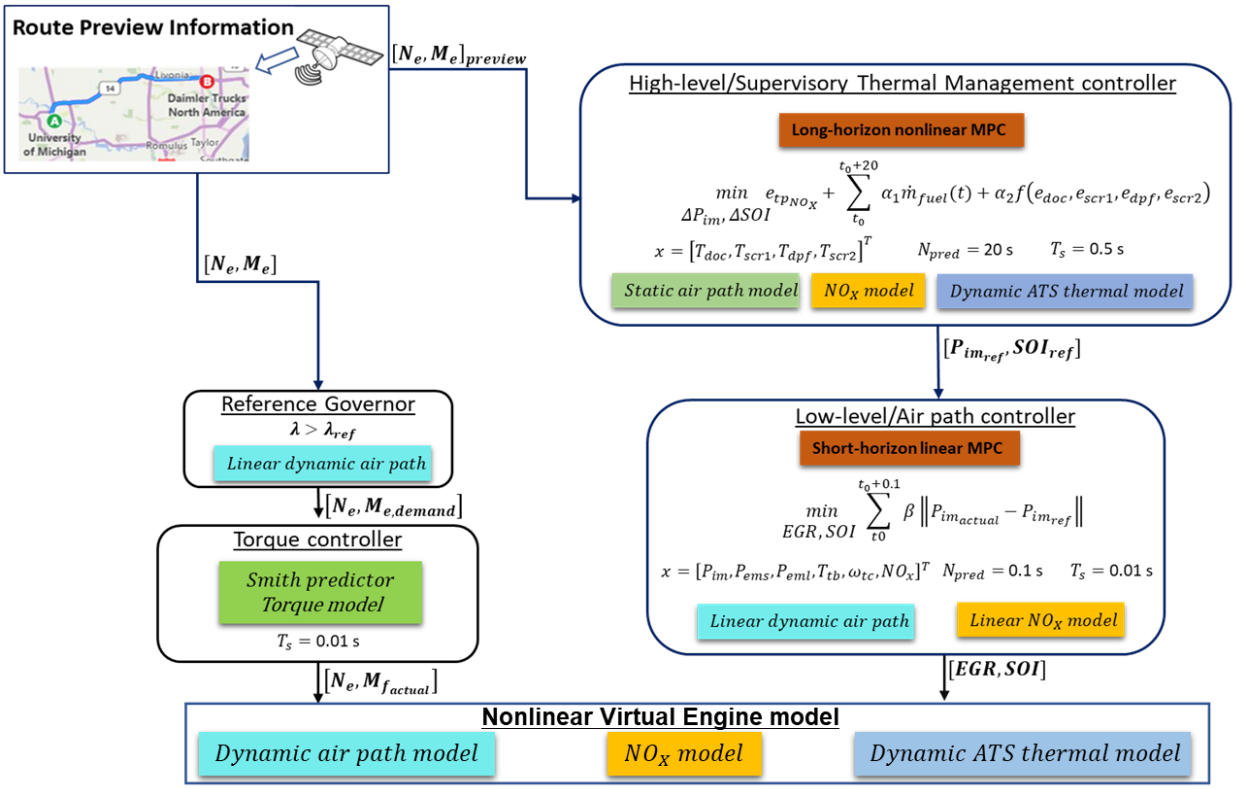

Figure 5-1: Hierarchical predictive controller architecture

5.1 Supervisory Thermal Management

The objective of the thermal management is to control the exhaust gas enthalpy such that the aftertreatment system (ATS) catalysts reach a reference temperature, T_{ref}, which is set as 210 °C as fast as possible, and stay above it. Thus, for the catalyst i, with the temperature error e_i,

$$e_i = T_{i,ref} - T_i \tag{5.1}$$

the ATS controller ensures $e_i \leq 0$. Together with the lag dynamics considered for the gas temperature passing the turbine, T_{tc}, the 5th-order ATS is modeled with the state vector $X = [T_{tc}, T_{doc}, T_{scr1}, T_{dpf}, T_{scr2}]$ being the wall temperature of the turbine and ATS bricks. Two additional temperature states T_{tc} and T_{scr2} are added to improve the ATS thermal model prediction. A model predictive controller is formulated to calculate the input vector $U = [P_{im}, SOI]$ at each time step k.

$$[Pim, SOI]^*|_k = \underset{P_{im},\ SOI}{\operatorname{argmin}}\ \alpha_1 e_{Tp} NO_x|_{t0+T_h-1} + \sum_{k=t_0}^{t0+T_h-1} J|_k \tag{5.2}$$

sub to:

$$X|_{k+1} = F_{ATS}(X, \dot{m}_{exh}, T_{exh})|_k \tag{5.3}$$

$$[\dot{m}_{exh}, T_{exh}, P_{ems}, P_{tbl}]|_k = F_{AP}(q_f, U)|_k \tag{5.4}$$

$$q_f|_k = F_{Me}(M_{e,req}, N_e, P_{ems}, P_{tbl}, U)|_k \tag{5.5}$$

$$\dot{m}_{TpNOx}|_k = F_{NOx}(X, U, N_e, M_e)|_k \tag{5.6}$$

$$e_{TpNOx}|_k = M_{TpNOx}|_k - M_{TpNOx,ref}|_k \tag{5.7}$$

$$M_{TpNOx}|_k = \sum_0^k \dot{m}_{TpNOx}\ |_i \tag{5.8}$$

$$\lambda > \lambda_{min} \tag{5.9}$$

$$U|_k \subset U^2, X|_k \subset x^5 \forall k \subset [t_0, .., t_0 + T_h - 1] \tag{5.10}$$

where, P_{ems} and P_{tbl} are the small and large exhaust manifolds pressures, $M_{e,ref}$ is the reference torque for the engine, and λ is the equivalence air-fuel ratio. The objective function $J|_k$ is selected such that the fuel consumption is minimized and $T > T_{ref}$ for all ATS bricks. The following cost is proposed as the objective function at each step k in (5.2).

$$J|_k = \begin{Bmatrix} \alpha_1 e_{doc} u(e_{doc}) + \alpha_2 e_{scr1} u(e_{scr1}) + \alpha_3 e_{dpf} u(e_{dpf}) + \alpha_4 e_{scr2} u(e_{scr2}) \\ +\alpha_5 q_f N_e (1 - u(e_{doc}))(1 - u(e_{scr1}))\left(1 - u(e_{dpf})\right)(1 - u(e_{scr2})) \end{Bmatrix}|_k \Delta t_s \tag{5.11}$$

In (5.11), N_e is the engine speed, $\alpha_i, i = 1, \dots, 5$ is the tuning weight, Δt_s is the step time, and u is the unit function.

$$u(e_i) = \begin{cases} 1 & e_i > 0 \\ 0 & e_i \leq 0 \end{cases} \tag{5.12}$$

The objective function in equation (5.11) is designed such that:

1- Penalty terms for temperature error of all catalysts are included as far as

$$T_i < T_{ref} \;\; i \in \{doc, scr1, dpf, scr2\}.$$

2- Fuel is not penalized during the warm-up strategy. This will increase the fuel consumption when ATS is cold. However, the fuel-saving strategy (which are allowed when $T > T_{ref}$) will be activated earlier than a nonoptimal stock ECU strategy.

Model constraints in equation (5.3 - 5.5) indicate that the complete engine and aftertreatment model is split into two groups of sub-models 1) the ATS dynamical thermal model (5.3) and 2) the static air path and torque models (5.4 and 5.5). Including the air path and torque as static model constraints has the following benefits,

1- The static models exclude states related to a conventional air path dynamical model. It also does not consider q_f as a control variable in the optimal control problem. The required fuel to maintain the desired torque is calculated by the internal torque controller F_{Me}.

2- A conventional air path model has very fast dynamics, requiring the simulation and optimal control problem to be computed at small time steps to keep the simulations stable and reliable. The thermal dynamics of the ATS, on the other hand, is very slow, and one can select a larger (compared to the air path dynamics) time step to solve and optimize it. Therefore, by using the static air path, the optimization time step Δt_s is increased effectively.

The engine and aftertreatment system model in (5.3 - 5.5) are divided into three major sub-models. 1) ATS thermal dynamics, F_{ATS}, 2) air path static model, F_{AP} , and 3) engine brake torque F_{Me}. The ATS thermal dynamics model is shown in chapter 3, section 3.5. The complete architecture of the static airpath model and the brake torque model can be found elsewhere [45].

5.2 Reference Governor

To avoid tailpipe smoke, the actual engine air to fuel equivalence ratio λ need to be maintained above a reference air to fuel equivalence ratio λ_{ref}. A scalar reference governor (SRG-EX) is used to enforce this as λ constraint. Reference governor is an add-on control

scheme that can be used along with an existing control architecture. This SRG-EX is used along with the previously designed and experimentally validated torque controller. The complete algorithm is provided in . Figure 5-2 shows the simulation results of the SRG-EX for a step-change in torque demand at a constant engine speed of 1000 RPM. Two cases are compared, one is with SRG-EX, and the other is without SRG-EX. In the SRG-EX case, the torque reference is manipulated by the controller to maintain the actual lambda above a set reference value of λ_{ref} = 1.3 at all operating conditions. The λ control with SRG-EX was not experimentally validated since the baseline controller was adequate and our transients (the duty cycle considered) were not as demanding.

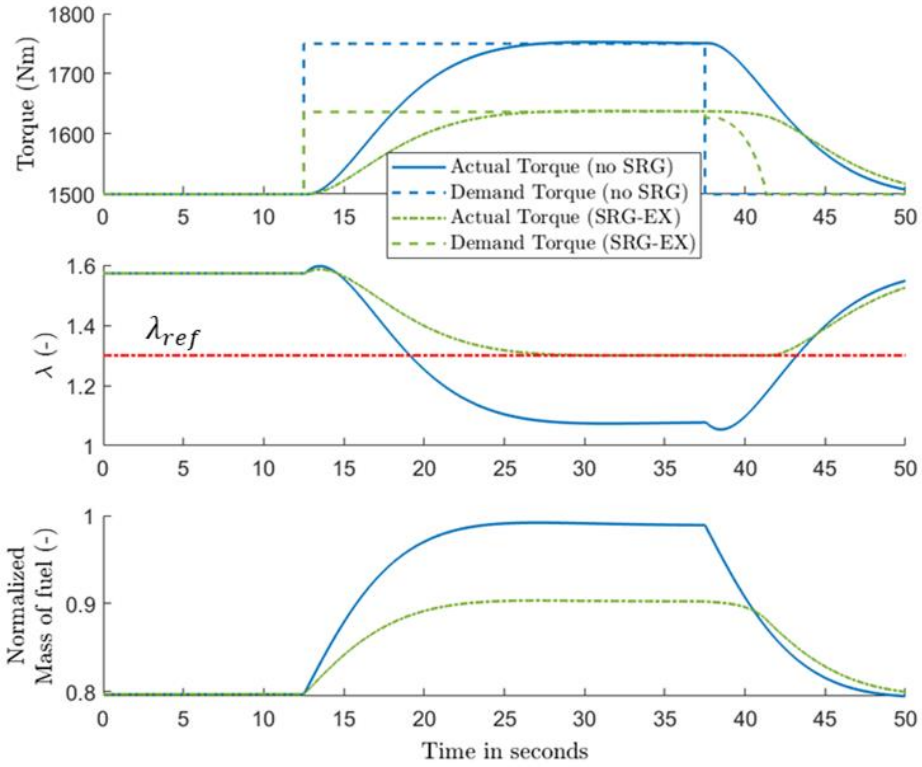

Figure 5-2: Simulation results of explicit scalar reference governor for step-change in demand torque.

5.3 Software in the loop simulation of hierarchical model predictive controller

The hierarchical predictive controller architecture consists of the Supervisory thermal management controller with a prediction horizon of 20 s, the air path controller with a prediction horizon of 0.1 s, and the gain scheduled PID torque controller with the reference governor, as shown in 2. The nonlinear airpath model, NO_X model, and aftertreatment thermal model are integrated together and used as a nonlinear virtual engine model. The high-level controller's optimal control problem is solved using GPOPS-II software, which is a nonlinear program solver integrated in the MATLAB environment. The toque controller, the air path controller, and the nonlinear virtual engine model are embedded in the rapid prototype controller (dSPACE). The computation time in the high-level controller to solve for one optimal move is 5 s. Hence the references for the low-level controller are updated every 5 s. The rest of the components in the dSPACE runs with a discrete-time step of 10 ms with an update frequency of 100 Hz. The nonlinear virtual engine model provides full state feedback to all three controllers.

5.4 Results and discussion

The hierarchical MPC (H-MPC) is simulated over a cold FTP cycle, where the ATS initial temperature is 25 °C. Two cases are considered, one with engine-out NO_X constraint and the other without engine-out NO_X constraint. The significance of the engine-out NO_X constraint is evident from Figure 5-3. The brake specific engine-out NO_X ($BSNO_{X_{eng}}$) reduces by 24 %, without any fuel penalty. However, without engine-out NO_X constraint, the engine-out NO_X increases by 10 % against the stock, along with a fuel penalty of 0.7 %. Due to the higher engine-out NO_X the tailpipe NO_X is also higher in the case without constraint. The actual values and the percentage change are shown in Table 5-1. As shown in Figure 5-4, with engine-out NO_X constraint, the transient NO_X is efficiently controlled below the stock engine-out NO_X. The fast transient NO_X spikes observed in the stock case is reduced with the engine-out NO_X constraint.

Table 5-1. Comparison of critical parameters with and without engine-out NO_X constraint at 25°C ATS initial temperature

	Case I **Unconstrained Engine-out NOx**	Case II **Constrained Engine-out NOx**
BSFC	0.7%	-0.3%
$BSNO_{X_{eng}}$	10%	-24%
$BSNO_{X_{tp}}$	-48%	-56%

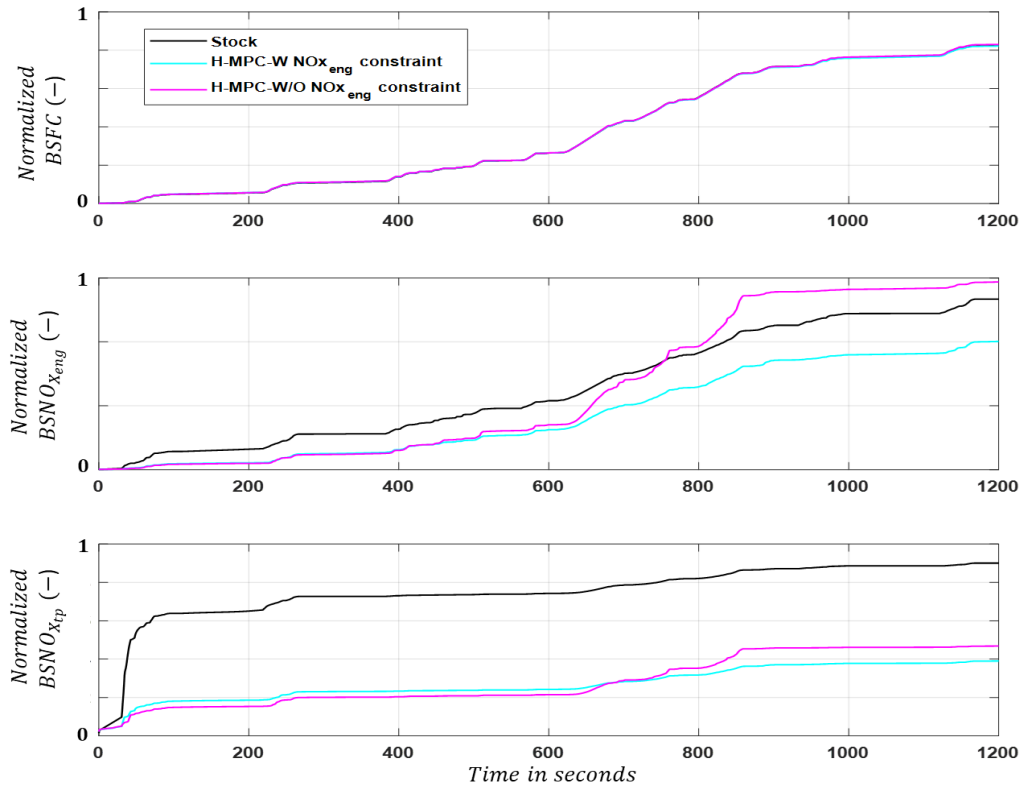

Figure 5-3: Software-in-the-loop results comparing critical cumulative parameters with and without engine-out oxides of nitrogen constraint against stock.

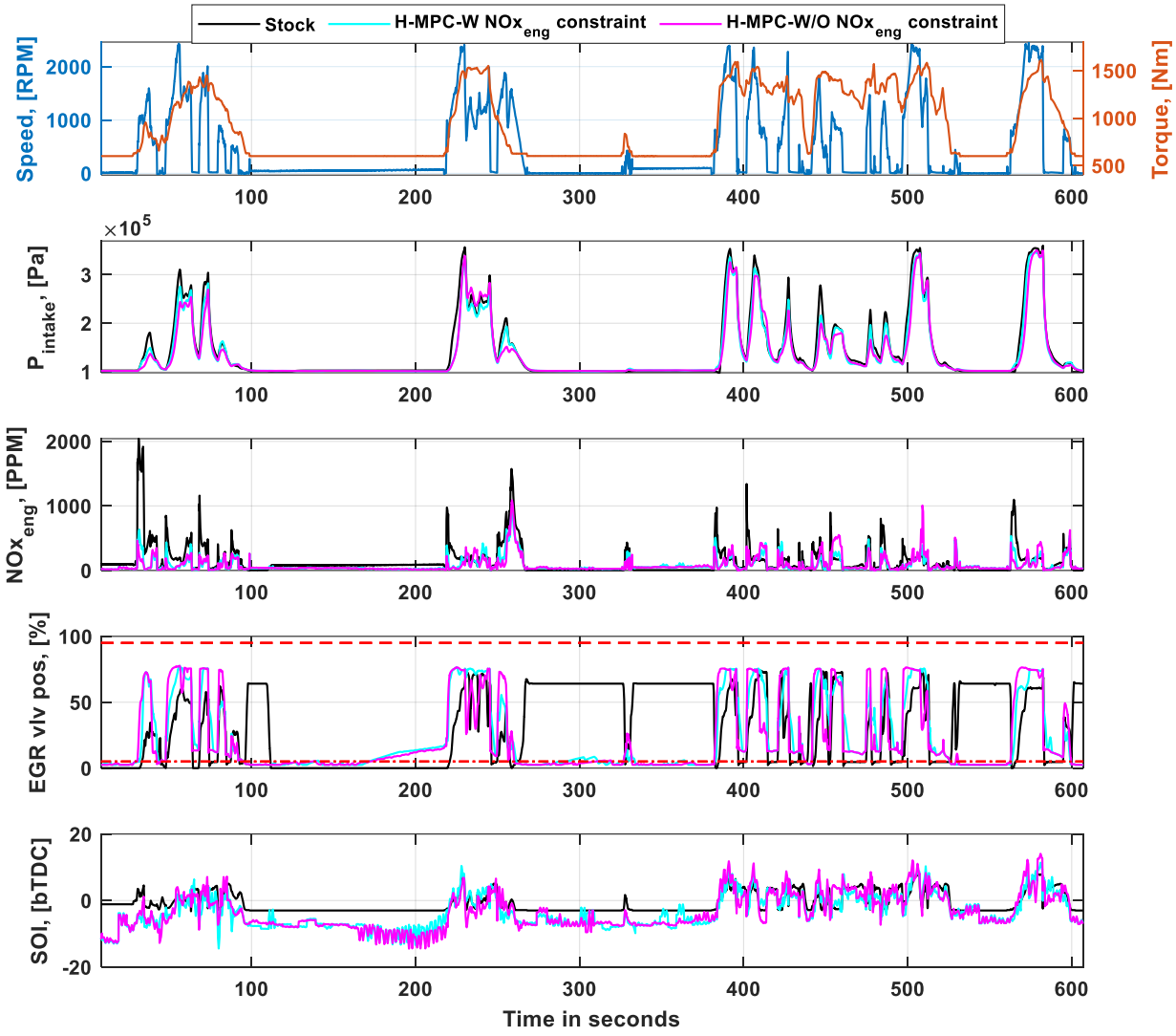

Figure 5-4: Software-in-the-loop results comparing critical control parameters with and without engine-out oxides of nitrogen constraint against stock.

As shown in Figure 5-5, the high-level controller is efficient in maintaining the ATS catalysts temperature above the set point temperature, which is 210 °C in this case. During the first 200 s,

the SOI is retarded to increase the engine-out exhaust gas temperature. After the ATS temperature is above the setpoint, the SOI is advanced to improve fuel economy.

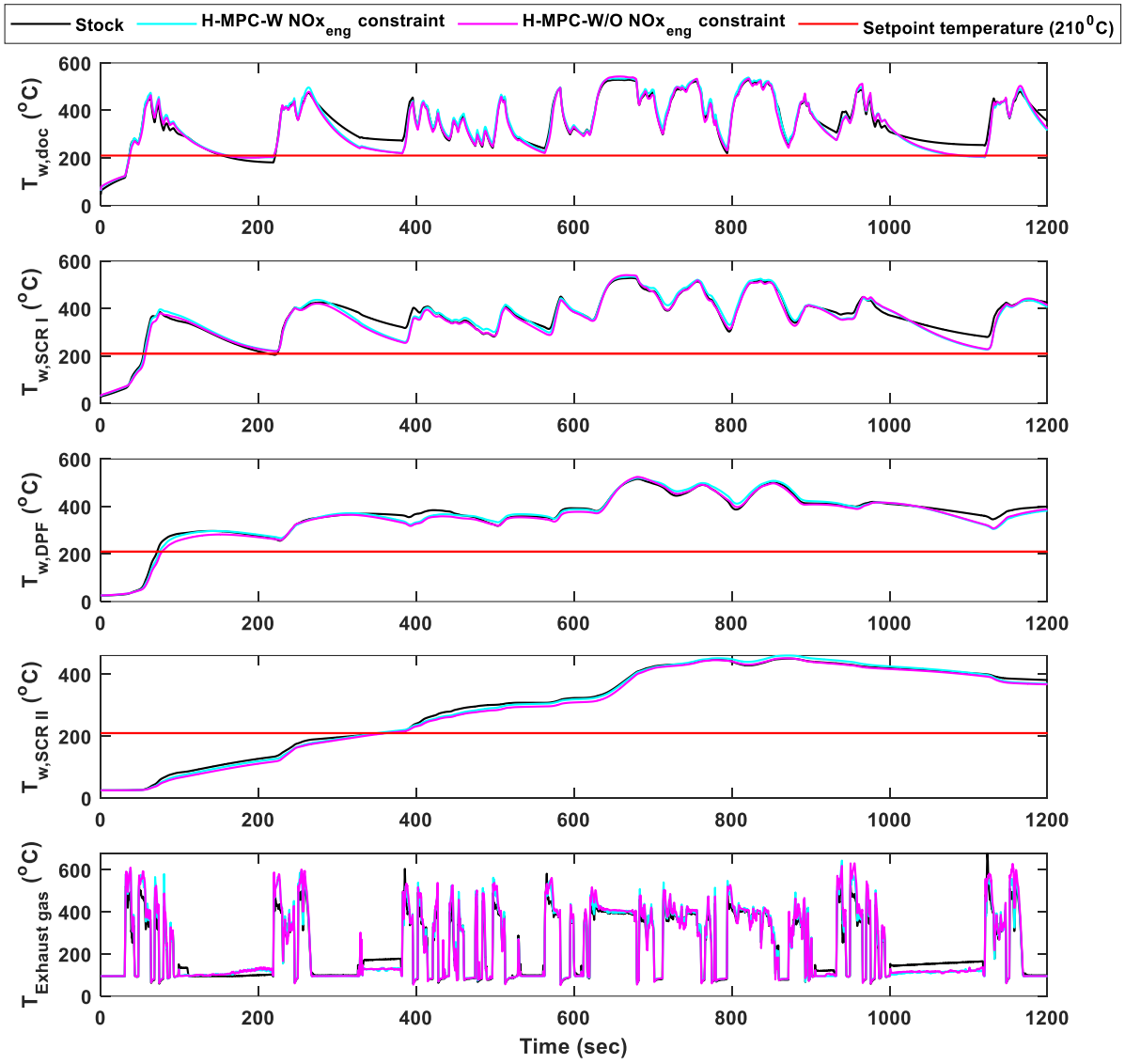

Figure 5-5: Software-in-the-loop results comparing aftertreatment temperature with and without engine-out oxides of nitrogen constraint against the stock.

The H-MPC is also simulated for different ATS initial temperature, as shown in Figure 5-6. Typically, at the start of a hot FTP cycle, the ATS temperature is 150 °C, and a warmed-up SCR refers to a temperature above 210 °C. Therefore, the H-MPC controller is validated at both 150 °C and 210 °C ATS initial temperatures. The H-MPC controller, irrespective of the ATS initial

temperature, provides significant tailpipe NO_X reduction without fuel penalty. Up to 0.8 % benefit in cycle averaged BSFC is obtained in H-MPC with 210 °C initial temperature. Table 5-2 compares the critical metrics for different aftertreatment initial temperatures.

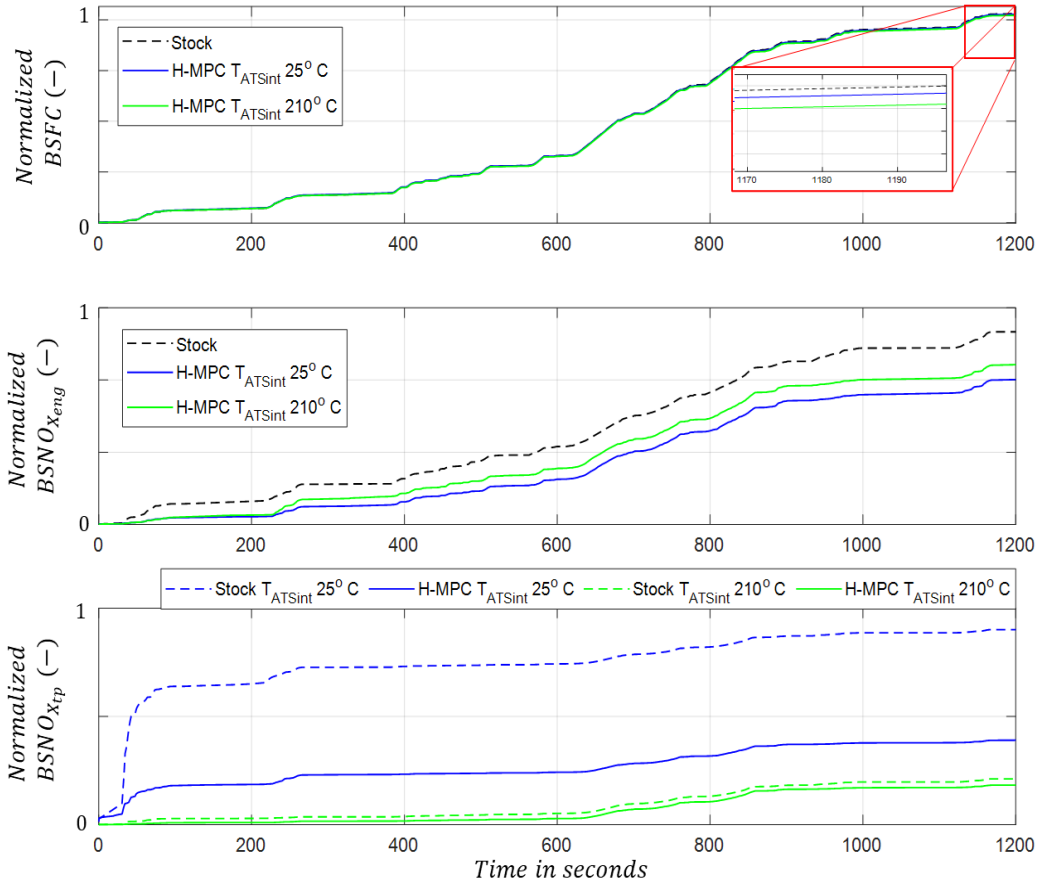

Figure 5-6: Software-in-the-loop results comparing critical cumulative parameters for different aftertreatment initial temperature against the stock.

Table 5-2: Comparison of critical parameters with engine-out NO_X constraint for various ATS initial temperature

	ATS initial temperature		
	25 °C	**150 °C**	**210 °C**
BSFC	-0.3 %	-0.6 %	-0.8 %
$\boldsymbol{BSNO_{X_{eng}}}$	-24 %	-20 %	-17 %
$\boldsymbol{BSNO_{X_{tp}}}$	-56 %	-45 %	-13 %

5.5 Conclusion

A hierarchical integrated engine and aftertreatment thermal management controller is designed with two different prediction horizons to handle the slow and fast dynamics in ATS and airpath. This architecture is implemented in a SIL architecture and simulated in real-time. Initial results show up to 0.8 % benefit in cycle averaged BSFC along with a 13 % reduction in tailpipe NO_X. With the controller already been validated in the dSPACE rapid prototyping hardware, experimental validation of this controller would be easier with just the input and out from the controller need to be connected to the respective engine control unit controlled are network (CAN) channels. The low-level controller was fine-tuned as an independent controller, however further fine tuning of the integrated low and high level controller will further improve the performance of the controller. Though this control architecture can be used with any drive cycle assuming that the controller can obtain a long-enough route preview information to effectively manage the thermal dynamics, the controller gains are tuned with FTP cycle as the primary focus. When the controller is used with a different drive cycle, further controller calibration will be needed.

Chapter 6 Conclusion and Future Work

This thesis presents a hierarchical model predictive control (H-MPC) architecture for real-time optimization of diesel engine fuel economy and emissions. The supervisory thermal management controller achieves a faster aftertreatment warmup compared to stock engine calibration and maintains the temperature above a set reference temperature. The control variables used by the high-level controller are intake manifold pressure and SOI. The low-level air path controller tracks the intake manifold pressure and SOI references from the supervisory controller while also satisfying safety and emission constraints. The HIL experimental validation of the low-level controller shows up to 1.4 % reduction in BSFC, 2 % reduction in engine-out NO_X, 40 % reduction in tailpipe NO_X, and 6 % reduction in brake-specific urea consumption (BSUC). The SIL simulation of the H-MPC mounted on a rapid prototype controller with the nonlinear virtual engine model shows 0.8 % reduction in BSFC, 17 % reduction in engine-out NO_X, and 13 % reduction in tailpipe NO_X.

Beyond the concrete improvement on efficiency several findings, and lessons were reached. A nonlinear virtual engine model comprising of a NO_X model, an engine airpath model, and an aftertreatment thermal model was developed. This virtual model is used for both controller tuning and SIL simulation. The physics-based engine-out NO_X emission model can be used in predictive applications to help with sensor delays and lags and with no need for an in-cylinder pressure sensor. This model can accurately capture the fast transient NO_X, and it can predict the effect in NO_X with change in engine calibration parameters like SOI, FRP, NOP, and intake manifold pressure and temperature with reasonable accuracy while affording the flexibility of adding more effects in the future. Experimental data validated the model accuracy, and a maximum error of 6.2 % was observed. The model's transient performance was also

evaluated with an engine run over the transient federal test procedure for heavy-duty engines, and an accuracy of 93 % was observed on a cycle-averaged basis.

Following large body of previous work, a full-order airpath model addressing an EGR path, which controls both intake manifold pressure and EGR mass flow rate, was developed. A minimal realization of the full-order model helped achieve a practically feasible integration time step (i.e., from 0.1 ms to 10 ms) at dSPACE hardware. A gain-scheduled torque controller and a Smith predictor in real-time using a rapid prototype controller was developed to allow the validation of the reduced-order airpath model. Moreover, the simplification was shown to rely on five states that could be measured on-board a vehicle, enabling full state feedback.

A rate-based MPC was designed for the short horizon air path control. It is based on the linearization of the previously developed reduced-order virtual airpath model. This controller utilizes a prediction horizon of 0.1 s and aims to track the supervisory controller's references while also satisfying engine safety and emission constraints. A single linear plant model is chosen to represent the entire operating range, and hence plant scheduling is avoided. The optimization is performed online by using an iterative quadratic solver. A Kalman filter is used to estimate the non-physical state in the rate-based controller, and full state feedback from the engine-mounted sensors is utilized.

The supervisory controller utilizes a long prediction horizon (20 s) to effectively predict the slow aftertreatment thermal dynamics with intake manifold pressure and SOI as control variables. The supervisory controller and low-level MPC controller are integrated together with the toque controller. It is validated through a SIL simulation by implementing this architecture in a rapid prototype controller with the virtual engine model. Real-time SIL simulation results show fuel benefit along with faster aftertreatment warmup compared to the stock engine case.

Robustness of the MPC controller was not studied in this current research. However, the controller was validated extensively in SIL and HIL environments over an aggressive FTP cycle. The robustness of the controller for noise in the feedback and plant model uncertainty needs to

be evaluated. Full state feedback is utilized through engine mounted sensors however, this may not be available in the conventional engine. Hence observer design and its impact on controller performance needs to be studied.

The H-MPC, which is validated in SIL simulation, can be validated experimentally. The current SIL architecture that is already mounted in a rapid prototype controller would need only a minimal signal configuration to make it work in the HIL experiment. On-road implementation and validation of this controller would be a giant step to look forward. This controller being well tunned and tested in engine dynamometer, testing it on-road would provide insights on controller's performance in fuel economy, drivability, and emissions. On-road test would also evaluate the controller's performance with the presence of noise and offset in the feedback signals could be evaluated.

Appendix A

Reduction of the linear-quadratic (LQ) MPC problem with constraints J_N to standard quadratic program form. The cost function J_N is given by:

$$\min_{u_0, u_1, \dots, u_{N-1}} J_N = (x_N)^T P_N(x_N) + \sum_{k=0}^{N-1} [(x_k)^T Q(x_k) + (u_k)^T R(u_k)]$$

Subject to $x_{k+1} = Ax_k + Bu_k$,

$x_0 = current\ state$,

$x_{min} \leq x_k \leq x_{max}, k = 1, \dots, N$, and

$u_{min} \leq u_k \leq u_{max}, k = 0, \dots, N-1$.

The first optimal move u_0^* defines the MPC feedback law, i.e, $u_{MPC}^*(x_0) = u_0^*$.

The stacked state and control vectors $X \in \mathbb{R}^{N.n_x}$,

$U \in \mathbb{R}^{N.n_u}$ are given by:

$$X = [x_1 \quad x_2 \quad . \quad . \quad . \quad x_N]^T, U = [u_1 \quad u_2 \quad . \quad . \quad . \quad u_N]^T.$$

The state transition formula,

$$x_k = A^k x_0 + \sum_{i=0}^{k-1} A^{k-1-i} B\, u_i,$$

yields the following relation,

$$X = SU + Mx_0,$$

where,

$$S = \begin{bmatrix} B & 0 & \cdots & 0 \\ AB & B & \cdots & 0 \\ \vdots & \vdots & \vdots & \vdots \\ A^{N-1}B & A^{N-2}B & \cdots & B \end{bmatrix}, \quad M = \begin{bmatrix} A \\ A^2 \\ \vdots \\ A^N \end{bmatrix}$$

The state and control vector with constraints can be expressed as,

$$GU \leq W + Tx_0, \text{with } G = \begin{bmatrix} S \\ -S \\ I \\ -I \end{bmatrix}, W = \begin{bmatrix} X_{max} \\ -X_{min} \\ U_{max} \\ -U_{min} \end{bmatrix}, T = \begin{bmatrix} -M \\ M \\ 0 \\ 0 \end{bmatrix}$$

where,

$X_{min} = [x_{min} \quad x_{min} \quad \cdots \quad x_{min}]^T$,

$X_{max} = [x_{\max} \quad x_{max} \quad \cdots \quad x_{max}]^T$,

$U_{min} = [u_{min} \quad u_{min} \quad \cdots \quad u_{min}]^T$, and

$U_{max} = [u_{max} \quad u_{max} \quad \cdots \quad u_{max}]^T$.

Now the constrained LQ-MPC problem can be expressed in the standard form as:

$$\min_{\mathrm{U}\epsilon\mathbb{R}^{N\times n_u}} J_N = \frac{1}{2}U^T HU + q^T U, \text{and}$$

$$subject\ to\ GU \leq W + Tx_0,$$

$$H = S^T \bar{Q} S + \bar{R} \text{ and } q = S^T \bar{Q} M x_0$$

$$\bar{Q} = \begin{bmatrix} Q & \cdots & \cdots & \cdots & 0 \\ 0 & Q & \cdots & \cdots & 0 \\ \vdots & \cdots & \ddots & \cdots & \vdots \\ 0 & \cdots & \cdots & Q & 0 \\ 0 & \cdots & \cdots & 0 & P \end{bmatrix}, \text{ and } \bar{R} = \begin{bmatrix} R & \cdots & 0 \\ \vdots & \ddots & \vdots \\ 0 & \cdots & R \end{bmatrix}$$

The discrete plant model corresponding to the linearization point at 1000 engine RPM and 1500 Nm engine torque is provided in

$$A = \begin{bmatrix} 0.6877 & 0.0440 & 0.0060 & -0.0006 & 0.3169 \\ 0.0888 & 0.9105 & -0.0486 & 0.0097 & 0.0227 \\ 0.0211 & 0.0734 & 0.7867 & -0.0083 & 0.0468 \\ 0.3839 & -0.0320 & -0.0012 & 0.9098 & -0.4698 \\ 0.0299 & -0.0024 & 0.0399 & 0.0062 & 0.9372 \end{bmatrix}$$

$$B = 1e^{-3} \begin{bmatrix} 0.0870 & -0.0012 \\ 0.4258 & 0.0095 \\ -0.6496 & 0.0330 \\ -0.0869 & -0.1187 \\ -0.0197 & -0.0091 \end{bmatrix}$$

$$C = I_{5\times 5} \text{ and } D = [0]$$

Appendix B

Dual gradient projection algorithm

Define $H_d = GH^{-1}G^T$,

$q_d = GH^{-1}q + \widetilde{W}$, and

$\widetilde{W} = W + Tx_0$.

Compute $L = \|H_d\|$

Algorithm:

- Set $\lambda^0, k = 0$
- Repeat $\lambda^{k+1} = \max(0, \lambda^k - \frac{1}{L}(H_d\lambda^k + q_d))$
- Until a termination criterion is satisfied at which $\lambda^* = \lambda^{k_{max}}$

Recover primal solution as $U^*(\lambda^*) = -H^{-1}(q + G^T\lambda^*)$

The matrices H_d, q_d, $\widetilde{W}$, and L are calculated corresponding to the linearization point. The vector of dual variables for the first iteration λ^0 set as a vector of 1. The maximum number of iteration (k_{max}) is set equal to 10.

Appendix C

Scalar reference governor

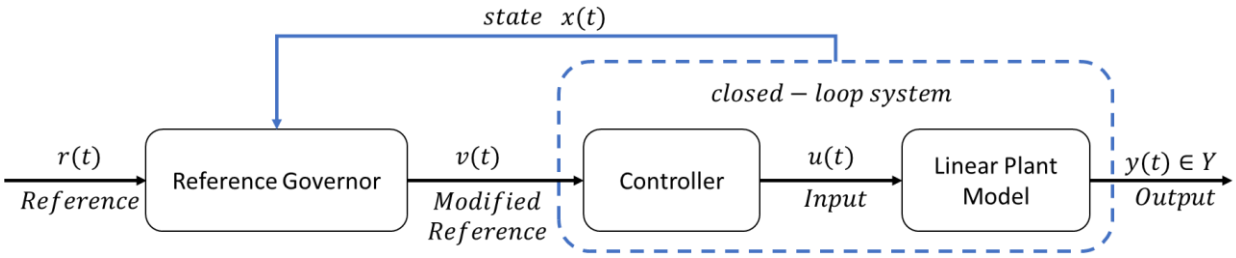

The Reference Governor is an add-on scheme that enforces pointwise in time state and control constraints by modifying the reference command to a well-designed closed loop system.

The discrete-time linear time invariant system is given by,

$$x(t+1) = Ax(t) + Bv(t),$$
$$y(t) = Cx(t) + Dv(t),$$

Where A, B, C, and D represents the closed loop system with controller. $x(t) \in \mathbb{R}^n$ is the state, $v(t) \in \mathbb{R}^m$ is the modified reference, and $y(t) \in \mathbb{R}^p$ is the output. The output constraint is given by,

$$y(t) \in \mathrm{Y}, \forall \mathrm{t} \in \mathbb{Z}^+,$$

where $Y \subset \mathbb{R}^p$ is a specified set.

The maximal output admissible set O_∞ is the set of all states x and inputs v such that the predicted response from the initial state x and with v maintained constant along the prediction satisfies the constraints, that is,

$$O_\infty \triangleq \{(x, v): \hat{y}(k|x, v) \in \mathrm{Y}, \forall\, k \in \mathbb{Z}^+\},$$

A tightened version of O_∞ can be obtained by,

$$\tilde{O}_\infty = O_\infty \cap O_\epsilon,$$

Where $O_\epsilon \triangleq \{(x, v): \bar{y}_v \in (1-\epsilon)Y\}$ and $y_v = (D + C(I - A)^{-1}B)v$ is the output at steady-state.

$$\hat{y}(k|x,v) = CA^k x + C\sum_{m=1}^{k} A^{m-1}Bv + Dv,$$

If A is Schur,

$$\hat{y}(k|x,v) = CA^k x + C(I-A)^{-1}(I-A^k)Bv + Dv, \quad (75)$$

Finite determination of O_∞:

As shown in [72],

Theorem 0: O_∞ is finitely determined if and only if $O_k = O_{k+1}$ for some $k \in \mathbb{Z}^+$.

Theorem 1: If A is Schur, (A, C) is observable, and Y is compact, then O_∞ is finitely determined. Furthermore, O_∞ is positively invariant, and if Y is convex, O_∞ is convex.

Collection of inequality functions:

Theorem 2: For $i = 1, \dots, s, f_i: \mathbb{R}^p \to \mathbb{R}$ are continuous and $f_i(0) \leq 0$. Then:

i) $O \in O_\infty$

ii) $O_\infty = \{(x,v): g_i(x,v) \leq 0, i \in \{1, \dots, s\}\}$

iii) $g_i(x,v) = \sup\{f_i\left(CA^k x + C\sum_{m=1}^{k} A^{m-1}Bv + Dv\right), k \in \mathbb{Z}^+\}$

Explicit algorithm to determine k^* and O_∞:

Step 1: Set $k = 0$.

Step 2: Solve for $i = 1, \dots, s$

$$\max_{(x,v)} j_i(x,v) = f_i(CA^{k+1}x + C\sum_{m=1}^{k+1} A^{m-1}Bv + Dv),$$

$$s.t. f_j\left(CA^l x + C\sum_{m=1}^{l} A^m Bv + Dv\right) \leq 0, j = 1, \dots, s, l = 0, \dots, k$$

Let $J_i^* = max\, J_i(x,v)$.

If $J_i^* \leq 0 \; for \; i = 1, \dots, s \rightarrow$ stop, set $k^* = k$ and $O_\infty = \left\{(x, v): f_i\left(CA^l x + C\sum_{m=1}^{l} A^{m-1}Bv + Dv\right) \leq 0, i \in \{1, \dots, s\}, l \in \{0, \dots, k^*\}\right\}$.

Else → continue.

Step 3: Replace k by $k + 1$and return to step 2.

Assume that $x(t)$ is available at time instant t. For all $t \geq 0$, compute $v(t)$ as close as possible to $r(t)$ along the line segment connecting $v(t-1)$ to $r(t)$such that $(v(t), x(t)) \in \tilde{O}_\infty$ [19].

More formally,

$$\kappa(t) = \max_{\kappa \in [0,1]} \kappa$$

$$\text{s.t, } v = v(t) + \kappa\big(r(t) - v(t)\big),$$

$$\big(v, x(t)\big) \in \tilde{O}_\infty,$$

Where $\kappa(t) \in [0,1]$, and $v(t+1) = v(t) + \kappa(t)\big(r(t) - v(t)\big)$ is the command step at t+1.

SRG Implementation - Closed form solution [13]

Assume that $\tilde{O}_\infty$ is polyhedral, that is

$$\tilde{O}_\infty = \{(x, v) = H_x x + H_v v \leq s\},$$

$$\kappa(t+1) = \min\left\{\min_{j \in J^+}\left\{\frac{s_j - h_{x,j}^T x(t) - h_{v,j}^T v(t)}{h_{v,j}^T (r(t) - v(t))}\right\}, 1\right\},$$

where $h_{x,j}^T$ and $h_{v,j}^T$ are the j-th row of H_x and H_v, respectively, s_j is the j-th element of s, and $J^+$is the set such that $h_{v,j}^T\big(r(t) - v(t)\big) > 0$. If $J^+ = \emptyset$, then $\kappa(t+1) = 1$.

Bibliography

[1]. ATA [American Trucking Associations]. (2020). American Trucking Trends 2020 Report. Arlington

[2]. John B. Heywood. Internal Combustion Engine Fundamentals, Second Edition (McGraw-Hill Education: New York, Chicago, San Francisco, Athens, London, Madrid, Mexico City, Milan, New Delhi, Singapore, Sydney, Toronto, 2018).

[3]. Tsuneyoshi, K., Takagi, O., and Yamamoto, K., "Effects of Washcoat on Initial PM Filtration Efficiency and Pressure Drop in SiC DPF," SAE Technical Paper 2011-01-0817, 2011, https://doi.org/10.4271/2011-01-0817.

[4]. Guzzella, L. and Onder, Ch.H. (2010) Introduction to Modelling and Control of Internal Combustion Engine Systems. 2nd Edition, Springer Editor. http://dx.doi.org/10.1007/978-3-642-10775-7

[5]. G. Cavataio, H.-W. Jen, J. R. Warner, J. W. Girard, J. Y. Kim, and C. K. Lambert, "Enhanced durability of a Cu/zeolite based SCR catalyst," SAE International Journal of Fuels and Lubricants, vol. 1, no. 2008- 01-1025, pp. 477–487, 2008.

[6]. "Greenhouse Gas Emissions and Fuel Efficiency Standards for Medium- and Heavy-Duty Engines and Vehicles— Phase 2", https://www.govinfo.gov/content/pkg/FR-2016-10-25/pdf/2016-21203.pdf.

[7]. California Air Resources Board (CARB), "Heavy-Duty Low NOx Program Public Workshop," January 23, 2019, online, available at: https://ww3.arb.ca.gov/msprog/hdlownox/files/workgroup_20190123/00-background_&_timing_ws01232019.pdf, accessed July 7, 2020.

[8]. US EPA, "Regulations for Emissions from Vehicles and Engines - Cleaner Trucks Initiative," online, available at: https://www.epa.gov/regulations-emissions-vehicles-andengines/cleaner-trucks-initiative, accessed July 7, 2020.

[9]. EPA Emission Standards Reference Guide, "EPA Emission Standards for Heavy-Duty Highway Engines and Vehicles," online, available at: https://www.epa.gov/emissionstandards-reference-guide/epa-emission-standards-heavyduty-highway-engines-and-vehicles, accessed July 7, 2020.

[10]. Manimaran, R., and R. Thundil Karuppa Raj. “CFD Analysis of Combustion and Pollutant Formation Phenomena in a Direct Injection Diesel Engine at Different EGR Conditions.” Procedia Engineering. Vol. 64. Elsevier Ltd, 2013. 497–506. Procedia Engineering. Web.

[11]. Mentink, P., Seykens, X., and Escobar Valdivieso, D., "Development and Application of a Virtual NOx Sensor for Robust Heavy Duty Diesel Engine Emission Control," SAE Int. J. Engines 10(3):1297-1304, 2017.

[12]. George A. Lavoie, John B. Heywood & James C. Keck., “Experimental and Theoretical Study of Nitric Oxide Formation in Internal Combustion Engines”, 1970.

[13]. Arrègle, J., López, J., Guardiola, C., and Monin, C., "Sensitivity Study of a NOx Estimation Model for On-Board Applications," SAE Technical Paper 2008-01-0640, 2008.

[14]. C. Guardiola ,J.J. López, J. Martín, D. García-Sarmiento, “Semiempirical in-cylinder pressure based model for NOX prediction oriented to control applications, Applied Thermal Engineering, Volume 31, Issue 16, November 2011, Pages 3275-3286.

[15]. Savva, N. and Hountalas, D., "Detailed Evaluation of a New Semi-Empirical Multi-Zone NOx Model by Application on Various Diesel Engine Configurations," SAE Technical Paper 2012-01-1156, 2012.

[16]. Quérel, C., Grondin, O., Letellier, C., “Semi-physical mean-value NOxmodel for diesel engine control,” Control Engineering Practice 40, 27–44, 2015.

[17]. Guardiola C., Martin J., Pla B., Bares P., “Cycle by cycle NOx model for diesel engine control,” Applied Thermal Engineering, 110 , pp. 1011-1020, 2017.

[18]. Asprion, J., Chinellato, O., & Guzzella, L, “Optimisation-oriented modelling of the NOx emissions of a Diesel engine,” Energy Conversion and Management, 75, 61–73. (2013).

[19]. Asprion, J., Chinellato, O., & Guzzella, L, “A fast and accurate physics-based model for the NOx emissions of Diesel engines,” Applied Energy, ISSN: 0306-2619, Vol: 103, Page: 221-233.

[20]. Saravanan D, Rasoul Salehi, Anna Stefanopoulou, Siddharth Mahesh and Marc Allain, “Control-Oriented Physics-based NOx emission model for a diesel engine with exhaust gas recirculation,” Proceedings of Dynamic Systems and Control Conference. DSCC2019-9247, 2019.

[21]. Duraiarasan, S., Salehi, R., Stefanopoulou, A., Mahesh, S., and Allain, M. (March 12, 2020). "Control-Oriented Physics-Based NOX Emission Model for a Diesel Engine With Exhaust Gas Recirculation." ASME. Letters Dyn. Sys. Control. January 2021; 1(1): 011008.

[22]. J. P. Jensen, A. F. Kristensen, S. C. Sorenson, N. Houbak, and E. Hendricks, “Mean value modeling of a small turbocharged diesel engine,” in SAE paper 910 070, 1991.

[23]. Kao, M., and Moskwa, J. J. (March 1, 1995). "Turbocharged Diesel Engine Modeling for Nonlinear Engine Control and State Estimation." ASME. Journal for Dynamical System, Measurement and Control, 117(1): 20–30, March 1995.

[24]. L. Guzzella and A. Amstutz, “Control of diesel engines” IEEE Control System Magazine 18(5):53 –71, 1998.

[25]. A.G. Stefanopoulou, I. Kolmanovsky, and J.S. Freudenberg, “Control of variable geometry turbocharged diesel engines for reduced emissions. IEEE Trans. Control Syst. Technol., 8(4):733 –745, 2000.

[26]. Lee, S., Andert, J., Neumann, D., Querel, C. et al., “Hardware-in-the- Loop-Based Virtual Calibration Approach to Meet Real Driving Emissions Requirements,” SAE Int. J. Engines 11(6):1479‑1504, 2018.

[27]. M. Jankovic, M. Jankovic, and I. Kolmanovsky, "Constructive Lyapunov control design for turbocharged diesel engines," in IEEE Transactions on Control Systems Technology, vol. 8, no. 2, pp. 288-299, March 2000.

[28]. Johan Wahlström and Lars Eriksson, “Modelling diesel engines with a variable-geometry turbocharger and exhaust gas recirculation by optimization of model parameters for capturing non-linear system dynamics,”, Proceedings of the Institution of mechanical engineers. Part D, journal of automobile engineering, (225), 7, 960-986, 2011.

[29]. Lee, S., Andert, J., Pischinger, S., Ehrly, M. et al., "Scalable Mean Value Modeling for Real-Time Engine Simulations with Improved Consistency and Adaptability," SAE Technical Paper 2019-01-0195, 2019.

[30]. Duraiarasan, S., Salehi, R., Wang, F., Stefanopoulou, A. et al., "Real-Time Embedded Models for Simulation and Control of Clean and Fuel-Efficient Heavy-Duty Diesel Engines," SAE Technical Paper 2020-01-0257, 2020.

[31]. A. G. Stefanopoulou, I. Kolmanovsky, and J. S. Freudenberg, "Control of variable geometry turbocharged diesel engines for reduced emissions," in IEEE Transactions on Control Systems Technology, vol. 8, no. 4, pp. 733-745, July 2000, doi: 10.1109/87.852917.

[32]. J. Ruckert, B. Kinoo, M. Kruger, A. Schlosser, H. Rake, and S. Pischinger, “Simultaneous control of boost pressure and exhaust gas recirculation in a passenger car diesel engine,” MTZ Worldwide, vol. 62, no. 11, 2001.

[33]. P. Ortner, and L. del Re, “Predictive control of a diesel engine air path. IEEE Transactions on Control Systems Technology,” vol. 15, no. 3, pp. 499-456, 2007.

[34]. Urban Maeder, Francesco Borrelli, Manfred Morari, “Linear offset-free model predictive control,” Automatica, vol 45, Issue 10, 2009.

[35]. M. Santillo and A. Karnik, "Model Predictive Controller design for throttle and wastegate control of a turbocharged engine," 2013 American Control Conference, Washington, DC, 2013, pp. 2183-2188, doi: 10.1109/ACC.2013.6580159.

[36]. F. Borrelli, M. Baotić, J. Pekar and G. Stewart, "On the complexity of explicit MPC laws," 2009 European Control Conference (ECC), Budapest, 2009, pp. 2408-2413, doi: 10.23919/ECC.2009.7074766.

[37]. G. Stewart, and F. Borrelli, “A model predictive control framework for industrial turbodiesel engine control,” proceedings of the 47th IEEE conference on decision and control. Cancun, Mexico, pp. 5704-5711, 2008.

[38]. Mike Huang, Hayato Nakada, Srinivas Polavarapu, Ken Butts, and Ilya Kolmanovsky, “Rate-based model predictive control of Diesel engines,” IFAC Proceedings vol, vol 46, Issue 21, 2013.

[39]. M. Huang, D. Liao-McPherson, S. Kim, K. Butts, and I. Kolmanovsky, "Toward Real-Time Automotive Model Predictive Control: A Perspective from a Diesel Air Path Control Development," 2018 Annual American Control Conference (ACC), Milwaukee, WI, 2018, pp. 2425-2430, doi: 10.23919/ACC.2018.8431407.

[40]. Gokul S. Sankar, Rohan C. Shekhar, Chris Manzie, Takeshi Sano, and Hayato Nakada. “Fast Calibration of a Robust Model Predictive Controller for Diesel Engine Airpath.” IEEE Transactions on Control Systems Technology 28 (2020): 1505-1519.

[41]. Cloudt, R. and Willems, F., "Integrated Emission Management strategy for cost-optimal engine-aftertreatment operation," SAE Int. J. Engines 4(1):1784-1797, 2011.

[42]. Zentner, Stephan & Asprion, Jonas & Onder, Christopher & Guzzella, Lino, “An Equivalent Emission Minimization Strategy for Causal Optimal Control of Diesel Engines,” Energies. 7. 1230-1250. 10.3390/en7031230, 2014.

[43]. Chen, Pingen & Wang, Junmin, “Nonlinear Model Predictive Control of Integrated Diesel Engine and Selective Catalytic Reduction System for Simultaneous Fuel Economy Improvement and Emissions Reduction,” Journal of Dynamic Systems, Measurement, and Control. 137. 081008. 10.1115/1.4030252, 2015.

[44]. Donkers, M. C.F., J. Van Schijndel, W. P.M.H. Heemels, and F. P.T. Willems, “Optimal Control for Integrated Emission Management in Diesel Engines.” Control Engineering Practice 61 (April). Elsevier Ltd: 206–16, 2017.

[45]. R. Salehi, A. Stefanopoulou, S. Mahesh, and M. Allain, "Reduced-Order Long-Horizon Predictive Thermal Management for Diesel Engine Aftertreatment Systems," *2019 American Control Conference (ACC)*, Philadelphia, PA, USA, 2019, pp. 1611-1616.

[46]. Huang, Chunan & Salehi, Rasoul & Ersal, Tulga & Stefanopoulou, Anna, “An energy and emission conscious adaptive cruise controller for a connected automated diesel truck,” Vehicle System Dynamics. 58. 1-21. 10.1080/00423114.2020.1740283, 2020.

[47]. Zhang, X., Farina, M., Spinelli, S. and Scattolini, R, “Multi-rate model predictive control algorithm for systems with fast-slow dynamics. IET Control Theory Appl., 12: 2468-2477, 2018.

[48]. M.A. Brdys, M. Grochowski, T. Gminski, K. Konarczak, M. Drewa, Hierarchical predictive control of integrated wastewater treatment systems, Control Engineering Practice, Volume 16, Issue 6, 2008, Pages 751-767.

[49]. Dec, J., "A Conceptual Model of DI Diesel Combustion Based on Laser-Sheet Imaging," SAE Technical Paper 970873, 1997.

[50]. Hendricks, E., Chevalier, A., Jensen, M., Sorenson, S. et al., "Modelling of the Intake Manifold Filling Dynamics," SAE Technical Paper 960037, 1996.

[51]. John B. Heywood, “Internal combustion engine fundamentals”, Second Edition, McGraw-Hill Education, Page: 1039-1040.

[52]. Improving air quality compliance with the law, “EPA Demonstrates Effective Controls for Its On-Road Heavy-Duty Vehicle Compliance Program; Further Improvements Could Be Made”, US EPA Office of Inspector General, Report No. 19-P-0168 June 3, 2019.

[53]. J. P. Jensen, A. F. Kristensen, S. C. Sorenson, N. Houbak, and E. Hendricks, “Mean value modeling of a small turbocharged diesel engine,” in SAE paper 910 070, 1991.

[54]. Kao, M., and Moskwa, J. J. (March 1, 1995). "Turbocharged Diesel Engine Modeling for Nonlinear Engine Control and State Estimation." ASME. Journal for Dynamical System, Measurement and Control, 117(1): 20–30, March 1995.

[55]. L. Guzzella and A. Amstutz, “Control of diesel engines” IEEE Control System Magazine 18(5):53 –71, 1998.

[56]. A.G. Stefanopoulou, I. Kolmanovsky, and J.S. Freudenberg, “Control of variable geometry turbocharged diesel engines for reduced emissions. IEEE Trans. Control Syst. Technol., 8(4):733 –745, 2000.

[57]. Lee, S., Andert, J., Neumann, D., Querel, C. et al., “Hardware-in-the- Loop-Based Virtual Calibration Approach to Meet Real Driving Emissions Requirements,” SAE Int. J. Engines 11(6):1479‑1504, 2018.

[58]. M. Jankovic, M. Jankovic and I. Kolmanovsky, "Constructive Lyapunov control design for turbocharged diesel engines," in IEEE Transactions on Control Systems Technology, vol. 8, no. 2, pp. 288-299, March 2000.

[59]. Johan Wahlström and Lars Eriksson, “Modelling diesel engines with a variable-geometry turbocharger and exhaust gas recirculation by optimization of model parameters for capturing non-linear system dynamics,”, Proceedings of the Institution of mechanical engineers. Part D, journal of automobile engineering, (225), 7, 960-986, 2011.

[60]. Lee, S., Andert, J., Pischinger, S., Ehrly, M. et al., "Scalable Mean Value Modeling for Real-Time Engine Simulations with Improved Consistency and Adaptability," SAE Technical Paper 2019-01-0195, 2019.

[61]. Mike J Hand, Erik Hellstro¨m, Doohyun Kim, Anna Stefanopoulou, Justin Kollien, and Craig Savonen. Model and calibration of a diesel engine air path with an asymmetric twin scroll turbine. In ASME 2013 Internal Combustion Engine Division Fall Technical Conference, pp V001T05A010–V001T05A010, 2013.

[62]. Salehi, R., and Stefanopoulou, A. G. "Parameter Set Reduction and Ensemble Kalman Filtering for Engine Model Calibration." ASME. J. Dyn. Sys., Meas., Control, , 2019.

[63]. DJ Rausen, AG Stefanopoulou, J-M Kang, JA Eng, and T-W Kuo. A mean-value model for control of homogeneous charge compression ignition (HCCI) engines. Journal of Dynamic Systems, Measurement, and Control, 127(3):355–362, 2005.

[64]. Stefan Kuenzel. Method for treating exhaust gas and arrangement of an exhaust gas system on an internal combustion engine, US Patent US20150260068A1.

[65]. Saravanan D, Rasoul Salehi, Anna Stefanopoulou, Siddharth Mahesh and Marc Allain, “Control-Oriented Physics-based NOx emission model for a diesel engine with exhaust gas recirculation,” Proceedings of Dynamic Systems and Control Conference. DSCC2019-9247, 2019.

[66]. J. Wahlström and L. Eriksson, "Output Selection and Its Implications for MPC of EGR and VGT in Diesel Engines," in IEEE Transactions on Control Systems Technology, vol. 21, no. 3, pp. 932-940, May 2013, doi: 10.1109/TCST.2012.2191289.

[67]. Wang, Liuping, “A Tutorial on Model Predictive Control: Using a Linear Velocity-Form Model,” Developments in Chemical Engineering and Mineral Processing. 12. pp 573-614, 2004.

[68]. H. Wassén, J. Dahl, A. Idelchi, “Holistic Diesel Engine and Exhaust After-Treatment Model Predictive Control,” IFAC-PapersOnLine, Volume 52, Issue 5, 2019, Pages 347-352, ISSN 2405-8963.

[69]. Stefanopoulou, A. G.; Storset, O. F.; Smith, R, “Pressure and temperature-based adaptive observer of air charge for turbocharged diesel engines,” Int Journal of Robust and Nonlinear Control 14(6): 543-560.

[70]. Chundru, V., Parker, G., & Johnson, J. H. (2019). The Effect of NO2/NOx Ratio on the Performance of a SCR Downstream of a SCR Catalyst on a DPF. SAE International Journal of Fuels and Lubricants, 12(2), 121-141. http://doi.org/10.4271/04-12-02-0008

[71]. Chen, P., Wang, J, “Nonlinear and adaptive control of NO/NO_2 ratio for improving selective catalytic reduction system performance,” Journal of the Franklin Institute, Volume 350, Issue 8, 2013, Pages 1992-2012, ISSN 0016-0032, https://doi.org/10.1016/j.jfranklin.2013.05.020.

[72]. Emanuele Garone, Stefano Di Cairano, Ilya Kolmanovsky, “Reference and command governors for systems with constraints: A survey on theory and applications,” Automatica, Volume 75, 2017, Pages 306-328, ISSN 0005-1098, https://doi.org/10.1016/j.automatica.2016.08.013.

[73]. Ye, Peng and Boehman, André L, “Investigation of the Impact of Engine Injection Strategy on the Biodiesel NOx Effect with a Common-Rail Turbocharged Direct Injection Diesel Engine,” Energy & Fuels, 2010, Volume 24, pages 4215 – 4225, https://doi.org/10.1021/ef1005176.